## Title

Synthesis, Fabrication, and Strain Engineering of Flexible Nanoelectronics Using Graphene and Other 2D Layered Materials

**Author**

Weiss, Nathan O

**Publication Date**

2019

UNIVERSITY OF CALIFORNIA

Los Angeles

# Synthesis, Fabrication, and Strain Engineering of Flexible Nanoelectronics Using Graphene and Other 2D Layered Materials

A dissertation submitted in partial satisfaction of the
requirements for the degree Doctor of Philosophy
in Materials Science and Engineering

by

Nathan Oulton Weiss

2019

# ABSTRACT OF THE DISSERTATION

# Synthesis, Fabrication, and Strain Engineering of Flexible Nanoelectronics Using Graphene and Other 2D Layered Materials

by

Nathan Oulton Weiss
Doctor of Philosophy in Materials Science and Engineering
University of California, Los Angeles, 2019
Professor Yu Huang, Chair

A new class of two-dimensional layered materials (2DLMs) has emerged with promising advancements made in nanoelectronics and flexible devices. Graphene, an atomically thin layer of carbon atoms in a honeycomb lattice, has gathered significant interest, followed by similar materials molybdenite, boron nitride, and black phosphorus among many others. As nanoscale building blocks, they exhibit a range of metallic, semiconducting, and insulating varieties in which to mix and match into van der Waals heterostructures (vdWHs) via controlled restacking that enables innovative nanoelectronic devices. These nanosheets behave as atomic membranes which can be stretched and bent in order to manipulate their properties using so-called nanoscale origami, such as inducing a bandgap via strain engineering. A wide range of devices utilize the unique advantages of these 2DLMs for future applications such as flexible electronics, soft robotics, biocompatible interfaces and wearable technology. High-speed electronics that utilize graphene and $MoS_2$ are capable of outstanding performance for gigahertz regime, low-power operation using self-aligned top-gated transistors. Additionally, graphene is used as transparent, flexible, electronically tunable contact electrodes. Scalable synthesis of 2DLMs utilizes chemical vapor deposition (CVD) growth of large-area, uniform monolayer films with moderate sacrifices in electronic performance and field effect transport characteristics. Unique device designs using 2DLMs provide technological improvements in practically every subfield of electronics and beyond, yet many roadblocks remain in efforts to make use of these materials in practical and commercial applications, for instance graphene's zero bandgap. We present two approaches towards precise application of strain in these two-dimensional membranes and observe the impact on their material properties. First, by suspending graphene across gaps and on top of topographically patterned substrates, the membrane is freestanding and capable of stretching between the peaks and valleys out of plane on the underlying surface. Using self-assembled monolayers of polystyrene spheres from 500 nm – 2 μm in diameter, $O_2$ plasma etching the spheres into a mask for selectively etching $SiO_2$ substrate into nanopillars, we create periodic structures that graphene is transferred onto. Second, elastic substrates of PDMS are prestrained, exposed to $O_2$ plasma, and transferred with graphene before relaxing, buckling the surface and forming ordered wrinkles and periodic, nanoscale ripples. Biaxial prestrain creates herringbone patterns, which can be precisely scaled in size from 500 nm – 3 μm wavelength with over 300 nm amplitude by controlling plasma dosage. Strained graphene structures are imaged and characterized with Raman spectroscopy mapping to analyze the peak shifting due to strain. These studies are part of a new paradigm using 2DLMs as membrane electronics manipulated through nanoscale origami for development of uniquely flexible devices.

The dissertation of Nathan Oulton Weiss is approved.

Richard B. Kaner

Qibing Pei

Xiangfeng Duan

Yu Huang, Committee Chair

University of California, Los Angeles

2019

# Table of Contents

# List of Figures

# Glossary

*2D* – '2D' characteristic peak of graphene
2DLM – two-dimensional layered material
$A$ – amplitude/height of the ripple
$A_{1g}$ – '$\mathrm{A_{1g}}$' characteristic peak of TMDs
AFM – atomic force microscopy
AOE – advanced oxide etch
ARPES – angle-resolved photoemission spectroscopy
$B_{2g}$ – '$\mathrm{B_{2g}}$' characteristic peak of TMDs
BN – boron nitride
BV – benzyl viologen
$C_0$ – back-gate capacitance
$d_0$ – initial diameter of the PS spheres
$d_\mathrm{e}$ – diameter of the etched spheres/pillars
$d_\mathrm{s}$ – minimum empty space between the etched spheres/pillars
DCE – dichloroethane
DNA – deoxyribonucleic acid
$E'$ – 'E' in-plane vibrational mode of TMDs
$E_F$ – Fermi energy
$E_g$ – bandgap energy
*EBL* – electron-beam lithography
$f_\mathrm{MAX}$ –frequency at which the power gain is equal to one
$f_\mathrm{T}$ – cutoff frequency of a transistor
FWHM – full width half max of a spectral peak
$G$ – 'G' characteristic peak of graphene
$G_\mathrm{ds}$ – drain–source conductance
*Gr* – graphene
$h_{21}$ – current gain
$I_\mathrm{ds}$ – drain–source current
IPA – isopropyl alcohol
$K$ – Dirac point of graphene's band structure
$L$ – channel length
MEMS – microelectromechanical systems
NEMS – nanoelectromechanical systems
OM – optical microscopy
rGO – reduced graphene oxide
$t$ – thin film thickness
TERS – tip-enhanced Raman spectroscopy
TMD – transition metal dichalcogenide
$R_C$ – contact resistance

SEM – scanning electron microscope
STM – scanning tunneling microscope
STS – scanning tunneling spectroscopy
SWNT – single-walled carbon nanotubes
TEM – transmission electron microscope
TMD – transition metal dichalcogenide
P3HT – poly(3-hexylthiophene-2,5-diyl)
PCBM – phenyl-C61-butyric acid methyl ester
PDMS – polydimethylsiloxane
PL – photoluminescence
PMMA – poly(methyl methacrylate)
PS – polystyrene
PTB7 – poly({4,8-bis[(2-ethylhexyl)oxy]benzo[1,2-b:4,5-b′]dithiophene-2,6-diyl}{3-fluoro-2-[(2 ethylhexyl)carbonyl]thieno[3,4-*b*]thiophenediyl})
PZT – lead zirconate titanate
$W$ – channel width
vdWH – van der Waals heterostructure
$V_g$ – gate voltage
$V_{ds}$ – drain–source bias voltage
XRD – x-ray diffraction
$Y_F$ – thin film plane-strain Young’s modulus
$Y_S$ – substrate plane-strain Young’s modulus
$\varepsilon$ – applied strain
$\varepsilon_{ps}$ – amount of applied prestrain
$\varepsilon_c$ – critical prestrain required to induce rippling
$\varepsilon_x$ – prestrain in the x-axis
$\varepsilon_y$ – prestrain in the y-axis
$\lambda$ – peak-to-peak wavelength between ripples
$\mu$ – carrier mobility
$\nu$ – Poisson’s ratio
$\omega$ – Raman spectral shift

# Acknowledgements

**Funding:**
National Institute of Health
NIH Director's New Innovator Award 1DP2OD004342-01
NIH Director's New Innovator Award 1DP2OD007279.

National Science Foundation
NSF CAREER Award 0956171
NSF IGERT: Materials Creation Training Program (MCTP)–DGE-0654431

**Institutions:**
University of California, Los Angeles
Henry Samueli School of Engineering and Applied Science
Department of Materials Science
410 Westwood Plaza, Los Angeles, CA 90095

California NanoSystems Institute
570 Westwood Plaza Building 114, Los Angeles, CA 90095

**Special Thanks:**

I would like to thank many people who help make this possible: My family for their continuous, unwavering support. All my friends, old and new. My roommates Eve, Seth, Andy, Mike, Jeff T, Jeff K, Chris, Adam, Ben, and Jordan. My doctoral research advisors Dr. Huang and Dr. Duan, and committee members Dr. Kaner and Dr. Pei. My previous research advisors, Dr. Cortez and Dr. Herman. My classmates and labmates Austin, Sarbajit, Dory, Yarleen, Jingwei, Rui, Yuan, Chin-yi, Lingyan, Yongjia, Yujing, Jingwei, Yung-chen, Yu, Xing, Jonathan, Boris, Ben, Chain, Hosein, Teng, Yuxi, Qiyuan, Yang, Mengning, Yun-Chiao, Hui-Ying, Hao, Hung-Chieh, Enbo, Bug, Dehui, Kayla, Ivan, Shan, Hailong, Xiaoqing, Mufan, Hua, Chen, Tanvi, Cara, Huanping, Shanyun and any other peers or collaborators that I may have missed. Everyone else who has helped me along the way. And readers like you!

# Biography

Nathan received his high school diploma from The Haverford School in Haverford, PA in 2005 before enrolling at Columbia University in New York City. In the summer of 2008, he joined a Research Experience for Undergraduates (REU) program at University of Puerto Rico-Mayagüez, studying the synthesis of spinel cobalt ferrite nanoparticles under Dr. Oscar Perales-Perez. In 2009 he received his Bachelor of Science in Materials Science and Engineering from the Fu Foundation School of Engineering and Applied Science at Columbia, with research on ultracentrifugal carbon nanotube enrichment with Dr. Irving P. Herman. He attended Johns Hopkins in Baltimore, Maryland with a Dean's Fellowship and received a Master of Science in Engineering Management in 2010 with a concentration in nanotechnology before attending UCLA. In 2010, Nathan joined the groups of Dr. Yu Huang and Dr. Xiangfeng Duan for his doctoral research in graphene and other two-dimensional layered materials. He received a National Science Foundation funded Materials Creation Training Program (MCTP) Fellowship from 2011–2013 and was awarded his Master of Science in Materials Science and Engineering from the Henry Samueli School of Engineering and Applied Science at UCLA in 2012. Nathan presented research posters at the 28th Latin American Chemical Congress in San Juan, Puerto Rico in 2008, UCLA Tech Forum in 2012, MCTP Symposiums at UCLA in 2012 and 2013, and the Bristol Centre for Functional Nanomaterials in England in 2013. He presented his research at the MCTP symposiums and the Emerging Research National Conference in STEM in Washington, DC in 2015.

# Chapter 1: Introduction

As electronics continue to influence advances in technology, improvements to the underlying science and engineering are necessary to accomplish higher performing and more capable applications. For instance, continuous shrinking down the dimensions of integrated circuits has propelled astounding advances in processing power; however, clear limits are unavoidable as we reach near-atomic dimensions. Getting down to one individual atomic thickness, graphene monolayers, and similarly other two-dimensional analogues, present one such limit of confinement in the single dimension of thickness. These two-dimensional layered materials (2DLMs) are therefore attractive for use in a wide range of cutting-edge technologies that open numerous opportunities in materials sciences and the electronics industry. In particular, these new nanomaterials enable novel applications in flexible devices that utilize properties unique to the nanoscale that extend beyond bulk crystals and the brittle, silicon-based microchips of today. This dissertation discusses methods of synthesizing and processing these 2DLMs, material characterization, and strain engineering of their material properties, as well as device fabrication and performance analysis.

Graphene (Figure 1.1), due to its exciting electronic and mechanical properties, enables many novel technologies in a wide array of applications[1] including high-speed[2,3] and flexible electronics which have been aggressively pursued.[4-6] Pristine graphene exhibits unique electronic behavior, as well as unparalleled carrier mobility,[7] elastic modulus, and yield strength.[8] Since the band structure is derived from the atomic structures and bonds, introducing strain, distortions, and defects will inevitably change the electronic properties. After the discovery of graphene, other 2DLMs (e.g. molybdenum disulfide and boron nitride) have been isolated into monolayers and investigated via use in advanced electronic devices which show extraordinary properties, along with additional advantages of obtaining semiconducting and insulating varieties based on the specific elements in the material. The controlled combination of these layers into precise nanostructures enables a large range of possibilities in designing nanodevices of exceptional performance and unprecedented capabilities.[9]

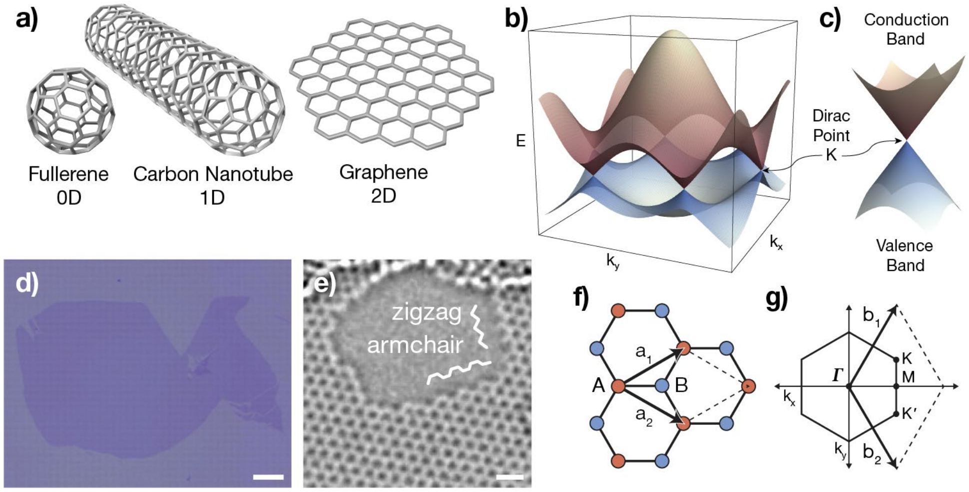

*Figure 1.1 – Carbon nanostructures and honeycomb lattice of graphene*
*a) Allotropes of carbon based on two-dimensional graphene (right), quasi-zero-dimensional buckminsterfullerene* $C_{60}$ *(left), and quasi-one-dimensional armchair single-walled nanotube (middle). b) Band structure of graphene and c) the linear dispersion relation showing the vertically mirrored Dirac cones intersecting at the Dirac point K. d) Optical microscopy of a graphene flake exfoliated from graphite. e) High-resolution TEM image of suspended graphene, showing a monolayer with a void in the middle and a bilayer region toward the top. Clear zigzag and armchair edges are seen. f) Hexagonal crystal structure of graphene with lattice parameters* $a_1$ *and* $a_2$ *and nonequivalent atomic positions A and B of the diatomic basis shown in red and blue. g) Reciprocal lattice and Brillouin zone with reciprocal lattice parameters* $b_1$ *and* $b_2$*, showing Dirac points K and K' at the Brillouin zone corners, as well as M, the midpoint of the zone edge and Γ, the zone center. Scale bars 100 µm (d) and 5 Å (e). Adapted*[1]

After the invention of the transistor and the inception of the semiconductor industry, computer technologies have progressively improved at a staggering pace, as dictated by Moore's law, with high precision feature sizes now below 10 nm. The entire electronics industry has seen amazing inventions over the decades and the turn of the century, contributing to communications, optoelectronics, photovoltaics, sensors, light emitters and more. Silicon has been the cornerstone of many of these technologies, particularly integrated circuitry, which continues to see exponential growth. While new processing techniques enable breakthroughs in order to surpass technological barriers and roadblocks, we will eventually reach the ultimate scale limits of these nanotechnologies. Evolutionary incremental improvements will slow as the extreme miniaturization reach their fundamental physical limits; newer, more novel strategies will be necessary to supplant the traditional semiconductor paradigms. Soon, new materials and processing techniques will be required, along with advanced and unconventional device designs essential to fueling the future computing demands of society as technology becomes more and more integrated into our lives.

Graphene and other 2DLMs offer promising opportunities for designing more powerful and uniquely capable nanodevices for future electronics. With these properties will come advances that traditional, top-down approaches are not capable of. The precise control of these materials, and integration into current commercial applications presents a difficult roadblock towards realizing practical application. The extraordinarily unusual properties of 2DLMs are what lead to the future promises of these as research expands into both the fundamental properties and how they can be implemented into and enhancing existing processing and fabrication technologies.

## 1.1 Electronic properties of graphene and devices

Graphene has been studied theoretically long before it was experimentally isolated in a lab in 2004; the honeycomb structure in graphite is well known from x-ray diffraction (XRD), but it was unknown if a monolayer of graphene would be stable on its own, let alone how to isolate it from bulk graphite. The electronic band structure of graphene approaches linearity at the Fermi level ($E_F$), forming a cone at the so-called Dirac point, which provides it with extraordinary intrinsic properties, such as high carrier mobility and a unique pseudospin (an additionally chiral dimension) in its theoretical form. Graphene is therefore a semimetal with symmetric hole (*p*-type) an quasiparticle electrons (*n*-type) mobility, that can be doped with an external electric field to induce charge carries, as shown in Figure 1.2a. Extrinsically however, external factors introduce various complications from its pristine state and away from its pure linear dispersion properties, for example impurities on the surface cause localized shifts if the Fermi level, stunting the full performance benefits of the pristine material, as demonstrated in *I*–*V* measurements in Figure 1.2b. The green curve shows a 'V' shape for the conductivity vs. applied electric field, while the magenta curve shows the resistivity which peaks at the Dirac point of 0 applied field. To the left and right of the Dirac point are the *p*- and *n*-type regions where holes and electrons are the majority carriers respectively.

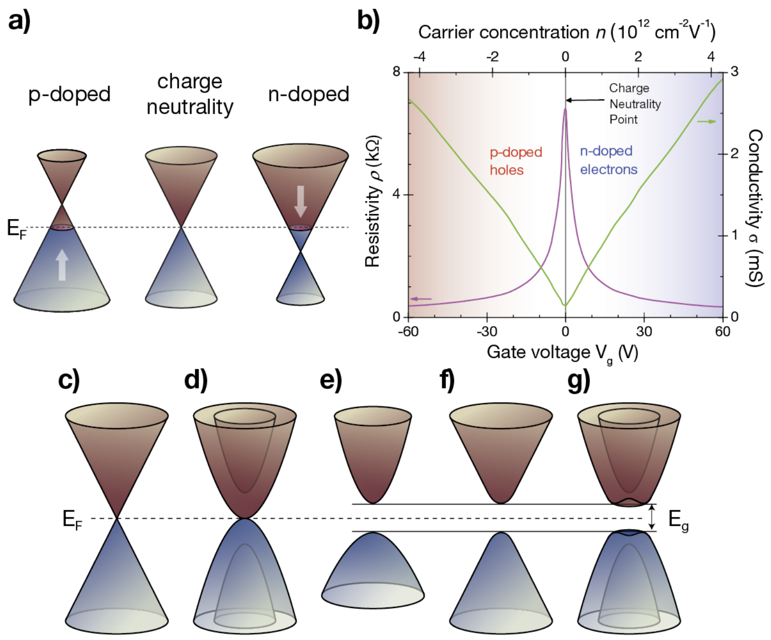

*Figure 1.2 – Graphene based field effect transistors*

*a) Schematic of band structure shift as an electric field (i.e. gate voltage) dopes the graphene Fermi level above and below the Dirac point. b) Typical resistivity/conductivity measurements as a function of gate voltage for graphene, showing the ambipolar nature as conduction switches between the hole (left) and electron (right) regimes, separated by the charge neutrality (Dirac) point where the resistance reaches its maximum. Band structures near the Fermi energy level $E_F$ with bandgap $E_g$ of monolayer (c) and bilayer (d) graphene, conventional direct bandgap semiconductors (e), and bandgap-induced monolayer (f) and bilayer (g) graphene. Adapted[1]*

The linear dispersion at the Dirac point give graphene a unique semimetallic, zero-gap band structure and makes it electronically tunable in ways different than most other materials. Figure 1.2c-g shows the various band structures around the Dirac point for pristine monolayer graphene (c), bilayer graphene (d), conventional direct bandgap semiconductors (e), a quantum confined graphene nanoribbon (f), and electronic field induced bandgap in bilayer graphene (g). One major difficulty in utilizing the fast carrier mobility in graphene is that creating a substantial bandgap will inherently curve the band structure at the Dirac point, and inevitably reduce the speed at which a transistor can switch off and on, limiting its use as a digital logic device (i.e. in a microprocessor). It can still be used in high-speed communications processing as an analog device with exceptionally high switching speeds due to the high mobility. However, in order to be used in digital logic circuitry such as computer processors, a bandgap must exist, making bandgap engineering of graphene critical. Methods such as quantum confinement in a graphene nanoribbons (analogous to semiconducting carbon nanotubes) is a popular approach,[10] though other factors such as edge effects and Coulomb blockades due to substrate induced energy wells complicate the physics.[11] An additional unique aspect of graphene electronics is the chiral pseudospin that emerges from the symmetric $K$ and $K'$ Dirac points within the crystal structure basis (Figure 1.3), which has spawned a new field called valleytronics, similar to spintronics using this additional degree of freedom.

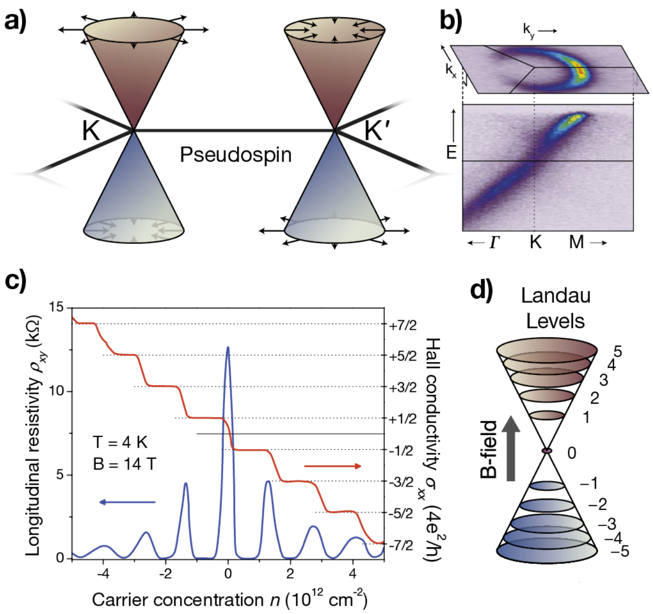

*Figure 1.3 – Pseudospin and landau levels in graphene*
*a) Dirac cones showing pseudospin as it rotates with respect to reciprocal space and the inverted orientation between the two valleys. b) Angle-resolved photoemission spectroscopy (ARPES) map of the pseudospin, horizontal cross section (upper) tilted perpendicularly to a vertical cross section (lower) of a Dirac cone observed experimentally using spherically polarized photons. c) Hall resistance measurements, showing quantized peaks and plateaus of the d) Landau levels for the anomalous and fractional QHE in graphene, labeled with the quantum number index. Adapted*[1]

Raman scattering spectroscopy is popular tool for analyzing the structure of materials by exposing its surface to excitation photons and observe reduced energy emissions due to energy transferred to phonons within a sample such as graphene.[12-14] 2DLMs tend to have a large area, making them conducive to being studied using spectroscopic analysis. Pristine monolayer graphene has characteristic peaks *G* and *2D* (Figure 1.4), while incorporating defects or dangling bonds introduces additional peaks, *D* and *D'*. Additional layers also include additional peaks within the *2D* modes as additional phonon interactions occur. These characteristics make Raman an incredibly useful tool for analyzing the structure and crystal quality of graphene and other

2DLMs which haver comparable peak behavior, such as the $A_{1g}$ and $B_{2g}$ peaks in TMDs.[15] Raman spectroscopy is an indispensable tool for quick, non-destructive characterization of 2DLMs, capable of determining properties such as the number of layers, material quality and presence of defects and edges, as well as degree of functionalization and other modifications. Additionally, as discussed later in Section 1.3, the strain will also influence the Raman spectra, making it capable of analyzing the strain profile within the membrane.

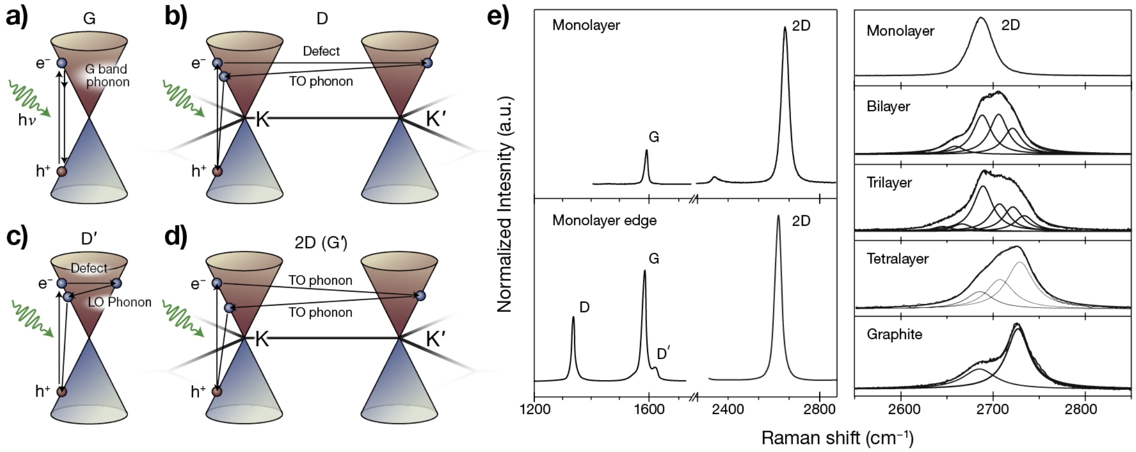

*Figure 1.4 – Characteristic peaks of Raman shift in graphene*
*Schematic band diagrams of Raman resonance pathways for a) G, b) D, c) D', and d) double resonance 2D (G') peaks of monolayer graphene. e) Raman spectroscopy of pristine (upper left) and at an edge (lower left) of a monolayer, showing D, G, D' and 2D (G') peak heights and 2D peaks of 1 through 4 layers and bulk graphite (right), showing the broadened full width half max (FWHM) and multipeak fits for multilayers. Adapted (a-d)*[1] *and (e)*[13]

## 1.2 Two dimensional layered materials and heterostructures

As with graphene, reducing the crystallinity of layered materials to two dimensions uncovers unique properties and enhanced capabilities.[16] Bulk materials have different material properties from their nanostructured forms, and in this case isolated mono and few-layered nanosheets. Here, the dangling bonds on the layer surface are exposed to van der Walls interactions with the environment, and the layers are able to bind well to other materials without issues like lattice mismatch of covalent bonds. This enables a wide variety of compatible materials and a mix-match approach to heterostructure formation and re-stacking of the 2DLMs for complex devices with novel designs, e.g. tunneling transistors[17] and barristors.[18] The ultra-thin structure and high durability enable for highly flexible devices for a new age of soft, bendable electronics.

Despite its many attractive properties and the unique platform for scientific and engineering advancements, graphene has limitations in many respects. Expanding on the semimetal nature of graphene, substituting elements for carbon enables a range of semiconducting (i.e. transition metal dichalcogenides and phosphorene) and insulating materials (i.e. boron nitride) as shown in Figure 1.5a. This array of layered materials to choose from enables all kinds of versatile electronic devices and integrated circuitry through heterogenous integration of atomically thin layers.

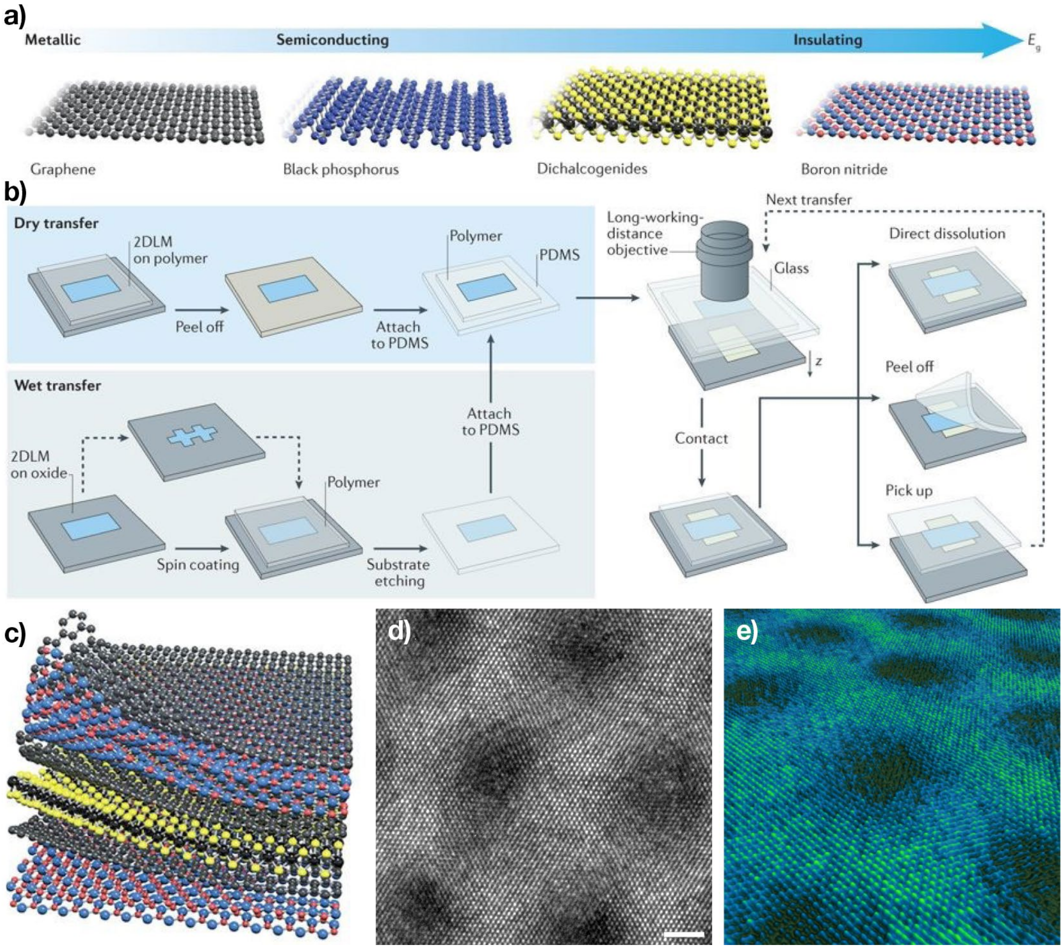

*Figure 1.5 – Two-dimensional layered material–based van der Waal heterostructures a) 2DLMs of various elements, structure, and electronic properties from metallic to semiconducting to insulating. b) Schematic illustration of the alignment transfer processes for precise heterostructure integration show both wet and dry techniques. c) Van der Waal Heterostructures (vdWHs) can take many forms, by combining materials without covalently bonding them and mixing and matching into designer stacks. d) TEM image of the Moiré patterns appear in vdWHs of stacked 2DLMs with slight mismatch in lattice parameter and e) an artistic depiction of the pattern. Scale bar 2 nm (d). Adapted*[9]

The van der Walls bonded nature of these layered materials makes offers advantages over other nanostructures that are typically plague by dangling bonds and trap states at the surface interface. With fully saturated chemical bonds, the interlayer van der Waals forces allow for good integration with various materials with zero-dimensional (e.g. nanoparticles, quantum dots, or fullerenes) [19] and one-dimensional (e.g. nanowires, nanotubes, or nanoribbons) [20] materials, as well as other 2DLMs[21] (Figure 1.5c) and even bulk materials.

Hexagonal boron nitride (BN), also called white graphite, is an insulating complement to graphene with a large bandgap due to boron and nitrogen atoms replacing the carbon atoms of the honeycomb lattice. These uniform and thin sheets have been used as defect-free, ultraflat substrates for higher performance electronics[21], an ultrathin dielectric material or tunneling barrier for graphene devices, [22] such as in tunneling transistors, and as an encapsulation material to isolate the active materials form the environment[23]. Additional research has explored hybrid systems of boron, carbon and nitrogen within individual layers to modify its electronic properties for bandgap engineering *p*- and *n*-type doping, and potentially designed circuitry within a single sheet.

Semiconductor 2DLMs are fit between graphene and BN with a moderately sized bandgap, such as transition metal dichalcogenides (TMDs), which are layered compounds comprised of a transition metal (e.g. molybdenum or tungsten) paired with chalcogenides (e.g. sulfur or selenium). The stoichiometry of the chalcogenides means they are split out of the plane, forming a thicker layer than one atom. They also tend to have a semiconducting indirect bandgap which transitions to a direct bandgap in monolayer form. Notably, bulk molybdenite ($MoS_2$) is found in nature and can be mechanically exfoliated into monolayers just as graphene is with the tape peeling method. These materials are very promising as they are already semiconducting without modification and offer variability in the combination of elements that are stable in monolayer form. Another more recent semiconducting 2DLM is black phosphorus is an allotrope of phosphorus with a layered material, with a similar honeycomb-like crystal structure where the atoms are staggered (Figure 1.5). Many other 2DLMs of other more configurations exist, such as MXenes[24] and more complex compounds, which have a wide range of properties and unique advantages, allow a large range of possibilities for combining into vdWHs. Though there is a large range of 2DLMs of varying complexity, even simple ones, however, have various limitations. For example, experimentally grown, atomically thin sheets of silicon or boron, named silicene[25] and borophene[26] respectively, are much less stable and have yet to be isolated from their growth substrate.

Two primary techniques for consistent fabrication of vdWHs (aside from directly growing them) is by using wet and dry transfer methods from a sacrificial substrate (Figure 1.5b). Wet and dry transfer techniques are used to attach the target sheet to the stamp material. The stamp is then attached to a glass slide and placed in a transfer microscope. Micromanipulators allow for the precise alignment of sheets using a long-working-distance objective lens. The polymer transfer stamp can either be chemically dissolved away, mechanically peeled off or used to pick up the entire stack for further transfer steps.

## 1.3 Strain engineering and nanoscale origami

When materials are deformed, the strain within the atomic structure causes changes to the properties; by engineering precise control over these changes, strain can be a powerful tool which is useful in a number of applications, and in particular electronics.[27] Graphene and other 2DLMs are mechanically stable membranes that can readily deform in unique ways at the nanoscale.[28] Strain-engineering of utilizes the coupling of the electronic and mechanical properties to precisely control what electronic behavior may result, and then integrate this into functional devices.[29] The main idea is that stretching, bending and folding the atomic membranes rather than slicing them in a type of nanoscale origami can yield complex results with tailored properties by controlling the nanostructure. For graphene in particular, a transport gap is theoretically possible by asymmetrically straining the lattice (Figure 1.6c-f).[30] The deformation of the lattice creates gauge fields with an altered electronic structures; the resulting electrons behave as if they are traveling in a fictitious (‘pseudo’) magnetic field with distinct Landau levels (Figure 1.6a and b) equivalent to quantum hall effect measurements. Triaxial strain in graphene is theorized to produce pseudomagnetic fields in graphene, behaving as if there is an effective, but net zero magnetic field.[31] Scanning tunneling spectroscopy (STS) experiments have observed this phenomenon in nanobubbles that form in chemical vapor deposition (CVD) graphene on platinum as it cools, with pseudomagnetic fields as large as 300 T in the highest strained nanobubbles.[32] Previously, this so-called strain engineering has been utilized to increase the mobility of silicon in devices for decades , as well as used in more recent studies such as inducing a bandgap in carbon nanotubes.[33]

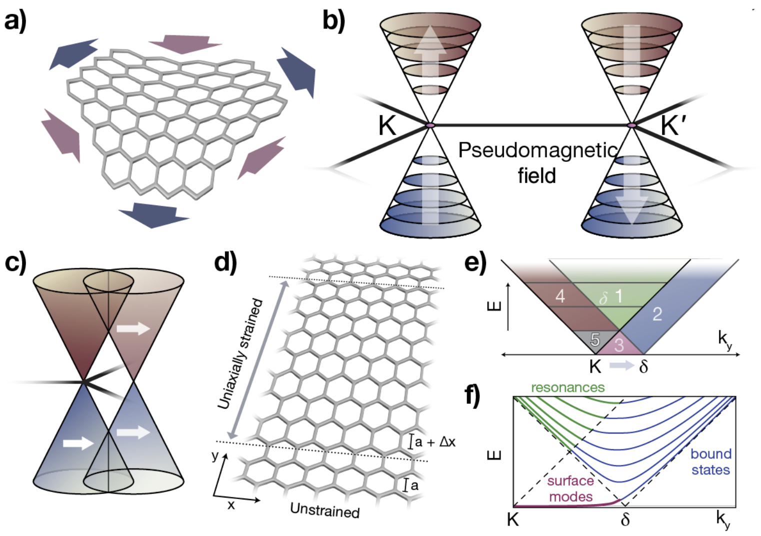

*Figure 1.6 – Effects of strain on the electronic properties of graphene*
*a) Triangularly symmetric strain profile that produces gauge fields and in turn pseudomagnetic effects in graphene. b) Band structure showing the opposing directions of the pseudomagnetic field on each sublattice point, with quantized Landau levels, and no net field. c) Schematic diagram of uniaxial strain induced shifting of the Dirac cones. d) A region of uniaxial strained graphene separates two unstrained regions, creating a transport gap between the two misaligned Dirac cones. e) Overlapping cones showing regions of possible states through a barrier of uniaxially strained graphene: 1) scattering states, 2) band states within the strained region, 3) localized states at boundary, 4) filtered states, and 5) filtered, evanescent waves. f) The resonant bands between the unstrained and strained region, and surface modes that appear at the junction, similar to the edge states of a nanoribbon. Adapted*[1]

So far it has been difficult to actualize enough controlled strain to induce a bandgap, and even so, the regions with a gap must encompass the entire channel region where electrons could otherwise transport through regions without a gap, making it logistically difficult to design experiments to observe the carrier transport. Many approaches have been proposed and implements to introduce strain into these materials with varying success. One technique, using a device with a suspended graphene ribbon channel is indented into the empty space within the substrate using an *in situ* nanoindenter inside an SEM was only capable of only 1% strain, which was not enough to observe a significant change in transport properties.[34] The necessary strain needed could be reduced in theory by introducing a scalar potential field.[35] Another approach is by thermal expansion mismatch: as the substrate cools, if the membrane is pinned through adhesion or otherwise, it will strain the lattice and buckle out of plane into ripples, blisters, and bubbles if enough stress builds up.[32]

A number of theoretical and experimental studies demonstrate these fundamental capabilities using a wide range of methods (Figure 1.7), from nanoindentation,[34] piezoelectrics,[36] pressure differentials,[37,38] thermal expansion,[32,39,40] prestrained elastomers[41,42] patterned substrates,[43-45] lattice mismatch[46,47] and defect engineering[48]. Graphene, along with other two-dimensional materials, opens up novel technological abilities that stretch the capabilities of current nanotechnology, in particular electronics. Its atomic thinness allows for great flexibility, which also makes its properties sensitive to physical manipulation. It is important to understand the intricate relationship between physical distortions and the resulting electronic behavior. One major attraction of straining graphene is to induce a bandgap in this otherwise zero bandgap semimetal,[7] or at least induce some sort of energy or transport gap[30] which can be used for digital logic transistors or other bandgap-dependent applications. Nonetheless, many opportunities arise through the various methods used to manipulate graphene beyond its pristine form. Both the mechanical strength and malleability of graphene make it ideal for incorporating strain. The essential aspect of our approach is the generation of strain in the graphene lattice that is capable of changing the in-plane hopping amplitude in an anisotropic way to induce a transport gap (Figure 1.6c-f).[30,49,50] Another way to compress the substrate is using thermal expansion. Graphene has an unusual negative thermal expansion coefficient in certain cases, so in the event of cooling graphene pinned to a substrate, the contraction of the substrate (and lack of it in the graphene) will force graphene to buckle, as seen in STM images of highly strained nanobubbles of graphene on Pt.[32] The bubbles conform to the three and six-fold symmetries of the honeycomb lattice, forming triangular and hexagonal pyramid-like structures. A key component to this approach is the adhesion of graphene to the substrate in order for it to buckle properly. In addition to the unique pseudomagnetic effect, theoretical valleytronic devices (controlling the valley-isospin/pseudospin degree of freedom) may be obtainable by using localized strain.[51,52] Engineering barriers via regions of strain could also prove useful for waveguiding of electrons in graphene that behave like light packets, and can be further extended to photonics and metamaterials. Micromechanical actuators may also be created based on a light or electricity driven graphene membrane vibrating at microwave frequencies.[53]

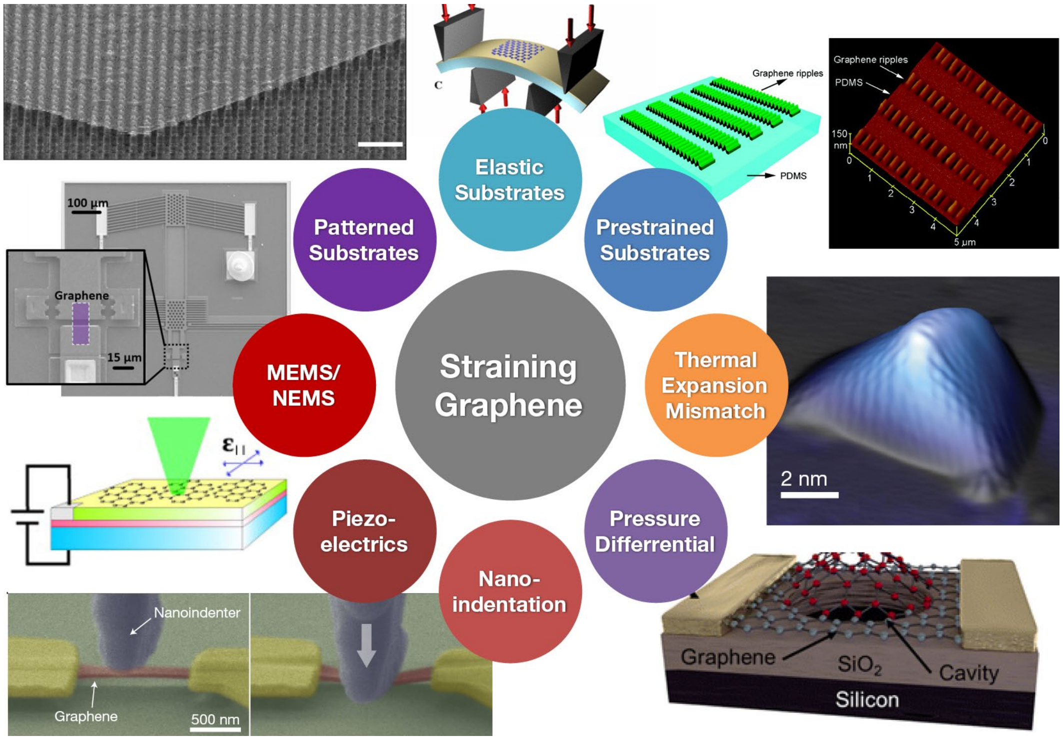

*Figure 1.7 – Methods of straining graphene membranes*
*Elastic substrates: by bending and stretching the material supports the graphene. Prestrained substrates: cause wrinkles in compressed graphene after relaxation of the prestrain. Thermal expansion mismatch: using the shrinking substrate while cooling to compress graphene due to the low thermal expansion of graphene. Pressure differential: microcapsules sealed by suspended graphene forms a bubble due to the difference in pressure across the impermeable membrane. Nanoindentation: graphene suspended over a trench that is then strained into the trench using an in situ nanoindenter or AFM tip. Piezoelectrics: biaxial strain with applied voltage to a piezoelectric substrate. MEMS/NEMS: micro and nanoelectromechanical systems form a microscopic straining apparatus. Patterned substrates: transferring graphene onto periodically structured topographic substrates.*

A number of early studies investigate the effect that uniaxial[54,55] and biaxial[36] strain has on the characteristic Raman peaks. In agreement with theoretical models, experimental measurements show that tension leads to a redshift of the *G* and *2D* peaks due to a phonon softening as the Dirac cones are shifted, and likewise a phonon hardening leads to a blueshift when in compression.[38,56,57] The linear relationship of the shifting in peak position and the applied strain allows calculation of strain via the measured Raman spectrum. In strain systems that do no preserve biaxial symmetry (i.e. uniaxial strain), the asymmetry changes the lattice shape, leading to a split in the $G$ peak into $G^+$ and $G^-$ sub peaks that are normally doubly degenerate as a single peak; and to a lesser degree, the $2D$ peak can also split into $2D^+$ and $2D^-$ sub peaks. The split is dependent on the angle of strain relative to the lattice, making it possible to determine the orientation of the crystal, and the misoriented domains within CVD graphene.[58] Typical values of $\partial\omega/\partial\varepsilon$ for uniaxial strain of the $G^+$ and $G^-$ are 33 $\mathrm{cm}^{-1}$/% and 15 $\mathrm{cm}^{-1}$/%, respectively, where $\omega$ is the shift in peak position and $\varepsilon$ is the strain.[59] For the $2D$ peak shift with uniaxial strain in the armchair direction, typical orientation dependent values are 63.1 $\mathrm{cm}^{-1}$/% and 44.1 $\mathrm{cm}^{-1}$/% for the $2D^+$ and $2D^-$ peaks respectively which is roughly double that of the $G$ band.[60] Additionally, by using polarized Raman, the strain orientation of the sample can be determined.[61] Similarly, TMDs such as $MoS_2$ have strain-dependent Raman spectral peaks, as well as a dependent photoluminescence, as the bandgap shifts and has direct–indirect transitions.[62-64] The $A'$ mode (403 $\mathrm{cm}^{-1}$) due to out-of-plane vibrations do not show a shift, while the $E'$ mode (384 $\mathrm{cm}^{-1}$) due to in-plane vibrations splits into $E'^+$ and $E'^-$, calculated to be 1.0 $\mathrm{cm}^{-1}$/% and 4.5 $\mathrm{cm}^{-1}$/% respectively using first principals.[62]

Origami, the ancient Japanese art of paper folding, has been around for centuries, but over the last few decades has seen a profound renaissance. From children's activities to the ingenious works of art by pioneers like Robert Lang, this practice can be enjoyed by everyone. With the advent of computational origami and robotic paper folding, this art has transcended its early beginnings with increasing complexity in design. Even more recently, it has been applied to scientific fields for the creation of macroscopic and microscopic origami structures for various applications. A top-down approach to nanoscale origami uses two-dimensionally patterned thin films that out-of-plane into 3-D structures for applications such as supercapacitors and electromechanical systems (Figure 1.8).[65,66] A novel and inspirational bottom-up technique is DNA origami: an analogous approach of engineering strands of DNA to self-organize into specific structures.[67] Here we present methods of stretching, straining, bending and folding 2DLMs inspired by the concepts of origami.

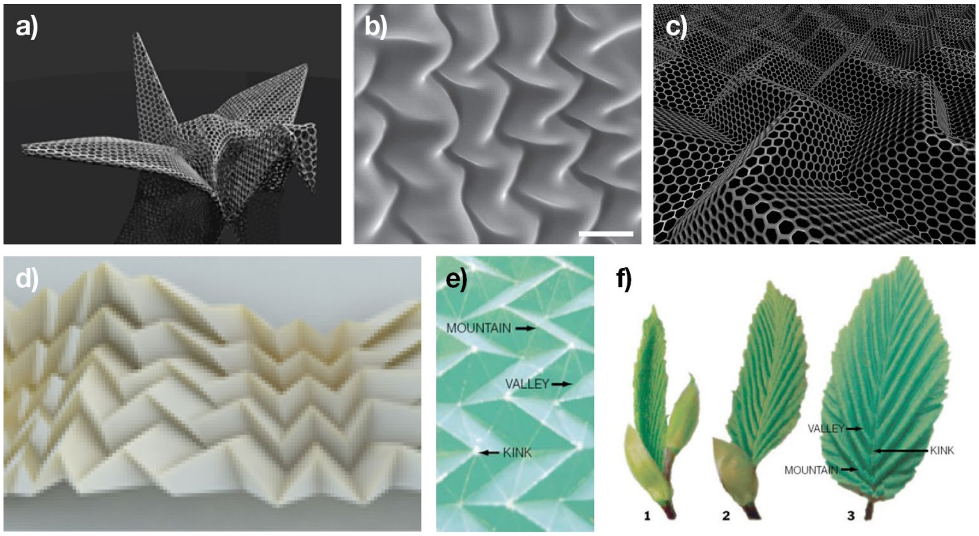

*Figure 1.8 – Nanoscale origami and the Miura-ori pattern*
*a) Artistic representation of an origami 'flapping bird' pattern folded from graphene. b) Self assembled herringbone pattern on a biaxially compressed surface. c) Artistic representation of graphene herringbone structures. (d,e) Miura-ori fold pattern and inspirational folding leaf structures (f). Scale bar 10 µm (b). Adapted (b,e,f)*[68]

Graphene represents the ultimate limit of scaling down paper to its thinnest form. Its membrane-like structure allows it to conform to various shapes or surfaces, and along with its superior mechanical properties, make it an ideal candidate for origami at the smallest scales. Graphene edges, like the sharp curves in the wall of a nanotube, are known to fold and roll with an extremely small radius of curvature, and it will also stack onto of itself or crumple up. Van der Waals forces between layers can hold more complex structures together but are relatively weak and enable unfolding capabilities and reversible processes. With this paper art analogy, this origami electronics where the membrane is altered from strain in the mechanical deformation and structural folding to tailor the electronic properties for function devices and circuits.[69,70] Corrugations appear naturally within graphene as it conforms to a rough substrate, or if suspended with no structural support, and the edges are also susceptible to rolling up. Typically, these are considered flaws within the otherwise pristine nature of graphene in its ideal form that many of its extraordinary properties are realized from; however, folds and local deformation can be engineered to control unique properties.

Graphene is very prone to wrinkles, both when suspended and supported on substrates. Typically, this is undesirable, but if it can be controlled, it could lead to novel methods of incorporating bends and folds into graphene. Wrinkles can be found at all scales in nature, from angstrom scale corrugations in graphene grown on ruthenium,[71] to as large as plate tectonics of the Earth's crust. The wrinkles are typically caused by strain in a rigid thin film that is forced to buckle in order to lower its free energy. Therefore, a useful approach to controlling such wrinkles is by compressing a flexible substrate in which graphene is bound. A common method to wrinkle such thin films is to mechanically pre-strain the flexible substrate in tension before the deposition of the film, and then relaxing the substrate, allowing the substrate to contact and the film (graphene) to buckle. Depending on the strain profile, various buckling morphologies can be achieved such as waves/corrugations with uniaxial strain,[41] or a Miura-ori-like pattern (Figure 1.8) with biaxial strain.[68]

A few methods of bending and folding these nanoscale membranes that have been developed include coupling graphene onto both oganic and inoganic subsrates and then deforming them. Patterns of alternating morphologies or chemical composition create strain and deformation both within and out of the two-dimensional plane, such as creating a microscale hinge structure. Actuation methods include lattice mismatch, ion implantation induced stress, electric or magnetic field-induced forces, and laser-based actuation. Epitaxially grown layers with slightly different lattice parameter with the substrate will induce latteral strain at the interface[72,73] When the layer is decoupled from the surface, the membrane will bend and buckle out of plane with enough stress in order to release the strain. Further engineered substrates with regions of prestrain can be used to fold and bend thin films after the prestrain is released from the underlying substrate in a controlled way. Figure 1.9a-d shows schematics of the process, where a sacrificial layered is chemically removed allowing regions to bend out of the plane into folds and scrolls, which have been demonstrated with other thin film materials.[73,74] For example, graphene-based biomorphs have also been used to form micron scale tetrahedra for autonomous origami machines controlled by pH level,[75] folded graphene nanoscale polyhedra on $Al_2O_3$ frames,[76] and temperature driven self-folding of functionalized graphene.[77] Theoretical models predict the use of hydrogenation of graphene hinges to form cubic cages.[78] The scrolls form a tube-like structure, though with a grapheme layer it would be different than a nanotube in that it does not reconnect the lattice but rather wrap back on itself. An intriguing potential technique proposed to scroll graphene is to use an electric dipole within a nanoribbon: nanowire electrodes suspended above the ribbon, which is clamped at only one end, will create an adjustable electric field that will cause the ripple to curl. A benefit of these techniques is that the folding can be performed in parallel, as well as have sequential steps that use different sacrificial materials. Creating an array of scrolls can form a periodic lattice for uses in photonic crystal metamaterials if on a similar scale to the wavelength of light.

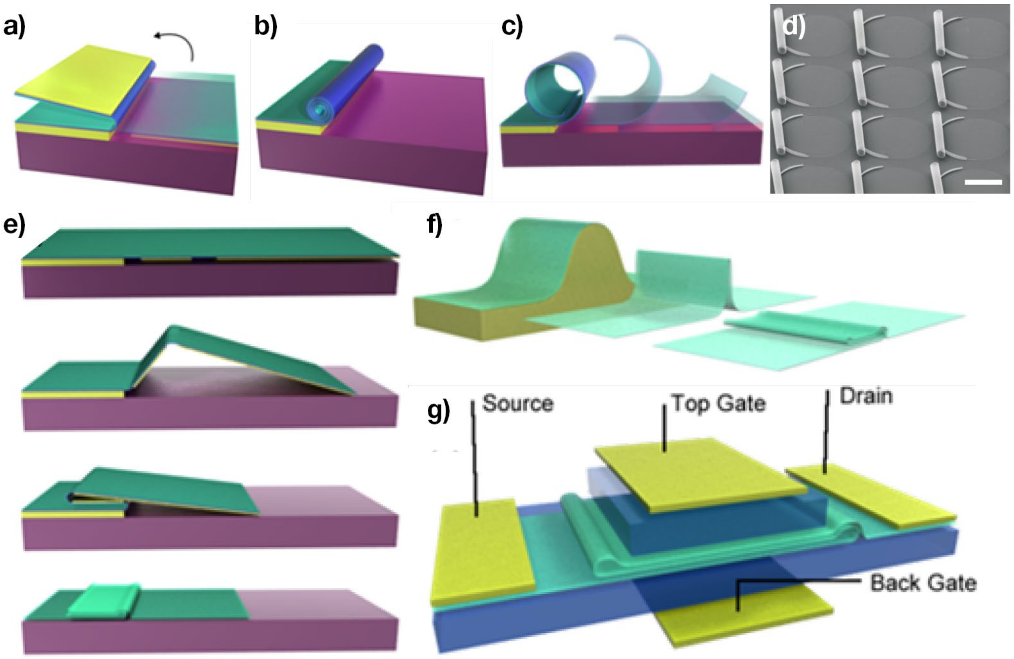

*Figure 1.9 – Graphene origami: folding and rolling nanosheets*
*Prestrain in thin films used for folding and scrolling graphene: (green) on a prestrained thin film (blue) and a rigid support substrate (yellow) with sacrificial etching layer (red). a) Schematic of folding graphene on a prestrained hinged structure. b) and c) Schematic illustration of scrolling of graphene on a sacrificial layer by etch releasing a strained bilayer (graphene attached on or below the strained thin film), causing it to scroll. d) SEM images of an array of photolithographically released scrolls of a polymer membrane. e-g) Creating creases and multiple folds in graphene membranes and formation of a single–multiple layer graphene junction. This structure can be obtained by e) nanoscale origami or f) CVD growth of graphene on a topographic substrate and then etching away the metal catalyst (or transferring graphene onto a topographic substrate and then etching away the topographic support) to allow graphene collapse into multi-folds. g) Schematic of a proposed dual gated "trilayer" folded graphene transistor. Scale bar 20 µm (d). Adapted (d)*[73]

Taking this mechanism further by introducing multiple folds, e.g. trifolds (Figure 1.9e-g) which are found from the natural creases that develop through transferring of layers have been studied before but not easily controllable.[79,80] These more complex layering may lead to opportunities to tailor properties beyond simple straining; since the junction at the transition from single to trilayer, confinement effects can arise from the finite size of the multilayer region in addition to the potential formation of bandgaps in multilayers. Furthermore, the stacking order of ordinary multilayers (i.e. Bernal stacking) is distinct from misoriented restacking of individual sheets and is an important consideration, as slight misorientations can lead to modification of the band structure.[81] Other interesting opportunities include materials can also be incorporated and place inside the folded region or functionalized molecules along the exposed curve with increased activity. A small bandgap arises in multilayers under certain conditions, such as a perpendicular electric field due to symmetry breaking[82] or a metal-insulator transition due to quasiparticle interactions.[83] The relative orientation between adjacent layers may also play an important role in determining the electronic properties, since it is known that the precise way atoms of different layers align gives rise to different band structures.[82,84-86] Slight misorientations of the cause lattice distortions and modify the band structure. Folds in graphene have been observed incidentally, but can also be engineered, by using patterned growth techniques or intercalation compounds.[79] Simulations show induced folds using water droplets that lower the energy barriers of folding the membrane and can help control folding morphology.[87]

## Summary

Graphene and similar 2DLMs have become an exciting topic of research with a variety of unique properties, novel advances in technology, and promising future applications. These thin yet robust membranes are very conducive for flexible electronics and suitable for advanced strain engineering. The following chapters explore the synthesis, material characterization and device fabrication utilizing these extraordinary materials. Chapter 2 demonstrates how graphene and TMDs are made, focusing primarily on scalable CVD based methods to enable scalable synthesis of high quality, large area nanosheets with controlled thickness. Chapter 3 and Chapter 4 cover two approaches towards incorporating controlled strain within graphene: applying graphene to topographically patterned substrates and compressing graphene on prestrained substrates to form nanoripples. Finally, a number of devices made using these materials is covered in Chapter 5, including flexible, high-speed TMD channel transistors and graphene used as a tunable contact electrode, with concluding remarks in Chapter 6.

## References

1. Weiss, N. O., Zhou, H., Liao, L., Liu, Y., Jiang, S., Huang, Y. & Duan, X. "Graphene: An Emerging Electronic Material" *Advanced Materials* **24**, 5782-5825 (2012)

2. Liao, L., Lin, Y.-C., Bao, M., Cheng, R., Bai, J., Liu, Y., Qu, Y., Wang, K. L., Huang, Y. & Duan, X. "High-speed graphene transistors with a self-aligned nanowire gate" *Nature* **467**, 305-308 (2010)

3. Cheng, R., Bai, J., Liao, L., Zhou, H., Chen, Y., Liu, L., Lin, Y.-C., Jiang, S., Huang, Y. & Duan, X. "High-frequency self-aligned graphene transistors with transferred gate stacks" *Proceedings of the National Academy of Sciences* **109**, 11588 (2012)

4. Kim, K. S., Zhao, Y., Jang, H., Lee, S. Y., Kim, J. M., Kim, K. S., Ahn, J.-H., Kim, P., Choi, J.-Y. & Hong, B. H. "Large-scale pattern growth of graphene films for stretchable transparent electrodes" *Nature* **457**, 706-710 (2009)

5. Sun, D.-M., Liu, C., Ren, W.-C. & Cheng, H.-M. "A Review of Carbon Nanotube- and Graphene-Based Flexible Thin-Film Transistors" *Small* **9**, 1188-1205 (2013)

6. Yan, C., Cho, J. H. & Ahn, J.-H. "Graphene-based flexible and stretchable thin film transistors" *Nanoscale* **4**, 4870-4882 (2012)

7. Castro, E. V., Ochoa, H., Katsnelson, M. I., Gorbachev, R. V., Elias, D. C., Novoselov, K. S., Geim, A. K. & Guinea, F. "Limits on Charge Carrier Mobility in Suspended Graphene due to Flexural Phonons" *Physical Review Letters* **105**, 266601 (2010)

8. Lee, C., Wei, X., Kysar, J. W. & Hone, J. "Measurement of the Elastic Properties and Intrinsic Strength of Monolayer Graphene" *Science* **321**, 385-388 (2008)

9. Liu, Y., Weiss, N. O., Duan, X., Cheng, H.-C., Huang, Y. & Duan, X. "Van der Waals heterostructures and devices" *Nature Reviews Materials* **1**, 16042 (2016)

10. Bai, J. & Huang, Y. "Fabrication and electrical properties of graphene nanoribbons" *Materials Science and Engineering: R: Reports* **70**, 341-353 (2010)

11. Gallagher, P., Todd, K. & Goldhaber-Gordon, D. "Disorder-induced gap behavior in graphene nanoribbons" *Physical Review B* **81**, 115409 (2010)

12. Ferrari, A. C., Meyer, J. C., Scardaci, V., Casiraghi, C., Lazzeri, M., Mauri, F., Piscanec, S., Jiang, D., Novoselov, K. S., Roth, S. & Geim, A. K. "Raman Spectrum of Graphene and Graphene Layers" *Physical Review Letters* **97**, 187401 (2006)

13. Malard, L. M., Pimenta, M. A., Dresselhaus, G. & Dresselhaus, M. S. "Raman spectroscopy in graphene" *Physics Reports* **473**, 51-87 (2009)

14. Bendiab, N., Renard, J., Schwarz, C., Reserbat-Plantey, A., Djevahirdjian, L., Bouchiat, V., Coraux, J. & Marty, L. "Unravelling external perturbation effects on the optical phonon response of graphene" *Journal of Raman Spectroscopy* **49**, 130-145 (2018)

15. Saito, R., Tatsumi, Y., Huang, S., Ling, X. & Dresselhaus, M. S. "Raman spectroscopy of transition metal dichalcogenides" *Journal of Physics: Condensed Matter* **28**, 353002 (2016)

16. Zhang, H. "Ultrathin Two-Dimensional Nanomaterials" *ACS Nano* **9**, 9451-9469 (2015)

17. Britnell, L. *et al.* "Field-Effect Tunneling Transistor Based on Vertical Graphene Heterostructures" *Science* **335**, 947 (2012)

18. Yang, H., Heo, J., Park, S., Song, H. J., Seo, D. H., Byun, K.-E., Kim, P., Yoo, I., Chung, H.-J. & Kim, K. "Graphene Barristor, a Triode Device with a Gate-Controlled Schottky Barrier" *Science* **336**, 1140 (2012)

19. Liu, Y., Cheng, R., Liao, L., Zhou, H., Bai, J., Liu, G., Liu, L., Huang, Y. & Duan, X. "Plasmon resonance enhanced multicolour photodetection by graphene" *Nature Communications* **2**, 579 (2011)

20. Liao, L., Lin, Y.-C., Bao, M., Cheng, R., Bai, J., Liu, Y., Qu, Y., Wang, K. L., Huang, Y. & Duan, X. "High-speed graphene transistors with a self-aligned nanowire gate" *Nature* **467**, 305 (2010)

21. Dean, C. R., Young, A. F., Meric, I., Lee, C., Wang, L., Sorgenfrei, S., Watanabe, K., Taniguchi, T., Kim, P., Shepard, K. L. & Hone, J. "Boron nitride substrates for high-quality graphene electronics" *Nature Nanotechnology* **5**, 722 (2010)

22. Britnell, L. *et al.* "Electron Tunneling through Ultrathin Boron Nitride Crystalline Barriers" *Nano Letters* **12**, 1707-1710 (2012)

23. Mayorov, A. S., Gorbachev, R. V., Morozov, S. V., Britnell, L., Jalil, R., Ponomarenko, L. A., Blake, P., Novoselov, K. S., Watanabe, K., Taniguchi, T. & Geim, A. K. "Micrometer-Scale Ballistic Transport in Encapsulated Graphene at Room Temperature" *Nano Letters* **11**, 2396-2399 (2011)

24. Naguib, M., Mochalin, V. N., Barsoum, M. W. & Gogotsi, Y. "25th Anniversary Article: MXenes: A New Family of Two-Dimensional Materials" *Advanced Materials* **26**, 992-1005 (2014)

25. Vogt, P., De Padova, P., Quaresima, C., Avila, J., Frantzeskakis, E., Asensio, M. C., Resta, A., Ealet, B. & Le Lay, G. "Silicene: Compelling Experimental Evidence for Graphenelike Two-Dimensional Silicon" *Physical Review Letters* **108**, 155501 (2012)

26. Mannix, A. J. *et al.* "Synthesis of borophenes: Anisotropic, two-dimensional boron polymorphs" *Science* **350**, 1513 (2015)

27. Dai, Z., Liu, L. & Zhang, Z. "Strain Engineering of 2D Materials: Issues and Opportunities at the Interface" *Advanced Materials* **31**, 1805417 (2019)

28. Kim, E.-A. & Castro Neto, A. H. "Graphene as an electronic membrane" *EPL (Europhysics Letters)* **84**, 57007 (2008)

29. Bissett, M. A., Tsuji, M. & Ago, H. "Strain engineering the properties of graphene and other two-dimensional crystals" *Physical Chemistry Chemical Physics* **16**, 11124-11138 (2014)

30. Pereira, V. M. & Castro Neto, A. H. "Strain Engineering of Graphene's Electronic Structure" *Physical Review Letters* **103**, 046801 (2009)

31. Settnes, M., Power, S. R. & Jauho, A.-P. "Pseudomagnetic fields and triaxial strain in graphene" *Physical Review B* **93**, 035456 (2016)

32. Levy, N., Burke, S. A., Meaker, K. L., Panlasigui, M., Zettl, A., Guinea, F., Neto, A. H. C. & Crommie, M. F. "Strain-Induced Pseudo–Magnetic Fields Greater Than 300 Tesla in Graphene Nanobubbles" *Science* **329**, 544 (2010)

33. Maiti, A. "Carbon nanotubes - Bandgap engineering with strain" *Nature Materials* **2**, 440-442 (2003)

34. Huang, M., Pascal, T. A., Kim, H., Goddard, W. A. & Greer, J. R. "Electronic−Mechanical Coupling in Graphene from in situ Nanoindentation Experiments and Multiscale Atomistic Simulations" *Nano Letters* **11**, 1241-1246 (2011)

35. Low, T., Guinea, F. & Katsnelson, M. I. "Gaps tunable by electrostatic gates in strained graphene" *Physical Review B* **83**, 195436 (2011)

36. Ding, F., Ji, H., Chen, Y., Herklotz, A., Dörr, K., Mei, Y., Rastelli, A. & Schmidt, O. G. "Stretchable Graphene: A Close Look at Fundamental Parameters through Biaxial Straining" *Nano Letters* **10**, 3453-3458 (2010)

37. Bunch, J. S., Verbridge, S. S., Alden, J. S., van der Zande, A. M., Parpia, J. M., Craighead, H. G. & McEuen, P. L. "Impermeable Atomic Membranes from Graphene Sheets" *Nano Letters* **8**, 2458-2462 (2008)

38. Zabel, J., Nair, R. R., Ott, A., Georgiou, T., Geim, A. K., Novoselov, K. S. & Casiraghi, C. "Raman Spectroscopy of Graphene and Bilayer under Biaxial Strain: Bubbles and Balloons" *Nano Letters* **12**, 617-621 (2011)

39. Pan, W., Xiao, J., Zhu, J., Yu, C., Zhang, G., Ni, Z., Watanabe, K., Taniguchi, T., Shi, Y. & Wang, X. "Biaxial Compressive Strain Engineering in Graphene/Boron Nitride Heterostructures" *Sci. Rep.* **2**, 893 (2012)

40. Bao, W., Miao, F., Chen, Z., Zhang, H., Jang, W., Dames, C. & Lau, C. N. "Controlled ripple texturing of suspended graphene and ultrathin graphite membranes" *Nature Nanotechnology* **4**, 562-566 (2009)

41. Wang, Y., Yang, R., Shi, Z., Zhang, L., Shi, D., Wang, E. & Zhang, G. "Super-Elastic Graphene Ripples for Flexible Strain Sensors" *ACS Nano* **5**, 3645-3650 (2011)

42. Zang, J., Ryu, S., Pugno, N., Wang, Q., Tu, Q., Buehler, M. J. & Zhao, X. "Multifunctionality and control of the crumpling and unfolding of large-area graphene" *Nature Materials* **12**, 321-325 (2013)

43. Reserbat-Plantey, A., Kalita, D., Han, Z., Ferlazzo, L., Autier-Laurent, S., Komatsu, K., Li, C., Weil, R., Ralko, A., Marty, L., Guéron, S., Bendiab, N., Bouchiat, H. & Bouchiat, V. "Strain Superlattices and Macroscale Suspension of Graphene Induced by Corrugated Substrates" *Nano Letters* **14**, 5044-5051 (2014)

44. Li, T. & Zhang, Z. "Snap-Through Instability of Graphene on Substrates" *Nanoscale Research Letters* **5**, 169 - 173 (2009)

45. Lee, J.-K., Yamazaki, S., Yun, H., Park, J., Kennedy, G. P., Kim, G.-T., Pietzsch, O., Wiesendanger, R., Lee, S., Hong, S., Dettlaff-Weglikowska, U. & Roth, S. "Modification of Electrical Properties of Graphene by Substrate-Induced Nanomodulation" *Nano Letters* **13**, 3494-3500 (2013)

46. Decker, R., Wang, Y., Brar, V. W., Regan, W., Tsai, H.-Z., Wu, Q., Gannett, W., Zettl, A. & Crommie, M. F. "Local Electronic Properties of Graphene on a BN Substrate via Scanning Tunneling Microscopy" *Nano Letters* **11**, 2291-2295 (2011)

47. Merino, P., Švec, M., Pinardi, A. L., Otero, G. & Martín-Gago, J. A. "Strain-Driven Moiré Superstructures of Epitaxial Graphene on Transition Metal Surfaces" *ACS Nano* **5**, 5627-5634 (2011)

48. Lahiri, J., Lin, Y., Bozkurt, P., Oleynik, I. I. & Batzill, M. "An extended defect in graphene as a metallic wire" *Nature Nanotechnology* **5**, 326-329 (2010)

49. Ni, Z. H., Yu, T., Lu, Y. H., Wang, Y. Y., Feng, Y. P. & Shen, Z. X. "Uniaxial Strain on Graphene: Raman Spectroscopy Study and Band-Gap Opening" *Acs Nano* **2**, 2301-2305 (2008)

50. Guinea, F., Katsnelson, M. I. & Geim, A. K. "Energy gaps and a zero-field quantum Hall effect in graphene by strain engineering" *Nat. Phys.* **6**, 30-33 (2010)

51. Fujita, T., Jalil, M. B. A. & Tan, S. G. "Valley filter in strain engineered graphene" *Applied Physics Letters* **97**, 043508 (2010)

52. Zhai, F., Zhao, X., Chang, K. & Xu, H. Q. "Magnetic barrier on strained graphene: A possible valley filter" *Physical Review B* **82**, 115442 (2010)

53. Bunch, J. S., van der Zande, A. M., Verbridge, S. S., Frank, I. W., Tanenbaum, D. M., Parpia, J. M., Craighead, H. G. & McEuen, P. L. "Electromechanical resonators from graphene sheets" *Science* **315**, 490-493 (2007)

54. Mohiuddin, T. M. G., Lombardo, A., Nair, R. R., Bonetti, A., Savini, G., Jalil, R., Bonini, N., Basko, D. M., Galiotis, C., Marzari, N., Novoselov, K. S., Geim, A. K. & Ferrari, A. C. "Uniaxial strain in graphene by Raman spectroscopy: *G* peak splitting, Grüneisen parameters, and sample orientation" *Physical Review B* **79**, 205433 (2009)

55. Yu, T., Ni, Z., Du, C., You, Y., Wang, Y. & Shen, Z. "Raman Mapping Investigation of Graphene on Transparent Flexible Substrate: The Strain Effect" *The Journal of Physical Chemistry C* **112**, 12602-12605 (2008)

56. Mohiuddin, T. M. G., Lombardo, A., Nair, R. R., Bonetti, A., Savini, G., Jalil, R., Bonini, N., Basko, D. M., Galiotis, C., Marzari, N., Novoselov, K. S., Geim, A. K. & Ferrari, A. C. "Uniaxial strain in graphene by Raman spectroscopy: $G$ peak splitting, Gr\"uneisen parameters, and sample orientation" *Physical Review B* **79**, 205433 (2009)

57. Huang, M., Yan, H., Heinz, T. F. & Hone, J. "Probing Strain-Induced Electronic Structure Change in Graphene by Raman Spectroscopy" *Nano Letters* **10**, 4074-4079 (2010)

58. Jegal, S., Hao, Y., Yoon, D., Ruoff, R. S., Yun, H., Lee, S. W. & Cheong, H. "Crystallographic orientation of early domains in CVD graphene studied by Raman spectroscopy" *Chemical Physics Letters* **568-569**, 146-150 (2013)

59. Cheng, Y. C., Zhu, Z. Y., Huang, G. S. & Schwingenschlögl, U. "Grüneisen parameter of the G mode of strained monolayer graphene" *Physical Review B* **83**, 115449 (2011)

60. Yoon, D., Son, Y.-W. & Cheong, H. "Strain-Dependent Splitting of the Double-Resonance Raman Scattering Band in Graphene" *Physical Review Letters* **106**, 155502 (2011)

61. Frank, O., Tsoukleri, G., Parthenios, J., Papagelis, K., Riaz, I., Jalil, R., Novoselov, K. S. & Galiotis, C. "Compression Behavior of Single-Layer Graphenes" *ACS Nano* **4**, 3131-3138 (2010)

62. Conley, H. J., Wang, B., Ziegler, J. I., Haglund, R. F., Pantelides, S. T. & Bolotin, K. I. "Bandgap Engineering of Strained Monolayer and Bilayer $MoS_2$" *Nano Letters* **13**, 3626-3630 (2013)

63. He, K., Poole, C., Mak, K. F. & Shan, J. "Experimental Demonstration of Continuous Electronic Structure Tuning via Strain in Atomically Thin $MoS_2$" *Nano Letters* **13**, 2931-2936 (2013)

64. Hui, Y. Y., Liu, X., Jie, W., Chan, N. Y., Hao, J., Hsu, Y.-T., Li, L.-J., Guo, W. & Lau, S. P. "Exceptional Tunability of Band Energy in a Compressively Strained Trilayer $MoS_2$ Sheet" *ACS Nano* **7**, 7126-7131 (2013)

65. Reis, P. M., López Jiménez, F. & Marthelot, J. "Transforming architectures inspired by origami" *Proceedings of the National Academy of Sciences* **112**, 12234 (2015)

66. In, H. J., Kumar, S., Shao-Horn, Y. & Barbastathis, G. "Origami fabrication of nanostructured, three-dimensional devices: Electrochemical capacitors with carbon electrodes" *Applied Physics Letters* **88**, 083104-083103 (2006)

67. Rothemund, P. W. K. "Folding DNA to create nanoscale shapes and patterns" *Nature* **440**, 297-302 (2006)

68. Mahadevan, L. & Rica, S. "Self-Organized Origami" *Science* **307**, 1740-1740 (2005)

69. Tománek, D. "Mesoscopic origami with graphite: scrolls, nanotubes, peapods" *Physica B: Condensed Matter* **323**, 86-89 (2002)

70. Pereira, V. M. & Castro Neto, A. H. "Strain engineering of graphene's electronic structure" *Phys. Rev. Lett.* **103** (2009)

71. Mao, Y., Wang, W. L., Wei, D., Kaxiras, E. & Sodroski, J. G. "Graphene Structures at an Extreme Degree of Buckling" *Acs Nano* **5**, 1395-1400 (2011)

72. Schmidt, O. G. & Eberl, K. "Nanotechnology: Thin solid films roll up into nanotubes" *Nature* **410**, 168-168 (2001)

73. Mei, Y., Huang, G., Solovev, A. A., Urena, E. B., Moench, I., Ding, F., Reindl, T., Fu, R. K. Y., Chu, P. K. & Schmidt, O. G. "Versatile Approach for Integrative and Functionalized Tubes by Strain Engineering of Nanomembranes on Polymers" *Advanced Materials* **20**, 4085-4090 (2008)

74. Cho, J.-H., Keung, M. D., Verellen, N., Lagae, L., Moshchalkov, V. V., Van Dorpe, P. & Gracias, D. H. "Nanoscale Origami for 3D Optics" *Small* **7**, 1943-1948 (2011)

75. Miskin, M. Z., Dorsey, K. J., Bircan, B., Han, Y., Muller, D. A., McEuen, P. L. & Cohen, I. "Graphene-based bimorphs for micron-sized, autonomous origami machines" *Proceedings of the National Academy of Sciences* **115**, 466 (2018)

76. Joung, D., Nemilentsau, A., Agarwal, K., Dai, C., Liu, C., Su, Q., Li, J., Low, T., Koester, S. J. & Cho, J.-H. "Self-Assembled Three-Dimensional Graphene-Based Polyhedrons Inducing Volumetric Light Confinement" *Nano Letters* **17**, 1987-1994 (2017)

77. Xu, W., Qin, Z., Chen, C.-T., Kwag, H. R., Ma, Q., Sarkar, A., Buehler, M. J. & Gracias, D. H. "Ultrathin thermoresponsive self-folding 3D graphene" *Science Advances* **3**, e1701084 (2017)

78. Zhu, S. & Li, T. "Hydrogenation-Assisted Graphene Origami and Its Application in Programmable Molecular Mass Uptake, Storage, and Release" *ACS Nano* **8**, 2864-2872 (2014)

79. Kim, K., Lee, Z., Malone, B. D., Chan, K. T., Aleman, B., Regan, W., Gannett, W., Crommie, M. F., Cohen, M. L. & Zettl, A. "Multiply folded graphene" *Physical Review B* **83**, 245433 (2011)

80. Zhu, W., Low, T., Perebeinos, V., Bol, A. A., Zhu, Y., Yan, H., Tersoff, J. & Avouris, P. "Structure and Electronic Transport in Graphene Wrinkles" *Nano Letters* **12**, 3431-3436 (2012)

81. Schmidt, H., Rode, J. C., Smirnov, D. & Haug, R. J. "Superlattice structures in twisted bilayers of folded graphene" *Nature Communications* **5**, 5742 (2014)

82. Zhang, Y., Tang, T.-T., Girit, C., Hao, Z., Martin, M. C., Zettl, A., Crommie, M. F., Shen, Y. R. & Wang, F. "Direct observation of a widely tunable bandgap in bilayer graphene" *Nature* **459**, 820-823 (2009)

83. Velasco, J., Jing, L., Bao, W., Lee, Y., Kratz, P., Aji, V., Bockrath, M., Lau, C. N., Varma, C., R, S., Smirnov, D., Zhang, F., Jung, J. & MacDonald, A. H. "Transport spectroscopy of symmetry-broken insulating states in bilayer graphene" *Nature Nanotechnology* **7**, 156-160 (2012)

84. Zhou, S. Y., Gweon, G.-H., Fedorov, A. V., First, P. N., de Heer, W. A., Lee, D.-H., Guinea, F., Neto, A. H. C. & Lanzara, A. "Substrate-induced bandgap opening in epitaxial graphene" *Nature Materials* **6**, 770-775 (2007)

85. Yavari, F., Kritzinger, C., Gaire, C., Song, L., Gullapalli, H., Borca-Tasciuc, T., Ajayan, P. M. & Koratkar, N. "Tunable Bandgap in Graphene by the Controlled Adsorption of Water Molecules" *Small* **6**, 2535-2538 (2010)

86. Yu, W. J., Liao, L., Chae, S. H., Lee, Y. H. & Duan, X. "Toward Tunable Band Gap and Tunable Dirac Point in Bilayer Graphene with Molecular Doping" *Nano Letters* **11**, 4759-4763 (2011)

87. Liu, Z., Suenaga, K., Harris, P. J. F. & Iijima, S. "Open and Closed Edges of Graphene Layers" *Physical Review Letters* **102**, 015501 (2009)

# Chapter 2: Synthesis of Two-Dimensional Layered Materials

In order for graphene to be useful in engineered devices, it must be isolated and synthesized. While mechanical exfoliation (the Scotch® tape method) of pristine sheets is useful, particularly in early fundamental studies, and provides samples of extremely high quality, more scalable chemical techniques of synthesis become necessary for practical applications. A range of approaches are now used to create two-dimensional layered materials (2DLMs), using both exfoliating solutions and vapor deposition. Early studies were able to utilize intercalation compounds within graphite to separate the layers.[1] Later techniques utilize the oxidation of graphite which breaks the interlayer bonding and separates into individual sheets suspended in liquid.[2] The aqueous product can then be processed in a multitude of ways and reduced back to graphene-like arrangement, called reduced graphene oxide (rGO). Additionally, bottom up chemical synthesis using organic reactions can produce much smaller samples, including thins strips or nanoribbons.[3] Larger scale synthesis methods include are able to cover a wide area. Epitaxial layer formation of graphene on silicon carbide (SiC) surfaces with wafer scale coverage; by heating to 1200–1600 °C in ultrahigh vacuum, the Silicon at the surface sublimates leaving behind a carbon layer.[4] SiC is insulating which makes it usable as a device substrate, though it is difficult to remove the surface layer for further processing, and high quality SiC is fairly expensive.

One of the more promising methods of creating high quality single layered sheets is chemical vapor deposition (CVD) over large areas, grown on both metals such as copper, and insulators such as $SiO_2$ coated silicon wafers.[5-7] The silica coating, usually of 300 nm thickness, are commonly used, as it allows for a strong contrast between a monolayer and bare substrate making the samples easy to identify, with the added benefits of isolating the sample electronically and acting as a back-gate using conducive, highly-doped silicon wafers. The following sections explore both CVD and solution based rGO synthesis of 2DLMs and analysis of their structure and properties. CVD is used for both large area graphene on copper foils and TMDs[8] including $MoS_2$ and $WSe_2$ directly on $SiO_2$ for use in strain engineering analysis and nanoelectronic devices, while the rGO is used to create graphene paper and aerogel frame networks.

## 2.1 Chemical vapor deposition of graphene and TMDs

CVD growth of graphene and 2DLMs has emerged as a promising and indispensable tool for synthesizing large-scale and highly uniform samples that have made both advanced research and commercial applications much more feasible. Gaseous reactants form solidified monolayers as they deposit onto the substrate, a common technique in the nanoelectronics processing industry. For graphene, methane ($CH_4$) is commonly used with a carrier gas such as nonreactive argon (Ar) with a small amount of hydrogen gas ($H_2$) to facilitate the reaction. Solid sources can also be used by heating the solid reactant (even sugars and other organic compounds such as biological samples) until its gaseous form flows towards the substrate. The major innovation in CVD of graphene is utilization of a copper foil as substrate; the copper catalyzes the reaction, and when covered by the carbon monolayer, self-limits the creation of additional layers. This allows for large scale coverage across the entire copper foil with highly uniform monolayer dispersity.[9,10] A limitation, however is that multiple domains of misaligned crystals form and grow into each other, creating defects at the intersecting boundary, analogous to grains in a multicrystalline bulk material, which causes a decrease in material performance compared to exfoliated samples which lack these defects.

Large area CVD graphene for a typical batch used in the subsequent chapters is synthesized as follows made using a low pressure, copper-catalyzed reaction with a mixture of Ar, $H_2$ and $CH_4$. A 25 μm thick copper foil (Alfa Aesar), washed with 1:10 hydrochloric acid in water, rinsed with isopropyl alcohol, and blow dried with nitrogen gas. The copper foil is placed into a quartz tube within the horizontal CVD furnace and vacuum pumped to 13 μbar for 30 min. The Ar/$H_2$ gas then fills the tube at a flow of 300 sccm and heated to 1,070 °C over 25 min, followed by the diluted 500 ppm methane in hydrogen gas to begin the deposition phase and growth of the graphene monolayers. The pressure is kept between 1–1,000 mbar and the growth is terminated by quenching the quartz tube in the ambient air environment at ~200 °C/min. Large area graphene fully covering both sides of the copper foil is now available for transferring onto arbitrary surfaces[11] and is used in Chapter 3 and Chapter 4 for strain engineering experiments.

Monolayer and few-layer samples of $MoSe_2$[12] and $WSe_2$[13] crystals are grown using CVD as described in published work and reiterated here. A home-built CVD system with a horizontal quartz tube and furnace is used for the reaction. Solid selenium (Se) and either molybdenum oxide ($MoO_3$) or tungsten oxide ($WO_3$) bulk materials are placed upstream of the deposition substrate within the tube as $H_2$ carrier gas in argon is flowed through the tube with the proposed chemical equation:

$$MoO_3 + H_2 + 3\ Se \rightarrow MoSe_2 + SeO_2 + H_2O \tag{2.1}$$

$$WO_3 + H_2 + 3\ Se \rightarrow MoSe_2 + SeO_2 + H_2O \tag{2.2}$$

As seen in previous studies,[14,15] the $H_2$ gas is a critical component in the growth of nanosheets, as without it, no synthesis is observed; even just a small fraction of $H_2$ is enough to nucleate crystals and begin lateral growth of each individual layer along the surface. The $H_2$ functions in conjunction with the selenium for added reduction of the oxides, similar to the synthesis of $MoS_2$ fullerenes.[16]

Similar to graphene, the nanosheet thickness is distinguishable using optical microscopy on 300 nm $SiO_2$/Si substrates, as the contrast is enhanced by the oxide thickness, as shown in Figure 2.1a. The nanosheets seem to nucleate randomly, forming triangular structures across the surface with no preferential orientation. When monolayer coverage is high enough, individual domains will merge into each other creating a grain boundary of the crystal structure at the intersection due to misalignment/orientation differences. Though most of the nanosheets are single layered, second and subsequent layers will nucleate on top of the first layer, typically at the initial nucleation site at the center of the triangle. Figure 2.1a shows an AFM topographic map of one of the samples showing a monolayer height between 0.7 and 1.0 nm. A bilayer domain in the middle with a step height of ~0.7 nm which is consistent with other studies. The bilayer has an expected lower step height than compared to the monolayer as seen in graphene and other 2DLMs. This is because the interlayer bonding is different than the interaction of the monolayer to the substrate, so an individual monolayer appears thicker per layer relative to multilayers.

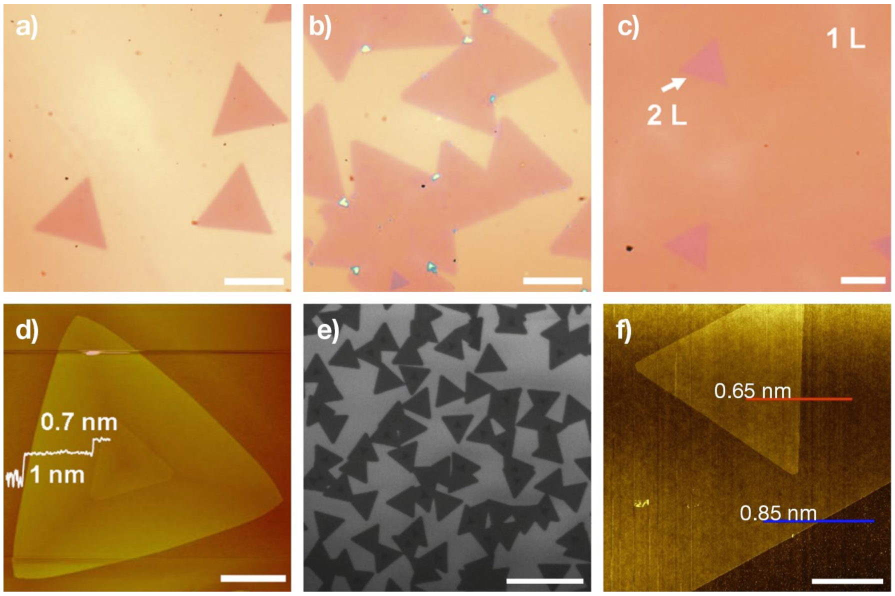

*Figure 2.1 – Chemical vapor deposition of TMDs MoSe$_2$ and WSe$_2$*
*a-c) OM image of WSe2 crystal grown by CVD. d) AFM topographic map of a monolayer WSe2 sample with a bilayer domain win the middle. Scale bars 5 µm (a-d, f) and 20 µm (e). Adapted (a-d)[13] and (e,f)[12]*

## 2.2 Spectroscopic analysis of CVD grown TMDs

Raman spectral mapping is used to analyze the layer thickness of 1–5 layers compared to a thicker bulk region (Figure 2.2a-d). The characteristic A$_{1g}$ of the out-of-plane mode located at 244 cm$^{-1}$ for bulk MoSe$_2$ shows a softening in the monolayer due to a smaller inter-planar restoring force. The A$_{1g}$ peak in the monolayer shifts down to 241 cm$^{-1}$, with a progressively stronger shift with decreasing the number of layers; a blueshift as the peak widens as the thickness gets smaller. For bilayers, the intensity is strongest which is greatly reduced with when adding layers. Additionally, Davydov splitting occurs for layers 3–5 MoSe$_2$ in Figure 2.2a, which is consistent with literature,[17] along with smaller beaks are also seen at in the range 239–241 cm$^{-1}$.

A more direct method of measuring the bandgap in TMDs is with photoluminescence (PL) spectroscopy, exposing the sample with high enough frequency photons will excite electrons across the gap, which will then emit light of the same energy as the gap when returning to their ground state. Direct bandgap systems will have a high PL emission, while for example the indirect bandgap of bulk $MoSe_2$ ($E_g = 1.1$ eV)[18,19] require phonon scattering, which greatly reduces the spectral peak. Previously, both theoretical and experimental research has shown that monolayer $MoSe_2$ (Figure 2.2a, blue line) exhibit a direct bandgap of 1.55 eV[17,19-21] which is confirmed in these results with a distinct peak at 800 nm, corresponding to 1.55 eV within error. As expected, the material transitions to an indirect bandgap of bilayer $MoSe_2$ (red line) shows a redshifted peak at 825 nm (1.50 eV) and a greatly reduced (by 35 times) peak intensity. Trilayer (green line) or any additional layers of $MoSe_2$ do not show an appreciable or detectable PL emission. The PL spectra is then mapped across the sample to determine the PL response within the layers. The direct to indirect transition is clearly shown in the map directly compared to the optical image of monolayer and bilayer regions, showing a dark triangle within the larger monolayer domain.

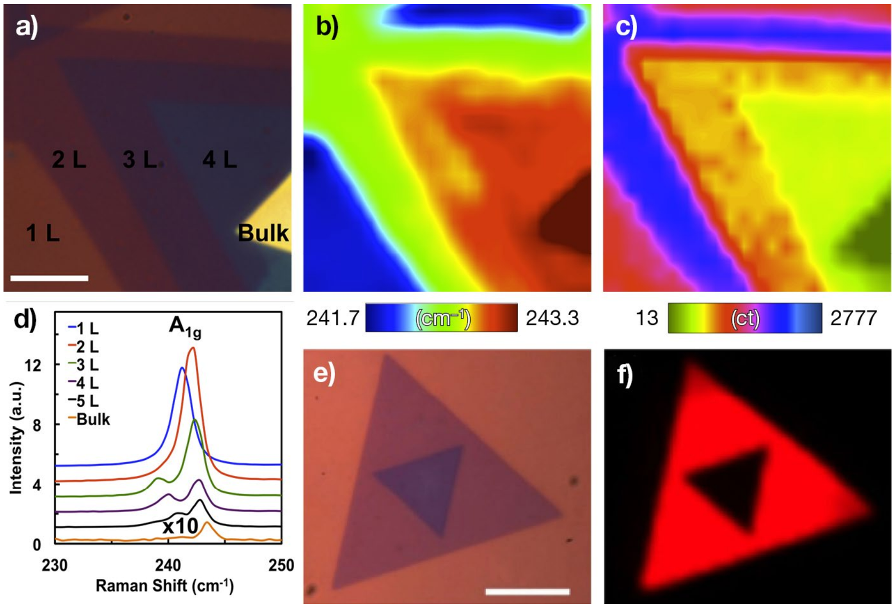

*Figure 2.2 – Raman and PL spectra of CVD grown* $MoSe_2$ *layers*

*a) OM image of the corresponding regions for Raman spectrum mapping. Raman maps of the* $A_{1g}$ *mode showing a thickness-dependent characteristic peak shift (b) and spectrum intensity (c). d)* $MoSe_2$ *nanosheet Raman spectra of 1–5 layer stacks compared to the bulk spectrum displayed at 10x scale. e) OM of MoSe2 mono/bilayer "triforce" nanosheet on SiO2/Si substrate and f) corresponding PL intensity map. Scale bars 6 μm (a) and 10 μm (e). Adapted*[12]

Spectral analysis of the CVD grown $WSe_2$ is carried out using micro Raman spectroscopy and photoluminescence spectroscopy. The monolayer regions show a single peak corresponding to the $A_{1g}$ resonance at 252 $cm^{-1}$ (Figure 2.3b, green line). The bilayer domains have an additional peak at 307 $cm^{-1}$ (red line), which corresponds to the $B_{2g}$ resonance mode, which generally should only appear in $N \geq 2$ layered regions, which suggests that additional interlayer interactions are present. The $A_{1g}$ peak is less sensitive to the layer number, with primarily a increase in intensity as N approaches 1. By mapping the peak intensity as shown in Figure 2.3c, a domain of $N \geq 2$ can be inferred from the dark region within the larger monolayer region with a bright intensity.

The Raman spectra show uniformity throughout the corresponding optical image with similar contrast of color indicating a good crystalline uniformity across the sample. The optical properties of the $WSe_2$ is analyzed using photoluminescence. Triangular single-domain samples of monolayer $WSe_2$ show a PL peak at 767 nm (Figure 2.3e), similar to data collected from mechanically exfoliated samples. PL measurements of the multi-domain monolayer regions of $WSe_2$ exhibit a strong peak intensity throughout, indicating high crystal quality of the monolayer sheets, but with a small shift to 766 nm (Figure 2.3e red curve). In the bilayer region, a much wider peak at ~790 nm and significantly reduced intensity (Figure 2.3e black curve). Further, by mapping the PL in two dimensions of 60 $\mu m^2$ region, the overall quality of the grown material is shown in Figure 2.3f with uniform emission throughout the monolayer regions demonstrating good uniformity of the sample with large regions of monolayer $WSe_2$. Some small regions with dark triangles indicated a secondary layer growth. Additionally, some slightly darker lines of lower intensity within the map suggest where the domain boundaries merge multiple crystals into one conformal monolayer.

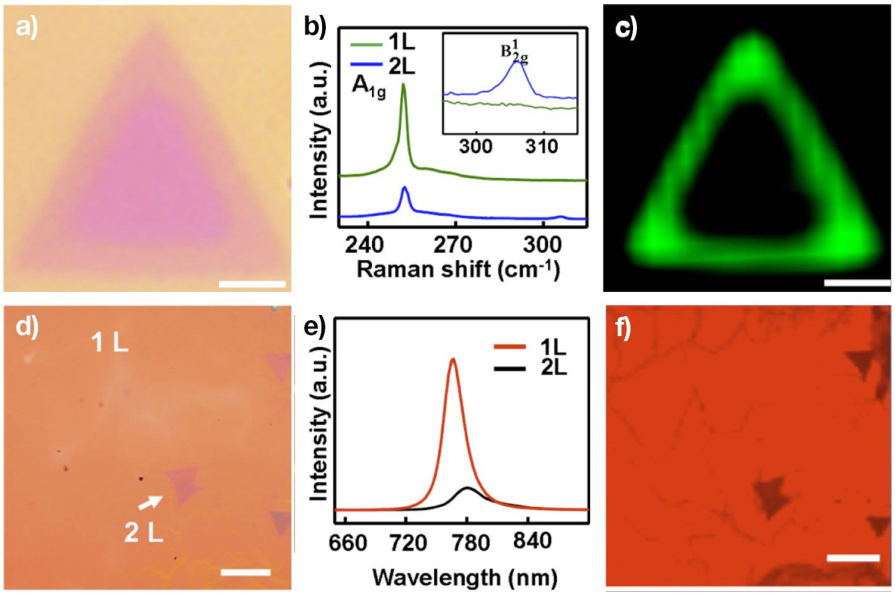

*Figure 2.3 – Raman and PL spectra of CVD grown $WSe_2$ layers*
*A typical $WSe_2$ crystal with a triangular bilayer domain within a monolayer (a) optical image and (c) Raman spectral map at ~1252 $cm^{-1}$ of the (b) $A_{1g}$ peak and (b inset) $B^1{}_{2g}$ peak. Large coverage of monolayer WSe2 with small domains of bilayers, optical image (d), representative PL spectra (e), and x-y PL map. Scale bars 5 µm (a,c) and 10 µm (d, f). Adapted*[13]

## Conclusions

Synthesis of 2DLMs is a critical towards both research scale investigations and any practical or commercial applications. A number of routes towards creating graphene and TMDs, among other 2DLMs successfully provide a range of options, each with advantages and disadvantages in terms of quality, scalability, and practicality. We demonstrated methods to synthesized layered materials with CVD used for further investigation by manipulation of these 2DLMs and implementation into electronic devices. Having various different approaches towards synthesis is important in satisfying the various needs of incorporating these new materials to viable applications.

## References

1. Lu, X., Yu, M., Huang, H. & Ruoff, R. S. "Tailoring graphite with the goal of achieving single sheets" *Nanotechnology* **10**, 269-272 (1999)

2. Li, X., Zhang, G., Bai, X., Sun, X., Wang, X., Wang, E. & Dai, H. "Highly conducting graphene sheets and Langmuir–Blodgett films" *Nature Nanotechnology* **3**, 538-542 (2008)

3. Narita, A. *et al.* "Synthesis of structurally well-defined and liquid-phase-processable graphene nanoribbons" *Nature Chemistry* **6**, 126 (2013)

4. de Heer, W. A., Berger, C., Wu, X., First, P. N., Conrad, E. H., Li, X., Li, T., Sprinkle, M., Hass, J., Sadowski, M. L., Potemski, M. & Martinez, G. "Epitaxial graphene" *Solid State Communications* **143**, 92-100 (2007)

5. Li, X., Cai, W., An, J., Kim, S., Nah, J., Yang, D., Piner, R., Velamakanni, A., Jung, I., Tutuc, E., Banerjee, S. K., Colombo, L. & Ruoff, R. S. "Large-Area Synthesis of High-Quality and Uniform Graphene Films on Copper Foils" *Science* **324**, 1312 (2009)

6. Banszerus, L., Schmitz, M., Engels, S., Dauber, J., Oellers, M., Haupt, F., Watanabe, K., Taniguchi, T., Beschoten, B. & Stampfer, C. "Ultrahigh-mobility graphene devices from chemical vapor deposition on reusable copper" *Science Advances* **1**, e1500222 (2015)

7. Chen, X., Zhang, L. & Chen, S. "Large area CVD growth of graphene" *Synthetic Metals* **210**, 95-108 (2015)

8. Lee, Y.-H., Zhang, X.-Q., Zhang, W., Chang, M.-T., Lin, C.-T., Chang, K.-D., Yu, Y.-C., Wang, J. T.-W., Chang, C.-S., Li, L.-J. & Lin, T.-W. "Synthesis of Large-Area $MoS_2$ Atomic Layers with Chemical Vapor Deposition" *Advanced Materials* **24**, 2320-2325 (2012)

9. Zhou, H., Yu, W. J., Liu, L., Cheng, R., Chen, Y., Huang, X., Liu, Y., Wang, Y., Huang, Y. & Duan, X. "Chemical vapour deposition growth of large single crystals of monolayer and bilayer graphene" *Nature Communications* **4**, 2096 (2013)

10. Liu, L., Zhou, H., Cheng, R., Yu, W. J., Liu, Y., Chen, Y., Shaw, J., Zhong, X., Huang, Y. & Duan, X. "High-Yield Chemical Vapor Deposition Growth of High-Quality Large-Area AB-Stacked Bilayer Graphene" *ACS Nano* **6**, 8241-8249 (2012)

11. Suk, J. W., Kitt, A., Magnuson, C. W., Hao, Y., Ahmed, S., An, J., Swan, A. K., Goldberg, B. B. & Ruoff, R. S. "Transfer of CVD-Grown Monolayer Graphene onto Arbitrary Substrates" *ACS Nano* **5**, 6916-6924 (2011)

12. Shaw, J. C., Zhou, H., Chen, Y., Weiss, N. O., Liu, Y., Huang, Y. & Duan, X. "Chemical vapor deposition growth of monolayer $MoSe_2$ nanosheets" *Nano Research* **7**, 511-517 (2014)

13. Zhou, H., Wang, C., Shaw, J. C., Cheng, R., Chen, Y., Huang, X., Liu, Y., Weiss, N. O., Lin, Z., Huang, Y. & Duan, X. "Large Area Growth and Electrical Properties of p-Type $WSe_2$ Atomic Layers" *Nano Letters* **15**, 709-713 (2015)

14. Zhang, Y., Zhang, Y., Ji, Q., Ju, J., Yuan, H., Shi, J., Gao, T., Ma, D., Liu, M., Chen, Y., Song, X., Hwang, H. Y., Cui, Y. & Liu, Z. "Controlled Growth of High-Quality Monolayer WS2 Layers on Sapphire and Imaging Its Grain Boundary" *ACS Nano* **7**, 8963-8971 (2013)

15. Huang, J.-K., Pu, J., Hsu, C.-L., Chiu, M.-H., Juang, Z.-Y., Chang, Y.-H., Chang, W.-H., Iwasa, Y., Takenobu, T. & Li, L.-J. "Large-Area Synthesis of Highly Crystalline WSe2 Monolayers and Device Applications" *ACS Nano* **8**, 923-930 (2014)

16. Li, X. L. & Li, Y. D. "Formation of $MoS_2$ Inorganic Fullerenes (IFs) by the Reaction of $MoO_3$ Nanobelts and S" *Chemistry – A European Journal* **9**, 2726-2731 (2003)

17. Tonndorf, P., Schmidt, R., Böttger, P., Zhang, X., Börner, J., Liebig, A., Albrecht, M., Kloc, C., Gordan, O., Zahn, D. R. T., Michaelis de Vasconcellos, S. & Bratschitsch, R. "Photoluminescence emission and Raman response of monolayer $MoS_2$, $MoSe_2$, and $WSe_2$" *Opt. Express* **21**, 4908-4916 (2013)

18. Coehoorn, R., Haas, C., Dijkstra, J., Flipse, C. J. F., de Groot, R. A. & Wold, A. "Electronic structure of $MoSe_2$, $MoS_2$, and $WSe_2$. I. Band-structure calculations and photoelectron spectroscopy" *Physical Review B* **35**, 6195-6202 (1987)

19. Liu, L., Kumar, S. B., Ouyang, Y. & Guo, J. "Performance Limits of Monolayer Transition Metal Dichalcogenide Transistors" *IEEE Transactions on Electron Devices* **58**, 3042-3047 (2011)

20. Tongay, S., Zhou, J., Ataca, C., Lo, K., Matthews, T. S., Li, J., Grossman, J. C. & Wu, J. "Thermally Driven Crossover from Indirect toward Direct Bandgap in 2D Semiconductors: $MoSe_2$ versus $MoS_2$" *Nano Letters* **12**, 5576-5580 (2012)

21. Horzum, S., Sahin, H., Cahangirov, S., Cudazzo, P., Rubio, A., Serin, T. & Peeters, F. M. "Phonon softening and direct to indirect band gap crossover in strained single-layer $MoSe_2$" *Physical Review B* **87**, 125415 (2013)

# Chapter 3: Stretching Membranes Across Microstructured Arrays

One method of straining a two-dimensional material is to place it on a substrate with surface irregularities, as the membrane will not be uniformly supported by the physical structures underneath. By controlling the topographic structure, the morphology of the membrane can also be controlled. Transferring these membranes onto the patterned substrate, the structure will be forced into two dominant modes, either strongly conforming to the substrate by stretching into the valleys, or staying suspended across the gaps. The combination of stiffness, structure, and aspect ratio is critical in determining how the membrane will behave, and additionally the layer can rip and break apart if the strain becomes too large. Also, the adhesion of the membrane to the surface can allow for slipping, which would relieve some of the strain, for instance in a one dimensional pattern, the layer can conform without stretching, whereas if the layer is pinned to the peaks within the substrate, or in a two dimensional array, it will be forced to stretch into the valleys. Various factors influence the adhesion of the membrane beyond the structure, such as the van der Waals forces, liquid surface tension and capillary action that pulls the membrane into conformity. Further methods of controllably forcing the membrane into the gaps is also possible, such as pressing with an elastic stamp, i.e. PDMS, or with pressure differentials across the impermeable 2DLM nanosheet.

Other groups' concurrent research with this project had similar approaches of transferring graphene onto topographically patterned substrates, with varying success.[1,2] Since then, many more reports have emerged with continuing advancements in the field,[3] which is further discussed at the end of the chapter, including a variety of 2DLMs in applications such as optoelectronics,[4] field emission of electrons and quantum photon emitters, as well as device characterization and theoretical modeling.[5] Before delving into transferring graphene on top of a topographically prepatterned substrate, the technique of underetching the substrate beneath a clamped graphene sample is explored in order to attempt to strain the graphene strip within a device structure.

## 3.1 Suspending graphene nanomembranes

Before graphene was discovered in 2004, it was not known if it would be stable as a two-dimensional crystal in isolation but supported on a substrate, let alone suspended with no physical support. Though the membrane structure is atomically thin, it is incredibly strong and is in fact capable of freestanding across a gap, as first demonstrated in 2007.[6] The preparation of creating suspended graphene is by depositing chrome and gold in specified regions using lithography. An etching agent is then used to selectively remove the underlying $SiO_2$ substrate where the gold does not protect it, causing the graphene to be released from its supporting structure, but still be clamped by the region where the gold is still holding it. The overhanging graphene is now suspended across the gap, only supported by the connected regions clamped on either side. The single atom membrane is then free to deform out of the plane, which is both simulated and observed through TEM diffraction patterns to have various nanoscale rippled structures.[6]

Later studies found that larger scale, wavelike ripples would form across the suspended region through spontaneous and temperature induced strains.[7] The ripple orientation, wavelength, and amplitude are tunable by utilizing the unusual negative thermal expansion of graphene [8] in conjunction with the specific boundary conditions of the suspended region. Suspended graphene has even been used as a support material for other samples for advanced TEM, as the atomically thin membranes are highly transparent to the electron beam while being able to support light atoms and molecules on its surface.[9] Other studies utilizing suspended graphene over sealed chambers utilize the impermeability of the nanomembrane to create pressure differentials to create a balloon-like effect to induce strain. [10-12] Studies of straining suspended graphene have used an *in situ* nanoindenter to measure the impact on the electronic properties.[13] The Raman shift due to strain is measured in few-layer graphene indented with an AFM tip.[14]

Here, suspended graphene devices are made in an attempt to deform the graphene out of the plane to induce strain and ultimately perceive a change in the electronic performance. Figure 3.1 shows proposed methods of straining within the device design, including (a) indenting with the probing tip of an AFM *in situ*, (b) incorporating a piezoelectric element to pull one side of the suspended graphene, and (c and d) using an electrostatic force from the back gate to pull the sample towards the substrate. These designs allow for controlled strain within the suspended channel while measuring the resistance across, though there are many difficulties in both fabricating such devices and properly characterizing the device performance. Since the device channel itself is moving in order to provide strain, it is difficult to properly apply a gate field to measure transport properties.

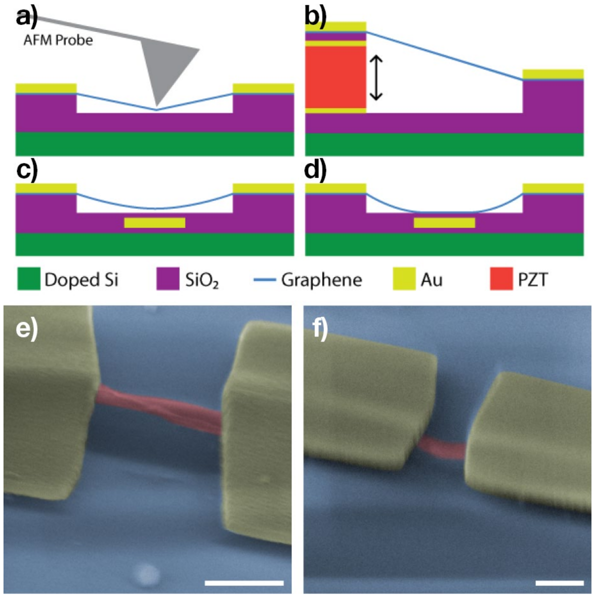

*Figure 3.1 – Methods of straining suspended graphene membranes*
*Schematic of proposed methods to controllably strain graphene with by (a) Indenting suspended graphene with an AFM probe tip (b) using a piezoelectric material such as lead zirconate titanate (PZT, red) to deform one side of the sample (c,d) using a back-gate the electrostatically attract the graphene towards the substrate. Suspended graphene devices: e) and f) SEM images of two suspended graphene devices (false colored: graphene is red, gold is yellow, and substrate is blue). Scale bars 500 nm (e,f).*

Mechanically exfoliated graphene flakes on 300 nm $SiO_2$ coated, doped Si wafers were optically selected according to shape that were thin and rectangular. Electron beam lithography (EBL) is used to place electrodes on both ends of the graphene channel. Channel lengths of 100–200 nm were used. After the Cr/Au electrodes are places, the sample is put in an aqueous 10:1 buffered oxide etch (BOE) for a few minutes. The etching solution slightly undercuts the metal electrodes at the same rate as the downward etching, while the capillary forces under the graphene allow for the etchant to penetrate faster and fully etching beneath the graphene faster. Special care is then taken to dry the sample, as the surface when drying would tear the suspended graphene apart. Therefore, IPA is used at close to its boiling point as to minimize this effect, as the surface tension is greatly reduced. Figure 3.1e and f show tilted SEM images of the suspended graphene.

### 3.2 Self-assembly and etching of polystyrene spheres and nanopillar arrays

Colloidal particles, and in particular here polystyrene spheres, with diameters on the order of micrometers have previously been used to create close-packed 3D arrays and hexagonally arranged monolayer in ordered domains and grains.[15,16] This is a useful tool in bottom up fabrication, where chemical and physical dynamics of a system arrange in an advantageous structure for engineering, such as photonic bandgap crystals of dielectric spheres. A number of processes have been used to crystalize colloidal solutions, including spin coating and convectively self-assembled lattices. When under the right conditions, the array thickness can be tuned consistently, and dense monolayers are achievable. In addition to optical and photonic crystal applications, these polystyrene arrays have been utilized as sacrificial templates to create periodic microstructures of other materials. For example, by filling in the empty space between the spheres, and then chemically removing the spheres, a negative space is created of hollow, spherical pores. Additionally, with monolayered spherical arrays, the particles can act as masking material when etching the underlying layers. Etching of the spheres themselves will also shrink them in place, which forms a separation between each sphere of smaller diameter (Figure 3.2a).

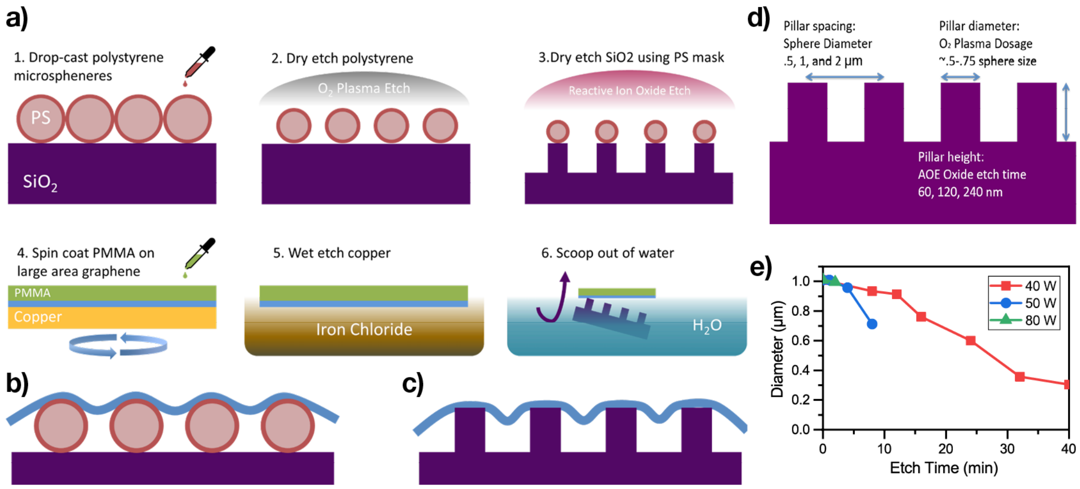

*Figure 3.2 – Nanopillar fabrication, etching and transfer processes*

*a) Schematic diagram of the patterned substrate fabrication and graphene transfer process by 1) dropcast of PS spheres, 2) dry etching the spheres using $O_2$ plasma, 3) dry etching $SiO_2$ using reactive ion etch (optional), 4) spin coating PMMA onto CVD graphene coated copper foil, 5) etch away the copper floating on an iron chloride solution, 6) clean in water and scoop out the floating graphene/PMMA with the substrate, and finally dissolving away the PMMA with acetone and IPA to end with either b) graphene suspended on either PS spheres or c) $SiO_2$ nanopillars. d) The aspect ratio of the pillar dimensions is defined with the height h which is controlled by the length of the oxide etch, the diameter $d_e$ is determined by the remaining etched PS sphere size, and the pillar spacing is set at the initial, unetched PS sphere diameter $d_0$ and a space between nearest neighbor pillar $d_s = d_0 - d_e$. e) Sphere diameter as a function of etching time for 1 µm PS in 40, 50, and 80 W power $O_2$ plasma.*

The polystyrene spheres of 0.5, 1, and 2 µm diameter are diluted to proper concentration (~1 wt%) in both pure water and 50% ethanol solution, and then dropcast onto a $SiO_2$/Si substrate (300 nm $SiO_2$ thickness on highly doped silicon). With each pipet drop, a larger white liquid forms on the surface. As the water evaporates, the crystalline PS spheres coalesce into ordered crystal domains. Thick white regions form a ring around the edge of the sample with much thinner and empty regions throughout the middle of the sample as the water dries towards the surface perimeter. In particular, hexagonally close packed PS spheres form throughout the empty center region within the thick ring. SEM images of the edge of a monolayer of spheres is shown in Figure 3.3a.

Etching the PS spheres using oxygen plasma will remove material from the spheres to create non-close-packed crystals with uniform spacing. [17] As each sphere loses material remaining in place on the surface, the shrunken spheroids now have a physical gap between each one with uniform dimensions. The oxygen plasma dosage is used to tune how much polystyrene remains and the uniformity of the remaining spheroid. Figure 3.2 shows the etching rates of 1 μm spheres are etched at 40, 50, and 80 W plasma power in order to reduce the size and increase the empty space between each sphere, which are shown in SEM images of increasing etch time of 32–72 min in Figure 3.3b-d. Higher etch rates create irregular structures, as seen in the chaotic structures on the surface of the spheres in Figure 3.3d, so a balance between etch time and power is recommended

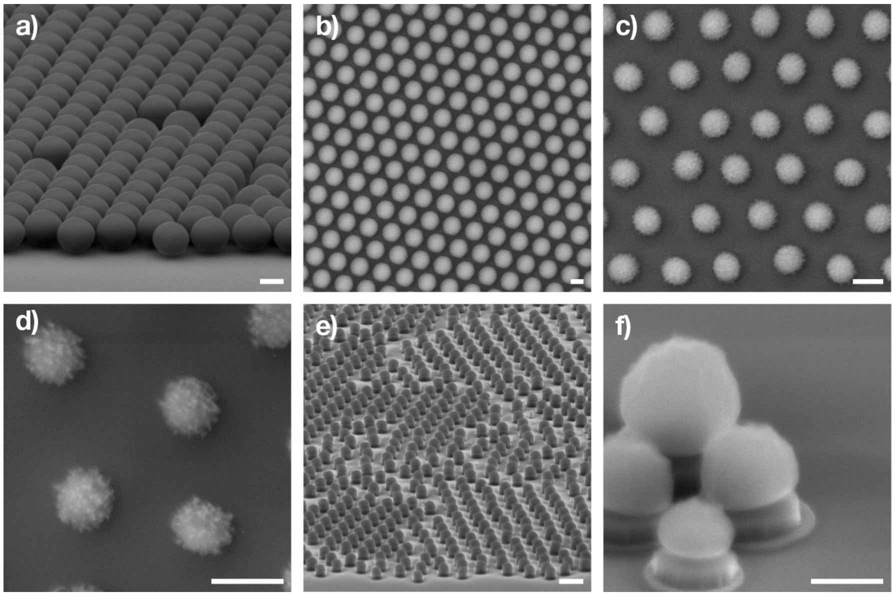

*Figure 3.3 – SEM images of polystyrene spheres and $SiO_2$ nanopillars*
*a) Tilted SEM image of the edge of a close packed monolayer of PS spheres. Oxygen plasma etched 2 µm PS spheres after b) 32 min, c) 48 min and d) 72 min. $SiO_2$ nanopillars after reactive ion etching with the PS sphere mask on top (e,f). Scale bars 1 µm (a-f).*

The spheres are subsequently used as etching masks to produce uniform nanopillars. As the original sphere diameter determines the periodicity of the spacing between pillar centers (only 0.5, 1, or 2 µm), the etching of the PS spheres determines the pillar diameter and subsequently the gap between each pillar. A dry plasma enhanced reactive ion etching process is used in an STS Advanced Oxide Etcher (AOE) in order provide an isotropic, directional etch of the underlying $SiO_2$ layer of the substrate pillars with high aspect ratio. Figure 3.3a and b show tilted SEM images of the nanopillar arrays with the PS sphere mask sitting on top. At an etching rate up to ~2 nm/min, the pillar height is controllable, all the way to complete removal of the 300 nm $SiO_2$ film, though the bare doped-silicon wafer surface is conductive and make contact with graphene, so typically at least a small amount of oxide is left. Taller pillars are of course achievable with a thicker initial oxide layer. However, the plasma etching process is not completely selective to the oxide, so the PS is also removed, but at a slower rate; in particular for the .5 μm spheres and tall pillar etching, the PS will be completely removed before the etching is completed, and the spheres will show a rounded top or even a sharp tip. The polystyrene is then removed with further oxygen plasma if the oxide etch did not already remove them, which happens more often to the smaller spheres. The pillars form in the hexagonal packed structures that the PS sphere mask determines in a cylindrical structure with diameter corresponding to the sphere size. Pillar heights of 60, 120, and 240 nm with each of the PS sphere sizes (which defines the pillar spacing), are studied here to give a range of aspect ratios.

## 3.3 Graphene transfer onto spheres and nanopillars

Graphene is then transferred onto either the polystyrene spheres (Figure 3.2b and Figure 3.4) or the etched nanopillars and (Figure 3.2c and Figure 3.5). CVD graphene is transferred using the previously discussed wet transfer process using a PMMA support layer to float on the surface of water after etching away the copper using iron oxide. This delicate step is critical in the uniformity that the membrane will form on top of the microstructures. Additionally, during removal of the PMMA using acetone and IPA, capillary forces will strain the membrane and can cause it to compress the spheres, or to rip apart the graphene layer in order to reduce the strain. This will also cause the layers to adhere to the valleys between the protruding structures. The surface tension can be reduced, as seen in suspended graphene fabrication, by using heated isopropyl alcohol at the last step, which reduced the force the meniscus has when drying.

OM images of the graphene on top of PS spheres is shown in the of Figure 3.4a, which adds a green tint to the spheres color which are otherwise brown. The AFM images in Figure 3.4c shows the topology of the various regions with and without the PS and the graphene, as it transitions from patterned to flat. Additionally, the AFM in of Figure 3.4d shows that the graphene remains fairly flat, suspended across the spheres rather than getting pulled between the cervices between them and the graphene ends up tearing apart into smaller, disconnected regions. The graphene can also closely wrap itself around individual spheres, making interesting folding patterns as seen in SEM images. In certain instances, the transfer process of the graphene flattens the PS spheres underneath, as seen in the SEM image of Figure 3.4e. This could be due to the surface tension of the IPA and enhanced by reactions with the acetone during the wet transfer and drying process.

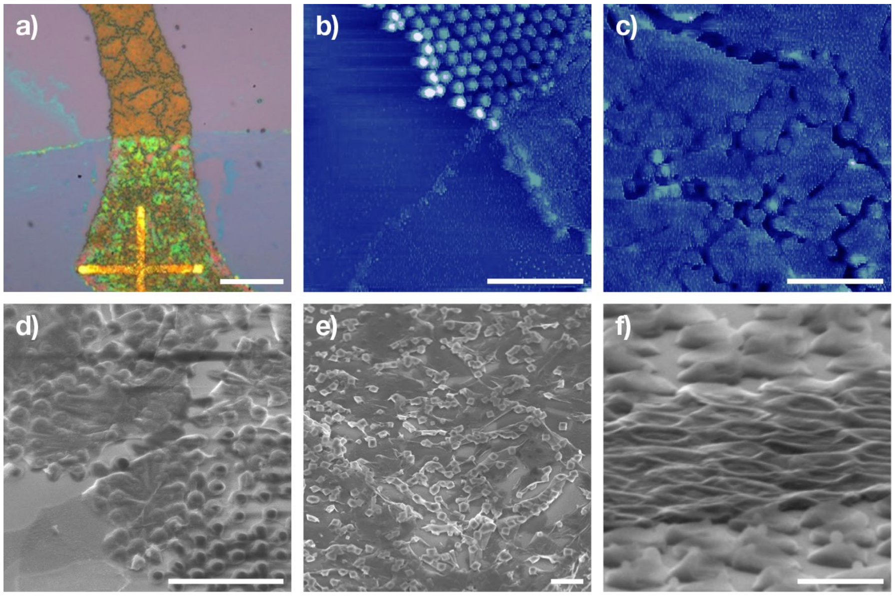

*Figure 3.4 – Polystyrene monolayers with graphene transferred on top*
*Graphene on PS spheres: a) OM image, and b) AFM plot of the intersection of regions of PS spheres and graphene coverage. c) AFM pot of graphene on top of PS spheres with ripped regions. d) and e) Tilted SEM images of the ripped regions of graphene on PS spheres, f) Tilted SEM image of flattened spheres. Scale bars 25 µm (a), 5 µm (b-f). AFM height scale is 800 nm (b,c).*

The increased robustness of the etched $SiO_2$ nanopillars over the PS spheres makes them more structurally reliable and more practical. Figure 3.5 shows many SEM images of graphene transferred on top of nanopillars of varying dimensions. Figure 3.5a-c shows tilted angle SEM images of the various aspect ratios and the morphology the graphene takes. With short pillars, the graphene is mostly adhered to the underlying substrate between the pillars, with interconnected creases between each nearest neighbor pillar forming a six-fold symmetrical hexagonal, star like structure. Where these creases meet the pillars is a region where the graphene separates from the substrate and the pillar as it needs to fold up to form the crease. The size and shape of the delaminated regions is highly dependent on the aspect ratio of the pillars. This trend continues as the relative pillar height increases, though a larger delamination region is observed, as there is a higher pillar for the graphene to conform to.

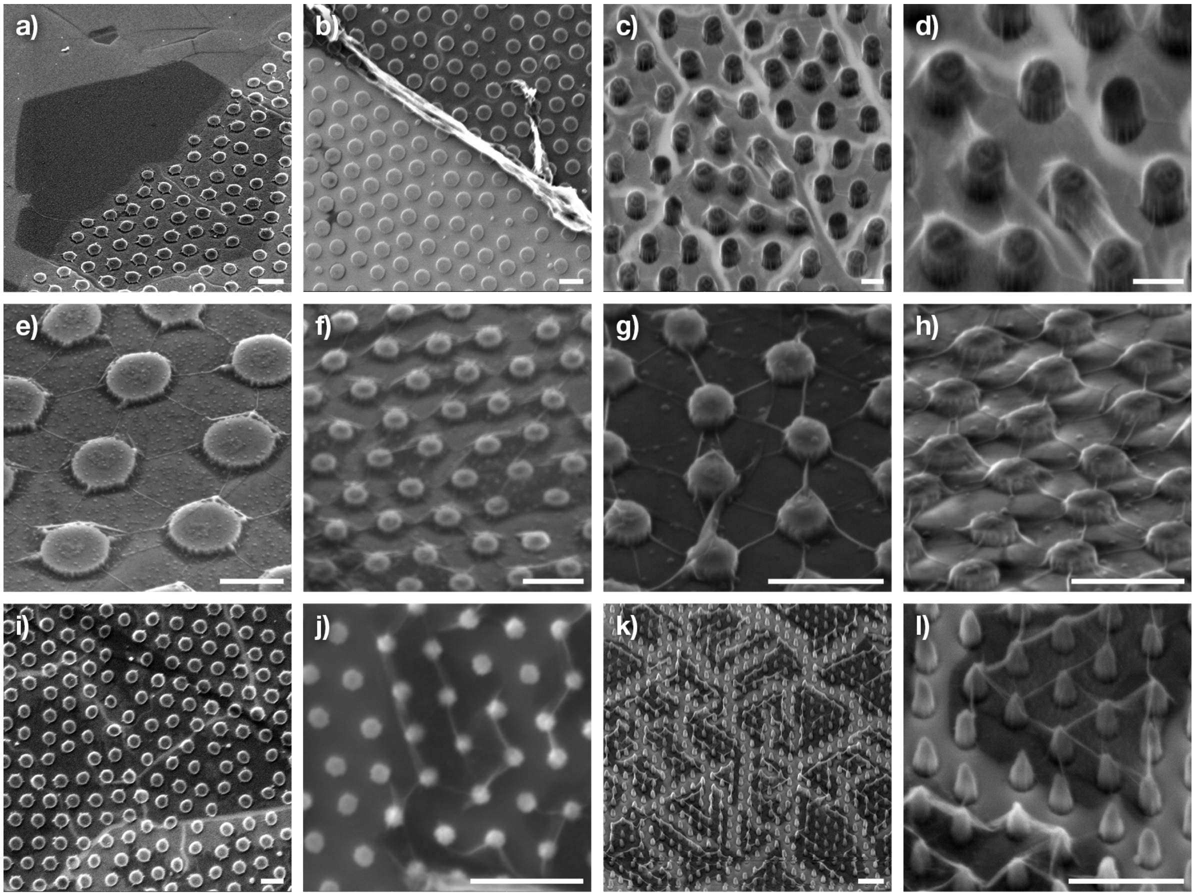

*Figure 3.5 – SEM of graphene transferred onto $SiO_2$ nanopillar arrays*
*Tilted (a, c-h, k and l) and non-tilted (b, i, and j) SEM images of graphene on $SiO_2$ nanopillar arrays. a) Bilayer graphene domain within a monolayer sheet both on and off of the pillars. b) Crumpled up edge of graphene on nanopillars. Scale bars 1 µm (a-d,i-l), and 500 nm (e-h).*

Raman spectroscopy is used to analyze the effects that the underlying patterned substrate has on and subsequent morphological changes and strain that is applied to the graphene samples. The un-normalized spectra show a decrease in change in peak intensity of the strained sample, as the morphological changes alters the ability to focus properly and scatters the incident beam with additional background noise. The control graphene peaks of flat, unstrained graphene is a *G* peak of 1602 $cm^{-1}$ and *2D* peak of 2698 $cm^{-1}$. Spectral analysis examines the effects of the PS sphere diameter and the (240 nm height) nanopillar spacing (defined by the PS spheres used as the mask), shown in Figure 3.6, compared with the graphene control (black). Figure 3.7 shows the Raman peak shift for the nanopillar with heights of 60 nm 120 nm and 240 nm and spacing of the 0.5 µm, 1 µm, and 2 µm. The spectra are separately normalized to each peak *G* and *2D* as the background noise from the irregular surface disrupts the smooth and consistent measurements. Figure 3.8 graphs the strain induced peak position vs. the spacing and height of the spheres and nanopillars. The graphene on PS spheres shows a steadily increasing redshift as the sphere diameter decreases, with the largest change in the 0.5 µm spheres with *G* and *2D* peaks at 1586 and 2674 $\text{cm}^{-1}$ respectively. However, with the nanopillars, the pattern is not as clear in relating the amount of strain present with the spacing of the pillars. With a maximum redshift of 18 and 24 $\text{cm}^{-1}$ for the *G* and *2D* respectively, the estimated strain within the stretched graphene is < 1%, though again, this may underestimate the total strain, as it averages around the entire area of nonuniform strain, as these value are not consistent with the physical form observed using microscopy.

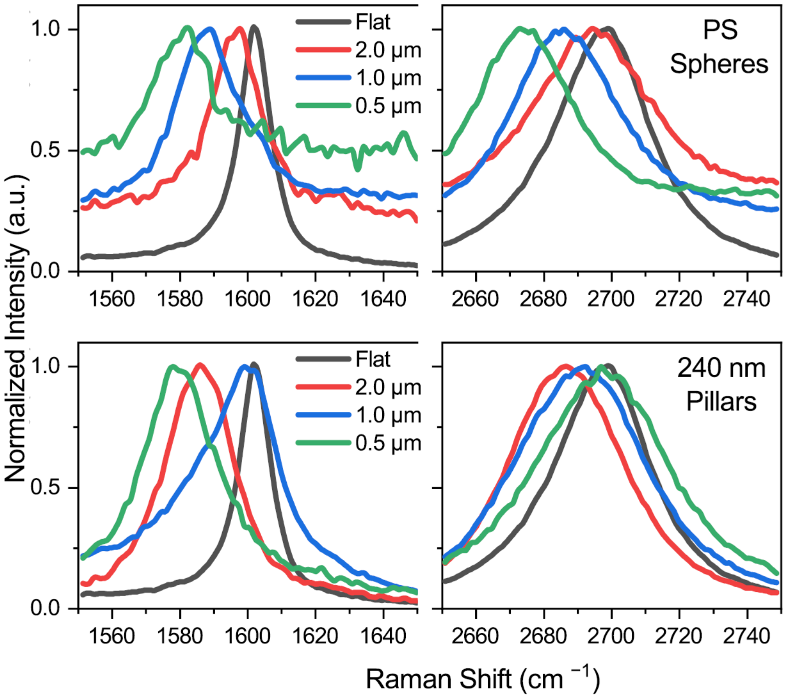

*Figure 3.6 – Raman peak shift of graphene on PS spheres and SiO$_2$ pillars vs. spacing Changes of the Raman shift G peaks (left) and 2D peaks (right) of graphene transferred onto PS spheres (top) and 240 nm height SiO$_2$ nanopillars (bottom) with spacing and sphere sizes of 2 µm (red) 1 µm (blue and 0.5 µm (green) with a control flat graphene (black).*

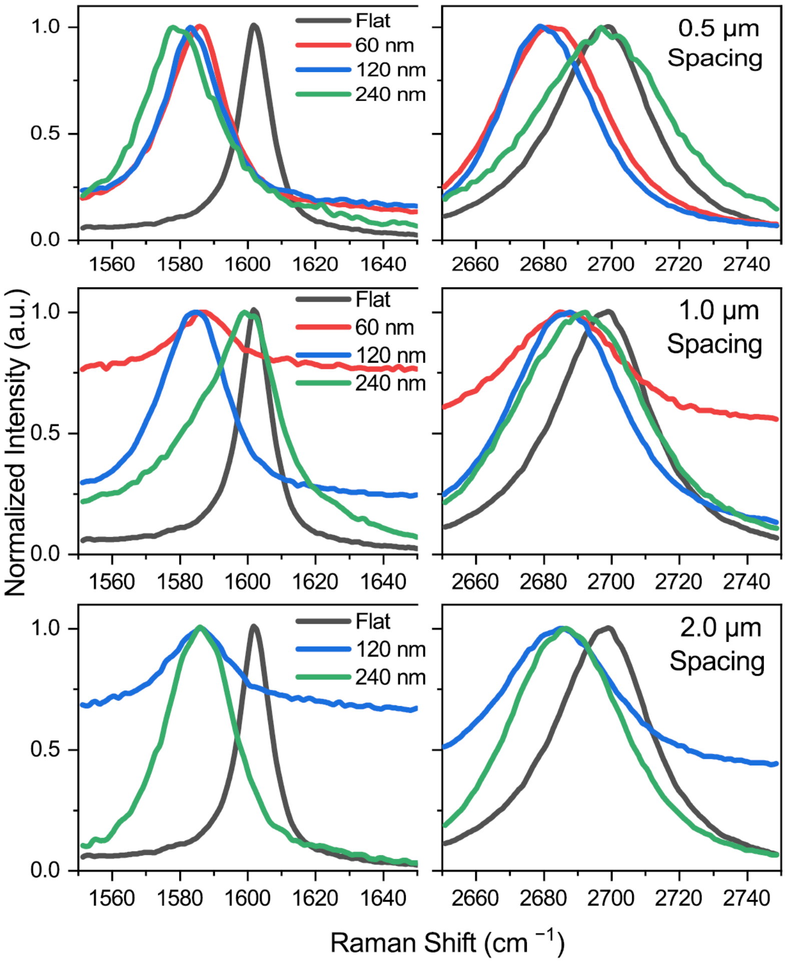

*Figure 3.7 – Raman peak shifts of graphene SiO$_2$ pillars vs. height and spacing*

*Redshift of the Raman G peaks (left) and 2D peaks (right) of graphene transferred onto SiO$_2$ nanopillars with spacing of 0.5 µm (top), 1 µm (middle), and 2 µm (top) and height of 60 nm (red) 120 nm (blue) and 240 nm (green) with a control flat graphene (black).*

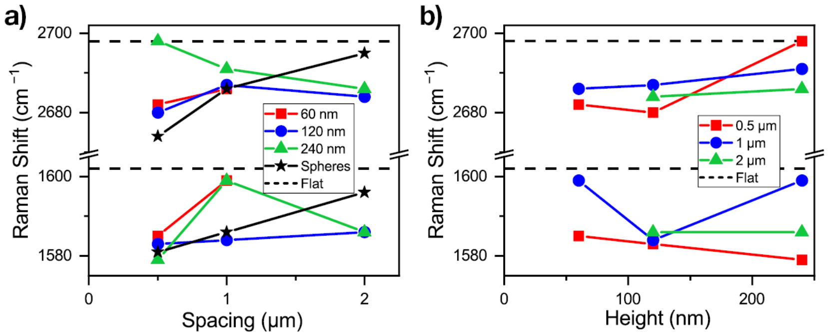

*Figure 3.8 – Raman shift on pillars and spheres vs. spacing and height*
*The strain induced Raman shift of graphene stretched on polystyrene spheres and* $SiO_2$ *nanopillars vs the spacing (a) and the height (b).*

Other research conducted concurrently and subsequently using similar approaches to transferring graphene onto nanopillars reached similar results to this study.[18] Since these investigations, progress has been made in using strain on topographically patterned substrates, using varying methods and revealing additional insights. They incorporate various alterations to the basic concept by utilizing both different patterns, shapes, and aspect ratios, combined with other types of 2DLMs, such as TMDs. They also incorporate further characterization such as using probe microscopy and tunneling spectroscopy.

Another way to vary the strain profile beyond adjusting the nanopillar spacing and aspect ratio is to change the shape of the pillar, into domes, pyramids, inverted pyramids, or any other protruding structure which will change the way the graphene membrane needs to wrap around and conform to. Using feature sizes from 2.5 µm to 50 µm patterned into 3D microstructures on PDMS substrates, subsequent studies to strain graphene demonstrate the versatility of these methods.[19] In another study using $SiO_2$ pyramids and opal sphere arrays, CVD graphene is either suspended across or conforms to the surface topography respectively.[20] Electronic transport measurements demonstrate that while the *I–V* shows a linear curve indicating no apparent bandgap, these morphological changes will, while reducing the contact resistance, will more significantly reduce the sheet resistance up to 3 times that of unstrained graphene. Other methods including transferring on top of monodispersed nanoparticles arrays. [21] This enables much smaller topographic dimensions, as the particles can be smaller than 10 nm, but the periodicity is hard to control for an ordered array. Additionally, the micro-Raman spectroscopy has a far to limiting resolution to measure such small scales. Similarly, nanopillars can be fabricated at much smaller scales (down to 40 nm spacing and 80 nm height nanopillars) using self-assembled block copolymer resists to etch $SiO_2$ substrate, which creates a more ordered array than the nanoparticles, with both positive and negative form factor nanopillars.[22]

Further improvements were made by utilizing STM and STS along with SEM and AFM, the spectral modification of graphene due to strain and the pseudo landau levels were visualized in graphene on nanopillars.[23] On both lift-off resist and gold nanopillars of 1–2 µm separation and 50–600 nm height show a similar method of straining by either suspending across the pillars, or conforming to the substrate with a network of wrinkles connecting the nanopillars. An additional innovation here is the use of BN to create Moiré patterns which enhance the ability to collect spectra.

Electronic transport measurements of graphene on the $SiO_2$ pyramids demonstrate that, while the *I*–*V* shows a linear curve indicating no apparent bandgap, these morphological changes will, while reducing the contact resistance, will more significantly reduce the sheet resistance up to 3 times that of unstrained graphene.[20] Another study indicates that the transport mechanisms in graphene on nanopillars is due to the chemical interaction with the substrate rather than the induced strain.[24] In other magneto-transport measurements, a locally varying potential is inferred which is likely due to a variable gate capacitance throughout the graphene adhered to the surface features and forming quasibound states within the nanosheet.[25]

Additionally, these techniques have been extended to other 2DLMs, such as TMDs, which elicit a number of intriguing opportunities due to their intrinsic semiconductor nature. Another example uses $WSe_2$ on an array of nanopillars with 0.3 aspect ratio, consistent quantum emission is achievable and localized at the pillar tip.[26] At low enough temperatures, the excitons within the direct bandgap monolayer TMD are funneled towards the strained region at the tip of the nanopillar, causing enhance emission when exposed to an excitation laser, as measured by PL spectroscopy. A blue shifting of the bandgap in $MoS_2$ bilayers due to strain on cone and pyramid patterned substrates is shown to enhance photodetection within an increased photocurrent in the higher strained regions.[27] Another study shows the highly efficient field electron emission of $MoSe_2$ and $MoS_2$ suspended on an array of ZnO pillars.[28] Further experiments demonstrate a fabricated resonator of $MoS_2$ suspended on SiO2 pillars. Additionally, by separating contributions of both the Raman and PL spectroscopy data, the corresponding strain is more precisely estimated.[29]

## Conclusion

Graphene and other 2DLMs are incredibly robust within each layer and is stable in freestanding suspension, and can be stretched across various out of plane structures. Transferring 2DLMs onto patterned substrates offers a useful way to control the local strain within the membrane as is stretches across the substrate with various morphologies based on the dimensions and topographical shape of the pattern. SEM images reveal the conforming membrane of graphene on top of the polystyrene spheres and SiO2 nanopillars, incorporating strain within the naturally two-dimensional membrane, and by controlling the pattern sizes, the strain will change. Not only does the aspect ratio affect the way the membrane adheres to the surface, as the dimensions shrink, the stiffness of the nanosheet would become more significant. It is critical to further understand the tendencies of the nanomembrane to stay suspended across the pillars or to fall into and adhere to the underlying substrate. A crucial next step is to incorporate the strained graphene into a device with a transport gap, which is difficult, as the strain profile through the membrane is irregular, meaning the current could travel around and between the gapped regions. One method to ensure charge transport through the strained region is to place a flat electrode on top, which would make contact at the top of the pillar.

This technique can also be combined with straining methods, such as pressure differentials or elastic substrates, to further control the structure and strain within these nanosheets. Of course, a range of structures and other patterns can also be explored beyond a hexagonal array of spheres or cylindrical pillars, such as inverted pillars, square/rectangular arrays, honeycomb and wave patterns and more complex structures such as herringbone and checkerboard morphologies. The approach itself is versatile, and as shown, can also be applied to any number of other 2DLMs or membrane-like nanosheets. Many subsequent studies have explored the interesting behaviors that emerge as these materials stretch and strain across patterned substrates, which make for unique opportunities to harness the resulting electronic properties.

## References

1. Tomori, H., Kanda, A., Goto, H., Ootuka, Y., Tsukagoshi, K., Moriyama, S., Watanabe, E. & Tsuya, D. "Introducing Nonuniform Strain to Graphene Using Dielectric Nanopillars" *Applied Physics Express* **4**, 075102 (2011)

2. Reserbat-Plantey, A., Kalita, D., Han, Z., Ferlazzo, L., Autier-Laurent, S., Komatsu, K., Li, C., Weil, R., Ralko, A., Marty, L., Guéron, S., Bendiab, N., Bouchiat, H. & Bouchiat, V. "Strain Superlattices and Macroscale Suspension of Graphene Induced by Corrugated Substrates" *Nano Letters* **14**, 5044-5051 (2014)

3. Dai, Z., Liu, L. & Zhang, Z. "Strain Engineering of 2D Materials: Issues and Opportunities at the Interface" *Advanced Materials* **31**, 1805417 (2019)

4. Li, H., Contryman, A. W., Qian, X., Ardakani, S. M., Gong, Y., Wang, X., Weisse, J. M., Lee, C. H., Zhao, J., Ajayan, P. M., Li, J., Manoharan, H. C. & Zheng, X. "Optoelectronic crystal of artificial atoms in strain-textured molybdenum disulphide" *Nature Communications* **6**, 7381 (2015)

5. Milovanović, S. P., Covaci, L. & Peeters, F. M. "Strain fields in graphene induced by nanopillar mesh" *Journal of Applied Physics* **125**, 082534 (2019)

6. Meyer, J. C., Geim, A. K., Katsnelson, M. I., Novoselov, K. S., Booth, T. J. & Roth, S. "The structure of suspended graphene sheets" *Nature* **446**, 60 (2007)

7. Bao, W., Miao, F., Chen, Z., Zhang, H., Jang, W., Dames, C. & Lau, C. N. "Controlled ripple texturing of suspended graphene and ultrathin graphite membranes" *Nature Nanotechnology* **4**, 562 (2009)

8. Steward, E. G., Cook, B. P. & Kellett, E. A. "Dependence on Temperature of the Interlayer Spacing in Carbons of Different Graphitic Perfection" *Nature* **187**, 1015-1016 (1960)

9. Meyer, J. C., Girit, C. O., Crommie, M. F. & Zettl, A. "Imaging and dynamics of light atoms and molecules on graphene" *Nature* **454**, 319 (2008)

10. Bunch, J. S., Verbridge, S. S., Alden, J. S., van der Zande, A. M., Parpia, J. M., Craighead, H. G. & McEuen, P. L. "Impermeable Atomic Membranes from Graphene Sheets" *Nano Letters* **8**, 2458-2462 (2008)

11. Koenig, S. P., Boddeti, N. G., Dunn, M. L. & Bunch, J. S. "Ultrastrong adhesion of graphene membranes" *Nature Nanotechnology* **6**, 543-546 (2011)

12. Zabel, J., Nair, R. R., Ott, A., Georgiou, T., Geim, A. K., Novoselov, K. S. & Casiraghi, C. "Raman Spectroscopy of Graphene and Bilayer under Biaxial Strain: Bubbles and Balloons" *Nano Letters* **12**, 617-621 (2011)

13. Huang, M., Pascal, T. A., Kim, H., Goddard, W. A. & Greer, J. R. "Electronic−Mechanical Coupling in Graphene from in situ Nanoindentation Experiments and Multiscale Atomistic Simulations" *Nano Letters* **11**, 1241-1246 (2011)

14. Elibol, K., Bayer, B. C., Hummel, S., Kotakoski, J., Argentero, G. & Meyer, J. C. "Visualising the strain distribution in suspended two-dimensional materials under local deformation" *Scientific Reports* **6**, 28485 (2016)

15. Jiang, P., Bertone, J. F., Hwang, K. S. & Colvin, V. L. "Single-Crystal Colloidal Multilayers of Controlled Thickness" *Chemistry of Materials* **11**, 2132-2140 (1999)

16. Zhang, J., Li, Y., Zhang, X. & Yang, B. "Colloidal Self-Assembly Meets Nanofabrication: From Two-Dimensional Colloidal Crystals to Nanostructure Arrays" *Advanced Materials* **22**, 4249-4269 (2010)

17. Plettl, A., Enderle, F., Saitner, M., Manzke, A., Pfahler, C., Wiedemann, S. & Ziemann, P. "Non-Close-Packed Crystals from Self-Assembled Polystyrene Spheres by Isotropic Plasma Etching: Adding Flexibility to Colloid Lithography" *Advanced Functional Materials* **19**, 3279-3284 (2009)

18. Pacakova, B., Verhagen, T., Bousa, M., Hübner, U., Vejpravova, J., Kalbac, M. & Frank, O. "Mastering the Wrinkling of Self-supported Graphene" *Scientific Reports* **7**, 10003 (2017)

19. Choi, J., Kim, H. J., Wang, M. C., Leem, J., King, W. P. & Nam, S. "Three-Dimensional Integration of Graphene via Swelling, Shrinking, and Adaptation" *Nano Letters* **15**, 4525-4531 (2015)

20. Babichev, A. V., Rykov, S. A., Tchernycheva, M., Smirnov, A. N., Davydov, V. Y., Kumzerov, Y. A. & Butko, V. Y. "Influence of Substrate Microstructure on the Transport Properties of CVD-Graphene" *ACS Applied Materials & Interfaces* **8**, 240-246 (2016)

21. Vejpravova, J., Pacakova, B., Endres, J., Mantlikova, A., Verhagen, T., Vales, V., Frank, O. & Kalbac, M. "Graphene wrinkling induced by monodisperse nanoparticles: facile control and quantification" *Scientific Reports* **5**, 15061 (2015)

22. Mi, H., Mikael, S., Liu, C.-C., Seo, J.-H., Gui, G., Ma, A. L., Nealey, P. F. & Ma, Z. "Creating periodic local strain in monolayer graphene with nanopillars patterned by self-assembled block copolymer" *Applied Physics Letters* **107**, 143107 (2015)

23. Jiang, Y., Mao, J., Duan, J., Lai, X., Watanabe, K., Taniguchi, T. & Andrei, E. Y. "Visualizing Strain-Induced Pseudomagnetic Fields in Graphene through an hBN Magnifying Glass" *Nano Letters* **17**, 2839-2843 (2017)

24. Xu, T. *et al.* "Transport mechanisms in a puckered graphene-on-lattice" *Nanoscale* **10**, 7519-7525 (2018)

25. Hinnefeld, J. H., Gill, S. T. & Mason, N. "Graphene transport mediated by micropatterned substrates" *Applied Physics Letters* **112**, 173504 (2018)

26. Branny, A., Kumar, S., Proux, R. & Gerardot, B. D. "Deterministic strain-induced arrays of quantum emitters in a two-dimensional semiconductor" *Nature Communications* **8**, 15053 (2017)

27. Wang, S.-W., Medina, H., Hong, K.-B., Wu, C.-C., Qu, Y., Manikandan, A., Su, T.-Y., Lee, P.-T., Huang, Z.-Q., Wang, Z., Chuang, F.-C., Kuo, H.-C. & Chueh, Y.-L. "Thermally Strained Band Gap Engineering of Transition-Metal Dichalcogenide Bilayers with Enhanced Light–Matter Interaction toward Excellent Photodetectors" *ACS Nano* **11**, 8768-8776 (2017)

28. Yang, T.-H., Chiu, K.-C., Harn, Y.-W., Chen, H.-Y., Cai, R.-F., Shyue, J.-J., Lo, S.-C., Wu, J.-M. & Lee, Y.-H. "Electron Field Emission of Geometrically Modulated Monolayer Semiconductors" *Advanced Functional Materials* **28**, 1706113 (2018)

29. Chaste, J., Missaoui, A., Huang, S., Henck, H., Ben Aziza, Z., Ferlazzo, L., Naylor, C., Balan, A., Johnson, A. T. C., Braive, R. & Ouerghi, A. "Intrinsic Properties of Suspended $MoS_2$ on $SiO_2$/Si Pillar Arrays for Nanomechanics and Optics" *ACS Nano* **12**, 3235-3242 (2018)

# Chapter 4: Nanoscale Rippled Thin Films on Prestrained Substrates

Ripples are found throughout nature, notably on the surface of water, and represent a periodic, wavelike surface. They have also been observed in graphene at various dimensions from nano[1] to micro[2,3] scales when compressive forces wrinkle the membrane. It has been known for some time that when thin film materials are compressed by relaxing a prestrained elastic substrate, the compression at the surface causes a buckling instability out of the plane. With sufficient adhesion between the relaxed and compressed layers, the buckling will tend towards wavelike patterns.[4] Depending on the particular mechanical conditions, various patterns are achievable. One-dimensional waves develop using one axis of strain, while more complex patterns arise with two axes. In particular, by controlling a sequential release of a biaxial system, a herringbone pattern forms,[4,5] analogous to the famously simple origami technique 'Miura-ori' (translated from Japanese as 'leaf-fold'), which is capable of reversibly collapsing in on itself by periodically buckling along the triangular folds.[6]

Previously, elastic substrates have been applied to graphene with uniaxial prestrain,[3] transferring exfoliated graphite devices onto stretched PDMS substrates with otherwise unmodified surfaces. They showed no observable changes to the transport behavior other than a linear dependence of conductivity upon re-stretching, as the bent and buckled membranes mitigate the applied compressive strain of the substrate. When the strip of graphene is compressed, it delaminates from the elastomer surface,[3,7] causing periodic creases/folds based on the stiffness of the graphene. A similar method uses larger corrugated graphene, a capacitive strain sensor.[8] The high charge concentration at the peaks of the wrinkles increases the responsiveness and sensitivity when pressure is applied. Ripples can be controlled by combining the prestrain with a prepatterned substrate.[9] Some studies focus on just a single, individual wrinkle in graphene [10] or $MoS_2$.[11] Here, we expand the number of axis to two, and include a surface treatment of the prestrained elastomer[4,12] in order to control the size and shape of the ripples of large area CVD graphene. In this case, the contribution of graphene to the overall ripple structures is negligible, as it follows the underlying surface's buckled morphology as the substrate is relaxed. This enables greater control of the shape, size, and pattern by modifying this procedure. Heating of the substrate, and in particular soft substrates such as PDMS, has been used to expand and contract the graphene;  the different thermal expansion coefficient causes the surface to ripple in various patterns.[13] Here, the strain comes from mechanically stretching the sample to create prestrain prior to transferring the graphene. The mechanical exfoliation of 2DLMs often introduces wrinkles, folds or bubbles within the sample, as does the CVD transferring process.

There are a number of ways to form rippled, wrinkled, and crumpled 2DLM membranes,[14] whether it is through random creases in mechanical transferred samples, the CVD growth process with conforms to the metallic substrate (and compresses during cooling), which can be further patterned to form textured 2DLMs,[15] or by modifying/functionalizing the membranes after the fact.[16] Other studies of biaxial compressed graphene that crumples up into mess of random wrinkles with non-uniform structure (though the scale of the wrinkles is controllable). In large areas grown on a polyester film, the wrinkles can form islands of flat graphene that are separated by thin wrinkled regions.[17] Using varying ethanol concentration for the final transfer process introduces wrinkle islands with controllable sizes.[18] The wrinkled graphene is shown to have an increased durability and deformation toughness. Strain sensors were fabricated using rGO based "fish-scale like" wrinkles on prestrained elastic adhesive tape.[19] Other applications include stretchable conductors,[20] high surface area electrode materials in supercapacitors[21-23] and lithium batteries,[24] superhydrophobic tunable wettability surfaces,[9,25,26] and increased sensitivity photodetectors,[27-29] and highly efficient field emission from sharp winkles.[30] These wrinkles, however are different than the ripples as there is a less periodic structure and does not have a sinusoidal wave pattern, but similarly can increase its ability to stretch on an elastic substrate.

## 4.1 Lateral compression instability on prestrained surfaces

The mechanism used to ripple surfaces at nano and micro scales consists of prestraining an elastic substrate and then hardening, relaxing, and/or adding a relaxed thin film layer, before relaxing the strain applied to the substrate which buckles the now compressed surface due to an out-of-plane instability (Figure 4.1a). This well-established technique[31] consists of either a thermally[32] or mechanically[4] prestrained substrate deposited with various films from gold[32] and silicon[5] early on, and layered materials such as graphene[3] and molybdenite[33] more recently. An alternative technique uses an oxygen plasma surface treatment of PDMS that oxidizes the surface into variably-thin films of relaxed silicate.[12,34] When the prestrained substrate is relaxed, the compression of the stiffened surface causes a linear instability resulting in periodic buckling. Graphene is an ideal material to incorporate into these rippled structures as it can be deposited smoothly on the prestrained surface and buckle out of plane while retaining its structural integrity due to its high strength and robustness. Furthermore, CVD graphene enables large, atomically thin sheets to uniformly cover the entire sample area.

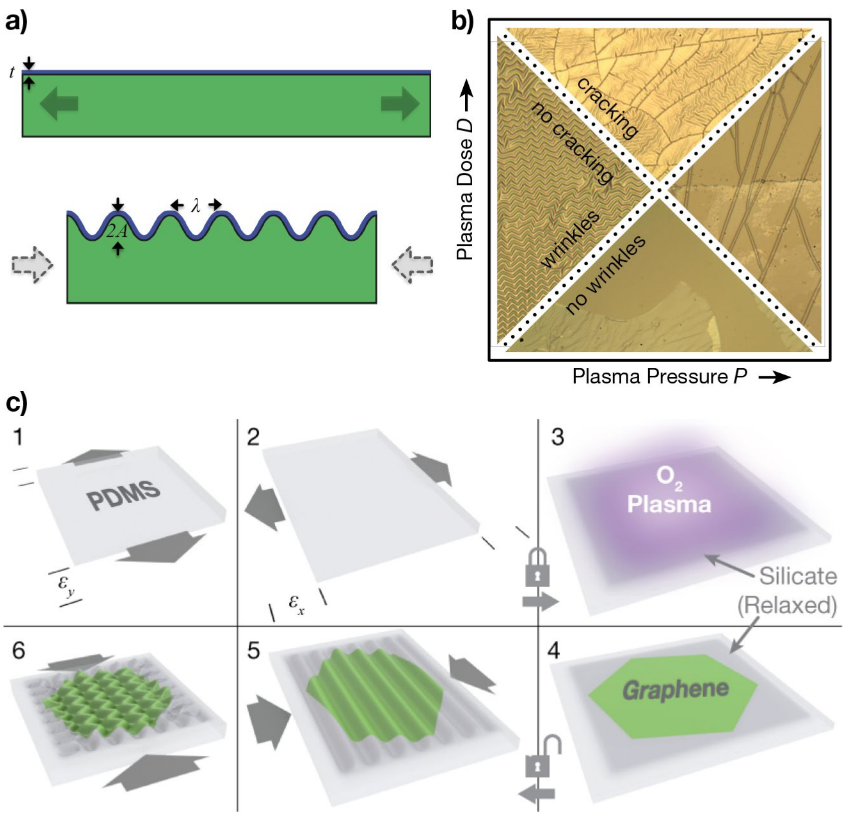

*Figure 4.1 – Schematic of rippled structure on prestrain surfaces*

*a) Schematic of biaxial prestrain, plasma treatment and graphene transfer. b) Schematic of wrinkle and cracking regimes based on plasma dosage and pressure. c) Diagram of prestraining process 1: and 2: Prestrain y-and x-axis of the PDMS. 2.5: place the clamp around the PDMS and screw it together, locking it in place 3: Expose PDMS to the windowed area to oxygen plasma for up to a few minutes. 4: Transfer Graphene through clamp window. 4.5: put the clamped PDMS back into the straining apparatus, the x and y axis of strain are reapplied and then the clamp is released with the windowed area of the surface compress into ripples as the PDMS relaxes. 5: and 6: release x and y axis sequentially to produce ordered herringbone patterns in the center of the window.*

The wavelength of these ripples is substantially influenced by the thickness and stiffness of the thin films, while the pattern is dictated by both the strain profile of the substrate prior to relaxation, and the order in which relaxation occurs, which is in essence how these structures can be controlled and engineered. Based on the linear buckling theory of thin films, for a uniaxial system, the peak-to-peak wavelength $\lambda$ can be predicted as:

$$\lambda = 2\pi t \sqrt[3]{\frac{Y_F}{3Y_S}} \tag{4.1}$$

where $t$ is the thin film thickness and $Y_F$ and $Y_S$ are the plane-strain Young's moduli of the thin film and substrate respectively, defined as $Y/(1 - \nu^2)$ with bulk Young's modulus $E$ and Poisson's ratio $\nu$.[35]

This enables a wide range of ripple dimensions by manipulating the plasma exposure and transferred/deposited layers. With an oxygen plasma dosage of 80 W over 5–120 seconds on prestrained PDMS, ripples of ~0.5–3 μm are achievable. Adding thicker layers such as 10–50 nm of gold will result in much larger dimensions with ripple wavelengths of ~15–30 μm. The amplitude $A$ is determined by the amount of prestrain, once this reaches the critical prestrain $\varepsilon_c$ value, according to:

$$A = t\sqrt{\frac{\varepsilon_{ps}}{\varepsilon_c} - 1} \tag{4.2}$$

where $\varepsilon_{ps}$ is the amount of prestrain.[35] Higher prestrains will result in a larger ripple amplitude, and to compensate, the ripple wavelength will decrease as the peaks and valleys compress towards each other. The critical prestrain $\varepsilon_c$ is the minimum amount in which buckling will begin to occur, and is defined as:

$$\varepsilon_c = -\frac{1}{4}\sqrt[3]{\frac{9Y_S^2}{Y_F^2}} \tag{4.3}$$

above which, ripples will form, and below, simple planar relaxation/compression takes place.[35]

The surface treatment is a critical step in determining the structure of the resulting ripples. This includes both chemical transformation of the prestrained elastic surface into a hardened yet relaxed thin film, and/or depositing additional layers on top of the surface. Thicker and stiffer layers will increase the wavelength of these buckling ripples, so a longer dosage of plasma results in larger ripples. More accurate analysis of these ripples shows a more complex dependence on strain, which is outlined extensively in the literature, but the same general relationships are observed.

Uniaxial prestrain will form a one-dimensional wavelike ripple, while biaxial strain profiles create zigzagging patterns. Depending on how the relaxation step is performed, more or less regular structures form once the critical strain is reached. To achieve well-ordered herringbone structures, one axis is relaxed first to form a uniaxial wave out of plane, then the second perpendicular axis buckles these ripples within the plane. In contrast, relaxing both axes at the same time, or in a non-uniform fashion, results in less-ordered patterns that resemble the folds on the surface of a brain. The orientation of the herringbone is determined by the order in which the axes are relaxed. By slightly mismatching the initial biaxial strain ($\varepsilon_x = \varepsilon_y \pm \Delta\varepsilon_x$), these resulting ripple structures is determined by weather the lower or higher strained axis is relaxed first which will change the zigzag angle and dimension of the herringbone pattern.

## 4.2 Controlling ripple size and shape with biaxial prestrain

Ripples were formed on elastomer substrates that are prestrained and surface treated by either chemical reaction or by placing solid, stiff layers of material. PDMS substrates are made using a Dow Corning Sylgard 184 PDMS kit, mixing 10:1 of the reagents, vacuuming out air bubbles, and curing in an oven at 60–90 °C for 1.5 hours. Silicone films 1–3 mm thick are sliced into the test sample shape (Figure 4.2b-d). A custom linear-screw driven clamp system (Figure 4.2a) is used to precisely strain graphene in uniaxial and biaxial directions. A home-built windowed aluminum clamp (Figure 4.2b) is placed on the PDMS substrate to hold the prestrain in place. The exposed window region can then be treated with oxygen plasma and/or coated with thin film layers and graphene. The clamped PDMS is then placed back into the straining apparatus and roughly brought back to the original strain. The windowed clamp is removed and the prestrain is slowly released, forming the ripples on the surface.

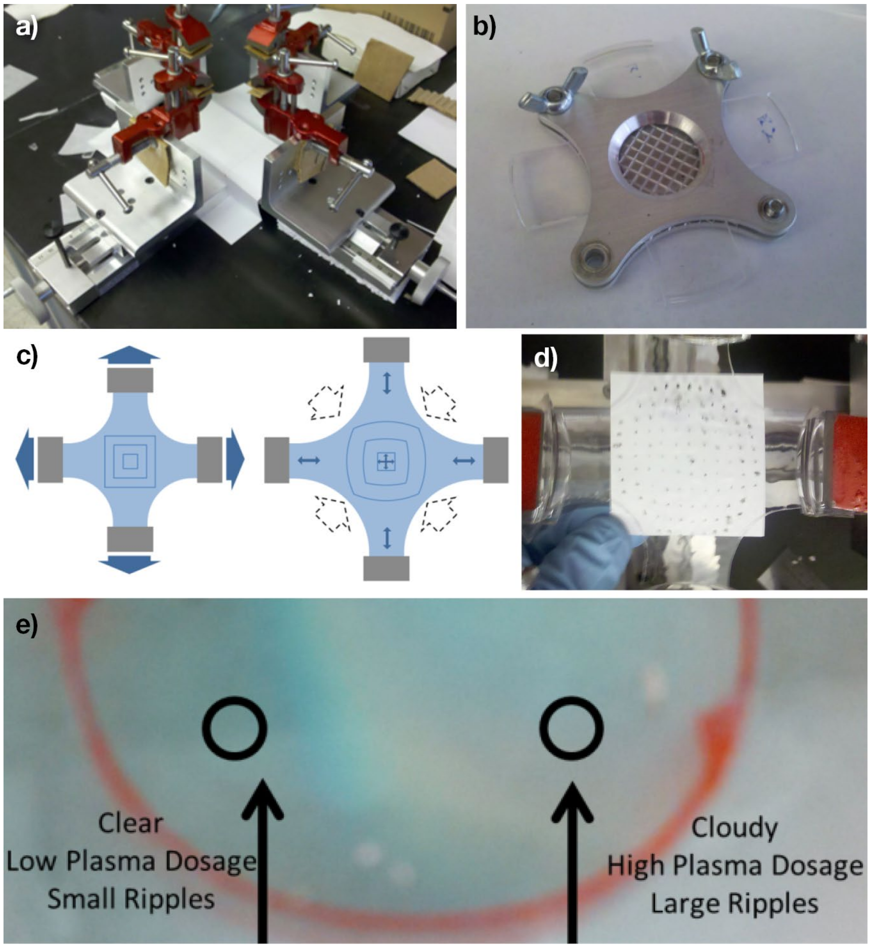

*Figure 4.2 – Biaxial straining device, clamp, and strain profile*

*Photos of a) custom made screw-drive strain apparatus and b) homemade clamp with window. c) Schematic of PDMS substrate shape and amount of prestrain. The strain profile is distorted toward the corners and more even as shown in a photo (d) of equally spaced points being stretched. e) Photograph of the rippled PDMS substrate with variable ripple dimensions caused by the half covered window during the* $O_2$ *plasma exposure inside the red circle.*

Graphene was grown using standard CVD processes as discussed in Section 2.1. In order to transfer the graphene to the elastomer substrates, a wet transfer process was used. The front side of the graphene/copper foil was spin coated with a layer of PMMA to structurally enforce the top graphene layer. Then, the back side of the copper foil was exposed to oxygen plasma for 30 seconds to etch the away graphene. With the PMMA coated side facing up, the exposed side is placed down into a beaker of calcium chloride, floating on top of the solution while the copper foil is etched away in about 15 minutes. Once the copper is removed and the transparent PMMA/graphene film is scooped out of the solution using a clean piece of silicon, and slowly placed in beakers of clean DI water, with several consecutive washes. Finally, the stretched elastomer substrate is used to scoop out the PMMA/graphene film, and then a brief acetone/IPA rinse/bath is used to dissolve away the PMMA, leaving a flat, relaxed graphene film on the plasma treated prestrained PDMS substrate.

SEM images show the rippled structure with high contrast due to the conductive nature of the graphene on the surface. The herringbone ripple structures of various dimensions are shown in Figure 4.3a and b. Alongside are AFM topographic maps (Figure 4.3c and d) of similar regions from the same sample, showing the vertical displacement of the ripples and the overall structural morphology. The range in ripple size is controlled by the oxygen plasma, and by partially covering half the sample, a gradient of ripple wavelengths is achieved within a single sample. These regions are characteristic of the sample as a whole, and are highly ordered within their local area, however, over larger areas, many imperfections of the herringbone lattice are present, and cause disordering of the otherwise periodic zigzag pattern. The presence of these defects is attributed to either imperfections in the substrate surface or by the approximate biaxial strain system developed for these experiments (Figure 4.2c and d). Larger order periodic patterns are also observed throughout the ripple structures, and towards the edges of the strained region, different buckling patterns are observed.

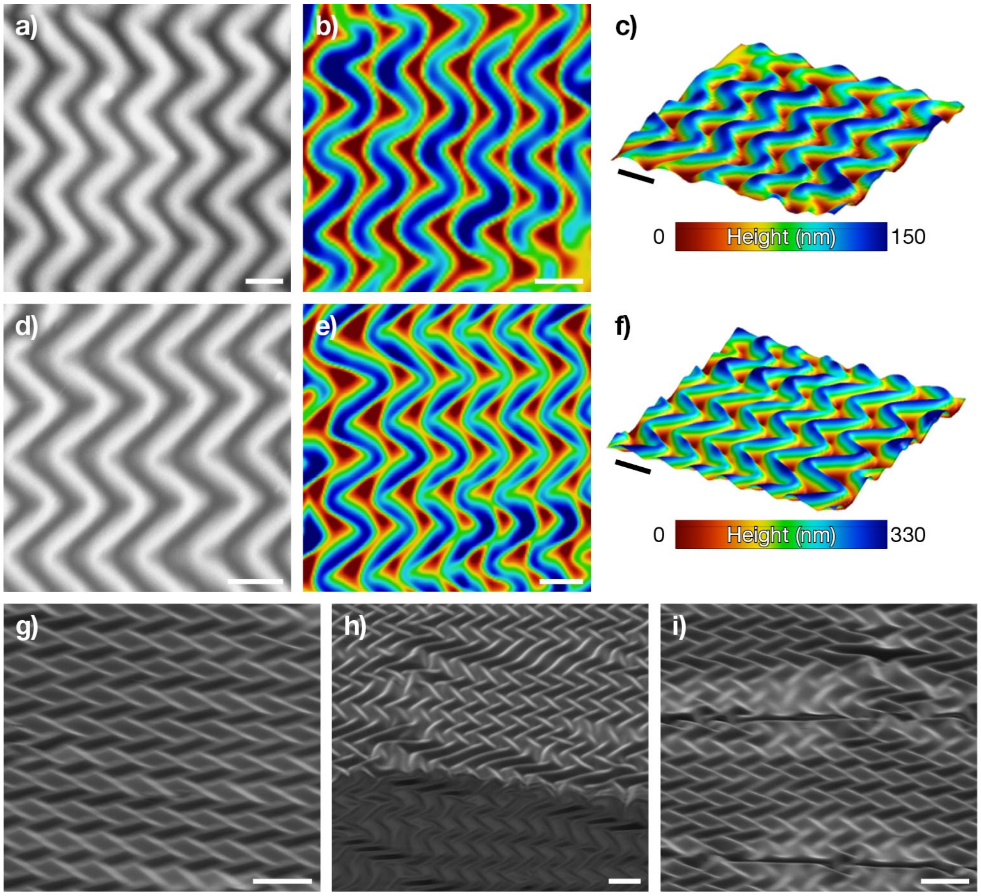

*Figure 4.3 – SEM and AFM of graphene ripples*
*Low dosage 1 µm (a-c) and high dosage 3 µm (d-f) SEM images (a and d), and AFM topography images (b,c,e and f) of ripples. Tilted SEM of herringbone graphene on rippled PDMS (g), showing the edge of graphene on bare substrate (h) and graphene folded into cracks in the substrate. Scale bars 1 µm (a-c), 3 µm (d-f), and 5 µm (g-i).*

So far, these structures have assumed a uniform surface treatment, whereas defining geometric changes along the surface treatment yields more complex patterns. For example, locally masking the oxygen plasma dosage will create regions of varying silica thicknesses on the same sample (Figure 4.2e). No rippling will occur on fully protected regions, while progressively larger ripples form as the plasma dosage increases. Patterned layers and devices that are transferred onto the surface before relaxation will also locally change the surface thickness and stiffness, which will alter the resulting ripple structures. To engineer various ripple patterns, it is important to control the local plasma exposure and added layers, along with precise straining and relaxing procedures.

Taking this further, regions of the PDMS substrate can be completely masked out from exposure the plasma which fully retains its initial elastic behavior within this region after being relaxed. The closer proximity of the mask to the substrate creates sharp edges of ripples are formed using square shadow mask window is directly on the PDMS, in contrast to the gradual change in dimensions in Figure 4.2e. The SEM image suggest that graphene rips along the edge of the transition, as the height variation is significant, and the graphene seems to be disconnected with a sharp line across the top of the peaks. Graphene placed on top of this transition regions is shown in Figure 4.4a. Furthermore, using the same PS microspheres dropcast technique of Chapter 3, a monolayer of spheres is used to mask the substrate from plasma exposure to create periodic regions of unaffected PDMS separated by an interconnection network of ripples between the spheres. AFM and OM of these structures is shown in Figure 4.4b-d showing how the unidirectional ripples form between the circular regions that were masked, with a sharp lip at the edge of the circle.

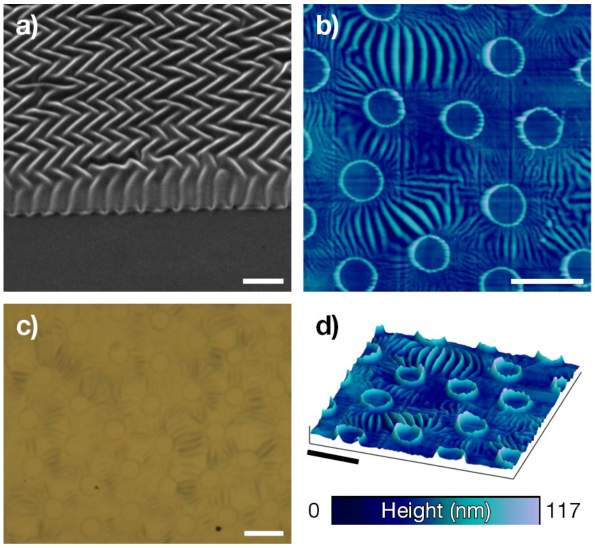

*Figure 4.4 – Masked patterning of ripple structures*
*Shadow masking regions of PDMS used to block the plasma exposure during prestrain, causing an edge where the ripples stop and show a straight sinusoidal pattern (a). Polystyrne spheres as a shadomask forms interconnected regions of strain. AFM topography (b and d) and optical images (c) after relaxing the prestrain and removal of the sphere mask. Scale bars 5 μm (a-d).*

Another consideration in order to control the rippled structures is by manipulating the morophologies after the relaxation and initial formation of the ripples. This can be achieved in two ways, by shining a focused visible light laser on a region of kinks in the ripples (Figure 4.5a and b). After exposure to the Raman microspectrometer during mapping, the kinks rearange themselves. Another example is by using the scanning electorn beam of an SEM to an exposed region of the ripple graphene (Figure 4.5c and d), which relaxes the amplitude of the ripples. Note that the ripples in this experiment are on top of flat PDMS that was not treated with the oxygen plasma durin prestrain, meanign there are no PDMS ripples, only biaxial graphene ripples compressed by the flat PDMS. The influence of light energy capable of altering the ripple structures is reminescent of the induction of circular ripples in graphene blisters using laser light.[36]

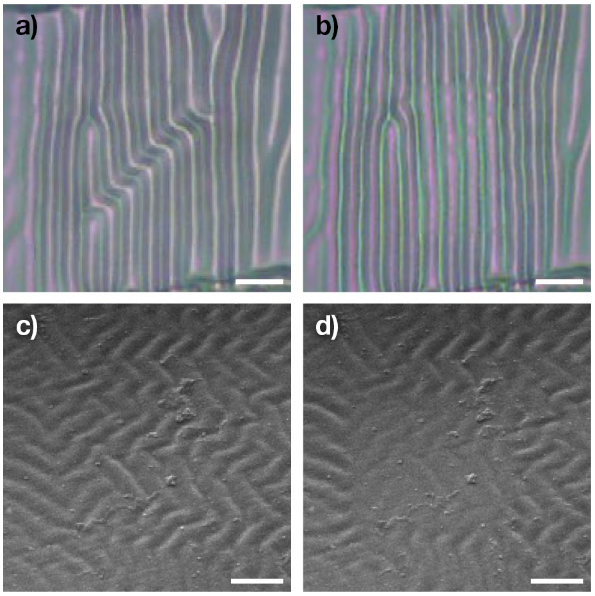

*Figure 4.5 – Inducing changes to the ripple structure with lasers and electron beams*
*Optical image of before (a) and after (b) exposure to the microspectrometer laser beam which removes a dislocation in the uniaxial wave pattern as it heats up. Tilted SEM images of graphene ripples before (c) and after (d) electron beam exposure to the center region where the amplitude is reduced in (d). Scale bars 5 µm (a-d).*

Other methods of forming ripples on prestrained substrates is to deposit layers on top of the prestrained PDMS, such as gold. Physical deposition of 50 nm Cr/Au film on top of the prestrained substrate yields much larger periodicity than the treated surface itself. After relaxing the PDMS, a gold rippled structure (Figure 4.6) with wavelength ~15 µm and an amplitude of 3.6 µm form on the surface, with significant cracking throughout the film (Figure 4.6e,f). Thicker gold layers can increase the wavelength such as 30 µm for 100 nm Cr/Au film. The pattern itself is also significantly different than the wavelike PDMS ripples; the buckling is much sharper at the valley and flat at the peak, and the biaxial structure is squarer, boxier shaped rather than zigzag. Additionally, the pattern seems be asymmetrically slanted, which may be attributed to the irregular strain profile within the biaxial straining apparatus and clamp. Further research done to investigate the controllable changing the orientation,[37] patterns, and morphology of wrinkles and ripples could prove useful in applications such MEMS/NEMS and microfluidics and others.

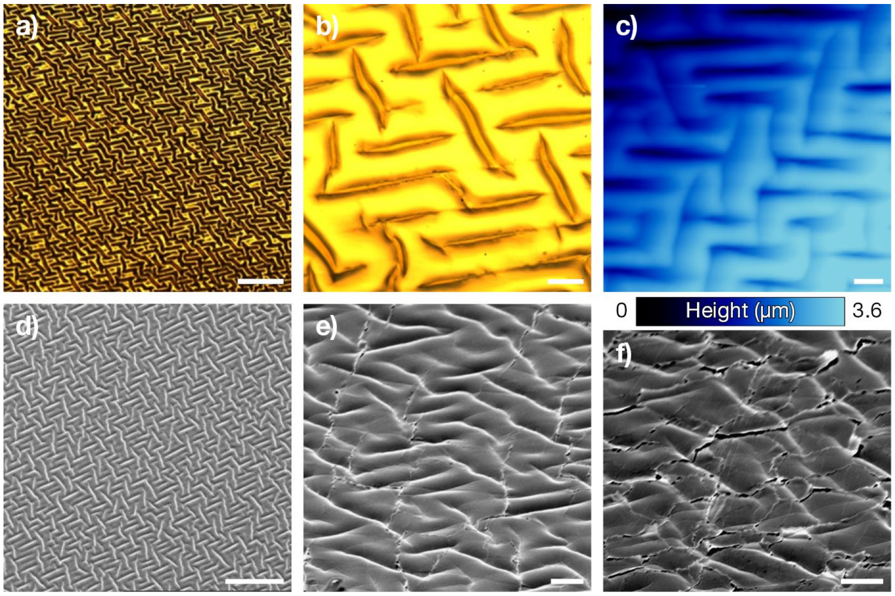

*Figure 4.6 – Periodic patterns of gold–graphene films deposited on prestrained PDMS Gold thin films deposited on prestrained, untreated PDMS optical (a,b), AFM (c), SEM (d), tilted SEM (e) and images after releasing the substrate prestrain, a larger pattern more similar to a basket weave appears. Scale bars 100 µm (a,d), 10 µm (b,c,e,f).*

### 4.3 Effects of strain on Raman peak shift

Raman spectroscopy reveals that the characteristic peaks of graphene, *G* and *2D* phonon modes, are shifted by physical deformation of the lattice. Uniaxial and biaxial strains produce a linear dependence. Compressive and tensile strains result in a red and blue shift respectively for both peaks. Asymmetric distortions of the hexagonal lattice (e.g. uniaxial strain) contribute to the splitting of $G^+$ and $G^-$ peaks that are otherwise degenerate as a single *G* peak in unstrained graphene. The strain within graphene can therefore be estimated by mapping the surface with the Raman spectroscope, providing a profile of deformation. The spot size of the focused excitation laser is a limiting factor in the lateral resolution of the map, and will generate the collective spectra of the area within the spot. The effective region of measurement is typically below 1 μm, which limits the ripple sizes that can be. If the feature size of the strain profile is smaller than this limit will lead to broadening of the peaks and potentially underestimates the peak strain that is inferred from the shift of the Raman peaks, due to an averaging of adjacent regions subject to lower strains. Raman measurements were made using a Horiba LabRam 800 system and a 514 nm excitation wavelength. Mapping is carried out with a motorized *x-y* stage equipped microscope and uses a peak fitting in order to chart the shift in *G* and *2D* characteristic Raman shifts.

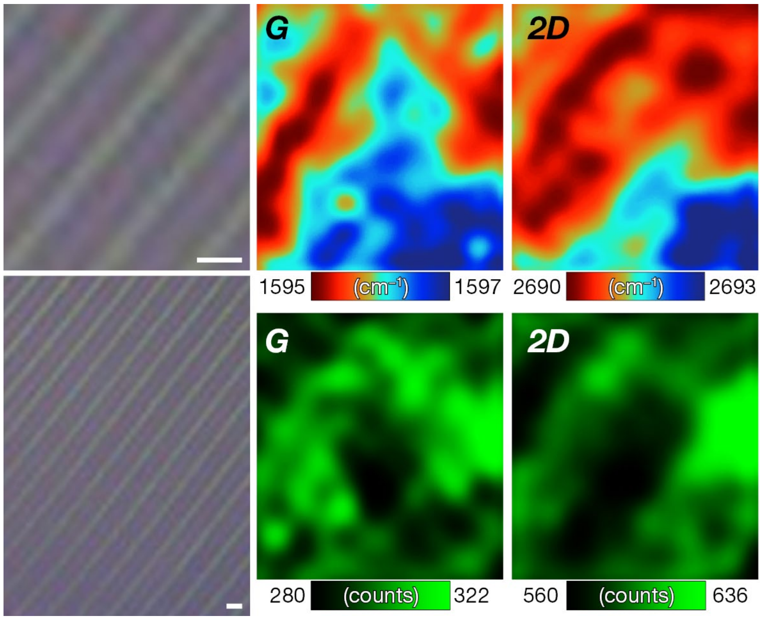

*Figure 4.7 – Raman spectral map of uniaxial ripples*
*Uniaxial ripples measured using Raman spectroscopy: peak position (top) and peak intensity (bottom) of the G (left) and 2D (right) peaks. Scale bars 2 μm.*

Raman maps of a representative 3 μm herringbone structure are shown in Figure 4.7 and 4.8, demonstrating the periodic strain profile within each ripple. The peak intensity does resemble a herringbone structure that matches the optical image pattern. This could be due to the varying incident angle and curvature of the surface where the laser hits, however it should not influence the position of the peaks, as the ripple amplitude is within the depth of field of the confocal microscope. The *G* and *2D* peaks are shifted by up to 7 $cm^{-1}$ and 6 $cm^{-1}$ respectively, which estimates the strain at less than 1%. The actual peak values may be somewhat higher due to the laser spot size averaging of the Raman signal. The strain is much lower than the requirements for inducing a bandgap or pseudomagnetic effects.  but is understandably lower than simply compressing graphene by the amount of prestrain due to the nature of the buckling instability that inherently reduces the residual strain. Additionally, the strain maxima will increase as the ripples get smaller, which may enable the manipulation of graphene's electronic properties.

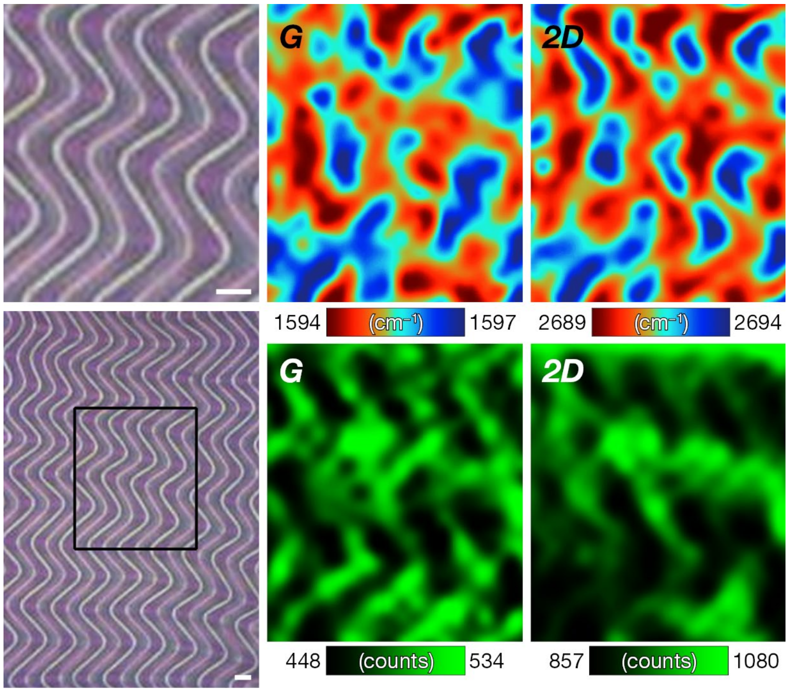

*Figure 4.8 – Raman spectral mapping of herringbone graphene ripples #1*
*OM images and map of Raman G and 2D peak shift of the rippled graphene G (left) and 2D (right) of peak shift (top) and peak intensity (bottom). Scale bars 2 μm.*

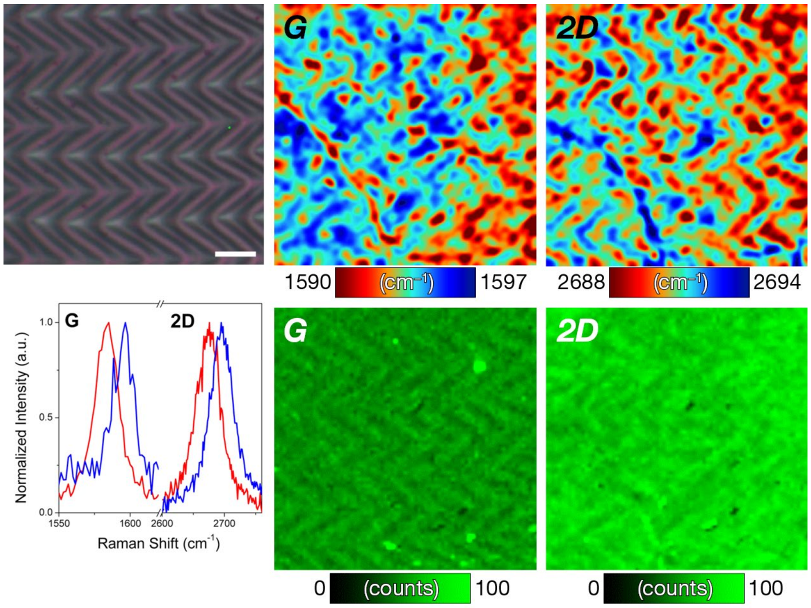

*Figure 4.9 – Raman spectral mapping of herringbone graphene ripples #2*
*OM images and map of Raman G and 2D peak shift of the rippled graphene G (left) and 2D (right) of peak shift (top) and peak intensity (bottom) with maximum peak spectra shown for each peak. Scale bars 5 µm.*

The strain profile is periodic throughout the ripple, clearly following the herringbone pattern that matches the physical structure. In this particular region, there is a diagonal line of high blueshift that does not appear in either the optical image or the peak intensity maps, which is probably some anomalous region where the graphene is somehow stuck in a strain state that does not conform to the buckled structure, or perhaps a rip or irregularity within the substrate. Other factors that may influence the Raman maps are delamination of the graphene from the rippled substrate and impurities within the PDMS or from the transfer process.

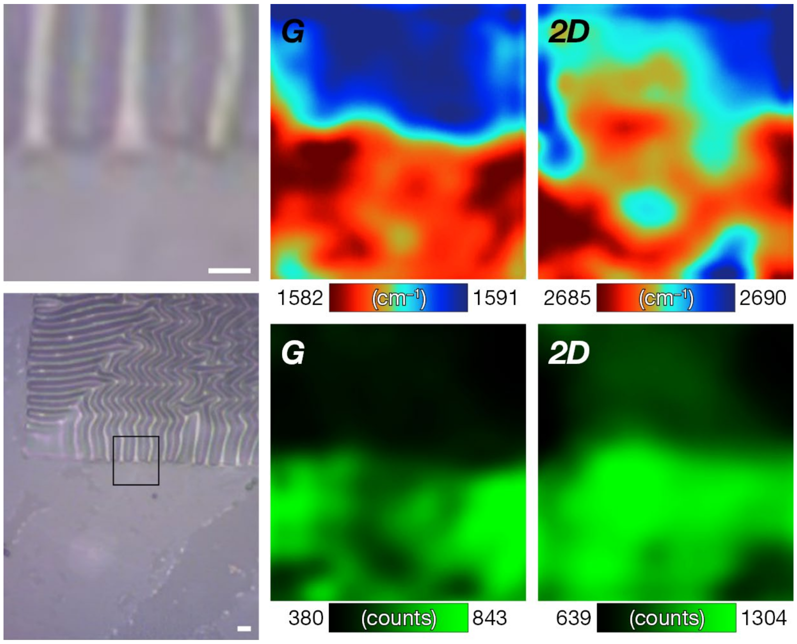

*Figure 4.10 – Raman spectral map of rippled and non-rippled regions*
*Graphene ripples next to no ripples at the edge of a region that was masked from the $O_2$ plasma, measured using Raman spectroscopy: peak position (top) and peak intensity (bottom) of the G (left) and 2D (right) peaks. Scale bars 1 μm (top) and 2 μm (bottom).*

The laser power must be kept low, as local heating of the PDMS substrate can lead to thermal expansion and a defocusing of the sample while mapping. Or, with enough power, the laser will completely destroy the ripple structures. However, controlled exposure can lead to specific changes within the ripples, such as adding or removing kinks (see Figure 4.5a and b), and could potentially enable the manipulation of the ripples into more sophisticated patterns. The low power and short acquisition time required to not damage the sample and collect useful maps ends up limiting the clarity of the results due to low signal to noise ratio, along with a high background signal from the substrate.

Standard electronic measurements of the sheet resistance were taken using shadow masked chrome/gold electrodes, showing a typical linear *I*–*V* curve of a normal resister. This indicates that there are no significant changes in the electronic properties of the graphene, as there is not a significant amount of strain within the ripples of this size, which is consistent with previous reports.[3] It is reasonable to assume that, by shrinking the ripple dimensions smaller, and increasing the prestrain and therefore ripple amplitude amount, that larger strain maxima could be produced. Preliminary theoretical results suggest that herringbone wavelengths around 100 nm would be enough to induce a pseudomagnetic field of around 10 T, which should be observable. However, even if some areas were to exhibit the previously observed pseudomagnetic effects, only the peak strained regions would be affected, and the current would simply travel around these regions. Therefore, other characterization methods must be applied, such as STS or photoemission spectroscopies. PDMS is insulating and not suitable for STM based characterization, though either using gold ripples, or by casting the graphene ripples into a conducting substrate, removing them from the PDMS, may enable tunneling measurements.

## Conclusions

The controlled rippling of graphene using prestrained elastic substrates is achieved in uniaxial and biaxial varieties as well as masked patterns with microscopic characterization and Raman spectroscopy analysis. Various shapes and sizes are controllable by altering the plasma dosage conditions while the sample is being presrained ranging in ripple periodicity of 500 nm – 3 μm or more. A noticeable pattern within the Raman peak shift reveals the periodic nature of the strain profile corresponding to the ripple morphology. The limited focusing of the excitation laser spot size makes it difficult to resolve the pattern as the dimensions are decreased. The peaks are averaged over the area, meaning the true amount of strain in underestimated, and only the largest sized ripples were able to be mapped at all. This could be improved using an AFM tip-enhanced Raman scattering (TERS) spectrometer to increase the mapping precision and lateral resolution.

Arbitrary stacks of layered materials can be added to these ripples with a negligible to small influence on the ripple structure itself, enabling the controlled rippling and straining of entire devices. Further investigations of nanoripples using the wide variety of other two dimensional layered materials such as $MoS_2$[9,33] or phosphorene[38] have shown interesting behavior when wrinkled. Also, using other substrate materials or intermediate layers, such as BN, can also be used to alter the ripple structures.

On one hand, we want to use large strains to controllably induce various electronic properties within the material, e.g. bandgap engineering. While on the other hand we may want to have materials of which these properties are resistant to substantial mechanical stimulations, e.g. ultra-flexible electronics. Though graphene already has an incredibly high elasticity as a single crystalline material, it can still only withstand roughly ~30% strain, which pales in comparison to some elastic polymers. Introducing these ripple structures allows for the substrate to stretch and compress without significantly straining the graphene beyond its limits, just as the Miura-ori paper can transform from a flat piece of paper and fold in on itself without tearing.

## References

1. Fasolino, A., Los, J. H. & Katsnelson, M. I. "Intrinsic ripples in graphene" *Nature Materials* **6**, 858-861 (2007)

2. Bao, W., Miao, F., Chen, Z., Zhang, H., Jang, W., Dames, C. & Lau, C. N. "Controlled ripple texturing of suspended graphene and ultrathin graphite membranes" *Nature Nanotechnology* **4**, 562-566 (2009)

3. Wang, Y., Yang, R., Shi, Z., Zhang, L., Shi, D., Wang, E. & Zhang, G. "Super-Elastic Graphene Ripples for Flexible Strain Sensors" *ACS Nano* **5**, 3645-3650 (2011)

4. Lin, P.-C. & Yang, S. "Spontaneous formation of one-dimensional ripples in transit to highly ordered two-dimensional herringbone structures through sequential and unequal biaxial mechanical stretching" *Applied Physics Letters* **90**, - (2007)

5. Choi, W. M., Song, J., Khang, D.-Y., Jiang, H., Huang, Y. Y. & Rogers, J. A. "Biaxially Stretchable “Wavy” Silicon Nanomembranes" *Nano Letters* **7**, 1655-1663 (2007)

6. Mahadevan, L. & Rica, S. "Self-Organized Origami" *Science* **307**, 1740-1740 (2005)

7. Zang, J., Ryu, S., Pugno, N., Wang, Q., Tu, Q., Buehler, M. J. & Zhao, X. "Multifunctionality and control of the crumpling and unfolding of large-area graphene" *Nature Materials* **12**, 321-325 (2013)

8. Paul, A., Gupta, S. & Dahiya, R. "Corrugated Graphene Network Based Pressure Sensor" *2018 IEEE SENSORS*, 1-4 (2018)

9. Okogbue, E., Kim, J. H., Ko, T.-J., Chung, H.-S., Krishnaprasad, A., Flores, J. C., Nehate, S., Kaium, M. G., Park, J. B., Lee, S.-J., Sundaram, K. B., Zhai, L., Roy, T. & Jung, Y. "Centimeter-Scale Periodically Corrugated Few-Layer 2D $MoS_2$ with Tensile Stretch-Driven Tunable Multifunctionalities" *ACS Applied Materials & Interfaces* **10**, 30623-30630 (2018)

10. Xu, K., Cao, P. & Heath, J. R. "Scanning Tunneling Microscopy Characterization of the Electrical Properties of Wrinkles in Exfoliated Graphene Monolayers" *Nano Letters* **9**, 4446-4451 (2009)

11. Deng, S., Gao, E., Xu, Z. & Berry, V. "Adhesion Energy of $MoS_2$ Thin Films on Silicon-Based Substrates Determined via the Attributes of a Single $MoS_2$ Wrinkle" *ACS Applied Materials & Interfaces* **9**, 7812-7818 (2017)

12. Bowden, N., Huck, W. T. S., Paul, K. E. & Whitesides, G. M. "The controlled formation of ordered, sinusoidal structures by plasma oxidation of an elastomeric polymer" *Applied Physics Letters* **75**, 2557-2559 (1999)

13. Sampathkumar, K., Androulidakis, C., Koukaras, E. N., Rahova, J., Drogowska, K., Kalbac, M., Vetushka, A., Fejfar, A., Galiotis, C. & Frank, O. "Sculpturing graphene wrinkle patterns into compliant substrates" *Carbon* **146**, 772-778 (2019)

14. Chen, W., Gui, X., Yang, L., Zhu, H. & Tang, Z. "Wrinkling of two-dimensional materials: methods, properties and applications" *Nanoscale Horizons* **4**, 291-320 (2019)

15. Hong, J.-Y., Kim, W., Choi, D., Kong, J. & Park, H. S. "Omnidirectionally Stretchable and Transparent Graphene Electrodes" *ACS Nano* **10**, 9446-9455 (2016)

16. Kim, S. J., Kim, D. W., Lim, J., Cho, S.-Y., Kim, S. O. & Jung, H.-T. "Large-Area Buckled $MoS_2$ Films on the Graphene Substrate" *ACS Applied Materials & Interfaces* **8**, 13512-13519 (2016)

17. Li, Z., Kinloch, I. A., Young, R. J., Novoselov, K. S., Anagnostopoulos, G., Parthenios, J., Galiotis, C., Papagelis, K., Lu, C.-Y. & Britnell, L. "Deformation of Wrinkled Graphene" *ACS Nano* **9**, 3917-3925 (2015)

18. Chen, W., Gui, X., Liang, B., Liu, M., Lin, Z., Zhu, Y. & Tang, Z. "Controllable Fabrication of Large-Area Wrinkled Graphene on a Solution Surface" *ACS Applied Materials & Interfaces* **8**, 10977-10984 (2016)

19. Liu, Q., Chen, J., Li, Y. & Shi, G. "High-Performance Strain Sensors with Fish-Scale-Like Graphene-Sensing Layers for Full-Range Detection of Human Motions" *ACS Nano* **10**, 7901-7906 (2016)

20. Feng, C., Yi, Z., Dumée, L. F., She, F., Peng, Z., Gao, W. & Kong, L. "Tuning micro-wrinkled graphene films for stretchable conductors of controllable electrical conductivity" *Carbon* **139**, 672-679 (2018)

21. Chen, T., Xue, Y., Roy, A. K. & Dai, L. "Transparent and Stretchable High-Performance Supercapacitors Based on Wrinkled Graphene Electrodes" *ACS Nano* **8**, 1039-1046 (2014)

22. Liu, Y.-Z., Chen, C.-M., Li, Y.-F., Li, X.-M., Kong, Q.-Q. & Wang, M.-Z. "Crumpled reduced graphene oxide by flame-induced reduction of graphite oxide for supercapacitive energy storage" *Journal of Materials Chemistry A* **2**, 5730-5737 (2014)

23. Clerici, F., Fontana, M., Bianco, S., Serrapede, M., Perrucci, F., Ferrero, S., Tresso, E. & Lamberti, A. "In situ $MoS_2$ Decoration of Laser-Induced Graphene as Flexible Supercapacitor Electrodes" *ACS Applied Materials & Interfaces* **8**, 10459-10465 (2016)

24. Song, J., Yu, Z., Gordin, M. L. & Wang, D. "Advanced Sulfur Cathode Enabled by Highly Crumpled Nitrogen-Doped Graphene Sheets for High-Energy-Density Lithium–Sulfur Batteries" *Nano Letters* **16**, 864-870 (2016)

25. Choi, J., Mun, J., Wang, M. C., Ashraf, A., Kang, S.-W. & Nam, S. "Hierarchical, Dual-Scale Structures of Atomically Thin $MoS_2$ for Tunable Wetting" *Nano Letters* **17**, 1756-1761 (2017)

26. Chen, P.-Y., Sodhi, J., Qiu, Y., Valentin, T., Steinberg, R., Wang, Z., Hurt, R. & Wong, I. "Multiscale Graphene Topographies Programmed by Sequential Mechanical Deformation" *Advanced Materials* **28** (2016)

27. Gowda, P., Sakorikar, T., Reddy, S. K., Ferry, D. B. & Misra, A. "Defect-Induced Enhancement and Quenching Control of Photocurrent in Few-Layer Graphene Photodetectors" *ACS Applied Materials & Interfaces* **6**, 7485-7490 (2014)

28. Kim, M., Kang, P., Leem, J. & Nam, S. "A stretchable crumpled graphene photodetector with plasmonically enhanced photoresponsivity" *Nanoscale* **9**, 4058-4065 (2017)

29. Shen, J. *et al.* "High-performance Schottky heterojunction photodetector with directly grown graphene nanowalls as electrodes" *Nanoscale* **9**, 6020-6025 (2017)

30. Wang, F.-J., Deng, L.-N. & Deng, J.-H. "Facile synthesis of differently shaped, ultrathin, and aligned graphene flakes without a catalyst for highly efficient field emission" *Applied Surface Science* **355**, 218-225 (2015)

31. Chen, C.-M. & Yang, S. "Wrinkling instabilities in polymer films and their applications" *Polymer International* **61**, 1041-1047 (2012)

32. Bowden, N., Brittain, S., Evans, A. G., Hutchinson, J. W. & Whitesides, G. M. "Spontaneous formation of ordered structures in thin films of metals supported on an elastomeric polymer" *Nature* **393**, 146-149 (1998)

33. Castellanos-Gomez, A., Roldán, R., Cappelluti, E., Buscema, M., Guinea, F., van der Zant, H. S. J. & Steele, G. A. "Local Strain Engineering in Atomically Thin $MoS_2$" *Nano Letters* **13**, 5361-5366 (2013)

34. Yin, J., Yagüe, J. L., Eggenspieler, D., Gleason, K. K. & Boyce, M. C. "Deterministic Order in Surface Micro-Topologies through Sequential Wrinkling" *Advanced Materials* **24**, 5441-5446 (2012)

35. Yang, S., Khare, K. & Lin, P.-C. "Harnessing Surface Wrinkle Patterns in Soft Matter" *Advanced Functional Materials* **20**, 2550-2564 (2010)

36. Koskinen, P., Karppinen, K., Myllyperkiö, P., Hiltunen, V.-M., Johansson, A. & Pettersson, M. "Optically Forged Diffraction-Unlimited Ripples in Graphene" *The Journal of Physical Chemistry Letters* **9**, 6179-6184 (2018)

37. Rhee, D., Paci, J. T., Deng, S., Lee, W.-K., Schatz, G. C. & Odom, T. W. "Soft Skin Layers Enable Area-Specific, Multiscale Graphene Wrinkles with Switchable Orientations" *ACS Nano* **preprint** (2019)

38. Li, Y., Wei, Z. & Li, J. "Modulation of the electronic property of phosphorene by wrinkle and vertical electric field" *Applied Physics Letters* **107**, 112103 (2015)

# Chapter 5: 2DLM Based Nanoelectronic and Flexible Devices

One of the primary motivations for research into graphene and other 2DLM, as previously discussed, is their extraordinary and versatile use in nanoelectronics devices and incorporation into vdWHs.[1-3] Their unique morphology with atomically sharp thickness combined with enhanced material properties enable novel engineering capabilities with superior performance. While still in early research and developmental stages, these materials could pave the way towards advanced circuitry far beyond the shortcomings of current semiconductor technologies which will inevitably hit their ultimate physical limitations. Many different advances using 2DLMs have been made over the years, from ultra-high radio frequency analog transistors[4,5] and flexible[6] logic circuits to LEDs, solar cells,[7,8] supercapacitors,[9] photodetectors,[10,11] strain gauges,[12,13] ultrasensitive chemical sensors,[14] and biosensors[15]. Completely new designs that utilize the unique properties have also emerged, such as tunneling transistors[16] that stretch the limits of these newly available materials.

Research and development takes form in stages; first, fundamental scientific studies of the material properties to better understand their underlying principles discover new physical phenomena that emerge. Then, the materials can be engineered into more practical devices to explore how to properly and scalably process them for utilization in commercial applications.[17,18] This chapter explores a number of 2DLM based nanoelectronics in order to better understand the newly synthesized materials and to demonstrate their capabilities in unique and high-performing devices. Firstly, TMD based transistors are fabricated to test the material properties and electronic performance of CVD grown $MoSe_2$ films, as well as furthering the advanced technique of transferring a self-aligned gate stack for $MoS_2$ based high-frequency devices, including inverters and amplifiers on flexible substrates. Next, we explore the use of graphene as a contact electrode which exploits its planar structure and work function tunability in vertical and lateral transistor structures. These studies demonstrate just part of the range and versatility of 2DLMs for advanced nanoelectronics and soft, flexible materials for innovative engineering designs.

## 5.1 TMD based field-effect transistors

Since the first studies done with graphene, electronic devices have been a cornerstone of 2DLM research, as the exception properties allow for both higher performing devices and novel device designs which enable new capabilities. Lateral channel devices are more reminiscent of traditional FET designs, while novel vertical device configurations allow for extremely short channels that are limited by the semiconducting layer's thickness rather than conventional lithographic constraints. Using two-dimensional semiconducting materials (e.g. TMDs) as the channel offers similar advantages as graphene, with the addition of an inherent bandgap which allows for much higher on–off ratios and true digital logic performance in contrast to typical graphene-based devices.[19,20]

Figure 5.1 shows the electronic performance of FETs based on the CVD grown 2DLMs described in Section 2.1 which demonstrates the viability of lab grown samples in electronic applications. This *p*-type semiconducting 2DLM, with an indirect to direct bandgap transition of ~1.2 eV in bulk $WSe_2$ to ~1.65 eV at the monolayer. 100 nm thick gold electrodes are placed on the $WSe_2$ samples in order to perform standard transport measurements ($I_{ds}$–$V_{ds}$ and $I_{ds}$–$V_g$ plots) in ambient conditions using the substrate as a back gate. Figure 5.1b shows the $I_{ds}$–$V_{ds}$ output of the monolayer device at various gate voltages, and Figure 5.1c shows the transfer characteristics of the monolayer device at different source-drain bias, from 0 to 4 V while sweeping the back-gate voltage from –100 to 100 V, demonstrating typical *p*-type semiconducting behavior, with mobility as high as 100 cm$^2$/V·s and an on–off ratio reaching $10^8$ for the monolayer device. Multiple devices were measured, including monolayer, bilayer, and multilayer domains, with mobility ranges from 10–350 cm$^2$/V·s as summarized in Figure 5.1d. These measurements compare favorably to even exfoliated $WSe_2$ devices and demonstrate the high crystal quality of the grown samples' viability and scalability of CVD growth of 2DLMs for advanced electronics.

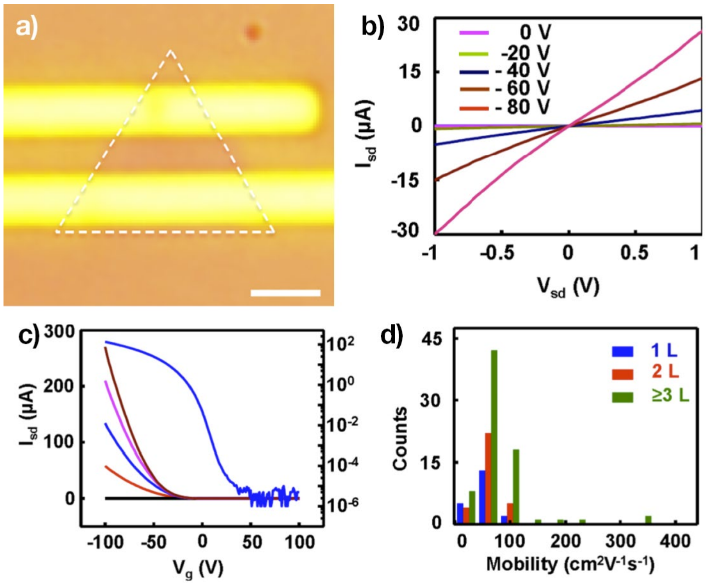

*Figure 5.1 – Electronic properties of* $WSe_2$ *atomic layers.*
*a) OM image of a monolayer* $WSe_2$ *transistor. b)* $I_{sd}$–$V_{sd}$ *output characteristics. c)* $I_{sd}$–$V_g$ *transfer characteristics at* $V_{sd}$ = 0, 1, 2, 3, and 4 V. *d) Mobility values of* $WSe_2$ *FETs with varying layer numbers. Scale bar 2 μm (a). Adapted*[21]

## 5.2 High-frequency devices

Due to the exceptionally high carrier mobility, high carrier saturation velocity, and large critical current density found in graphene, radio frequency electronics with graphene as the active channel material are often sought after. A novel development in the advancement of graphene electronics is the use of core-shell metal/insulator nanowires as a top-gate electrode. These devices allow for miniaturization of the channel down to the diameter of the nanowire by incorporating a self-aligning deposition technique down to 140 nm in length.[4] This technique enabled high-frequency operation with intrinsic cutoff frequencies ($f_T$) reaching 300 GHz in graphene using self-aligned platinum electrodes deposited on a $Co_2Si$ nanowire coated with a 5 nm thin layer $Al_2O_3$ dielectric shell.

Further advances in fabrication of self-aligned graphene devices using a transfer technique show both a scalable improvement and an increase in performance up to 427 GHz cutoff frequency in a 67 nm channel length device.[22] Rather than use core-shell nanowires, a prefabricated array of dielectric-electrode gate stack at transferred onto the lithographically patterned CVD graphene-toped substrate. Using this more controlled and scalable fabrication technique also offers a better adherence to the flat nature of the channel, as the gate stack has a rectangular shape in contrast to the cylindrical core-shell nanowire gate design retaining the similar advantages of the self-aligned source and drain and channel length defined by the width of the gate stack.

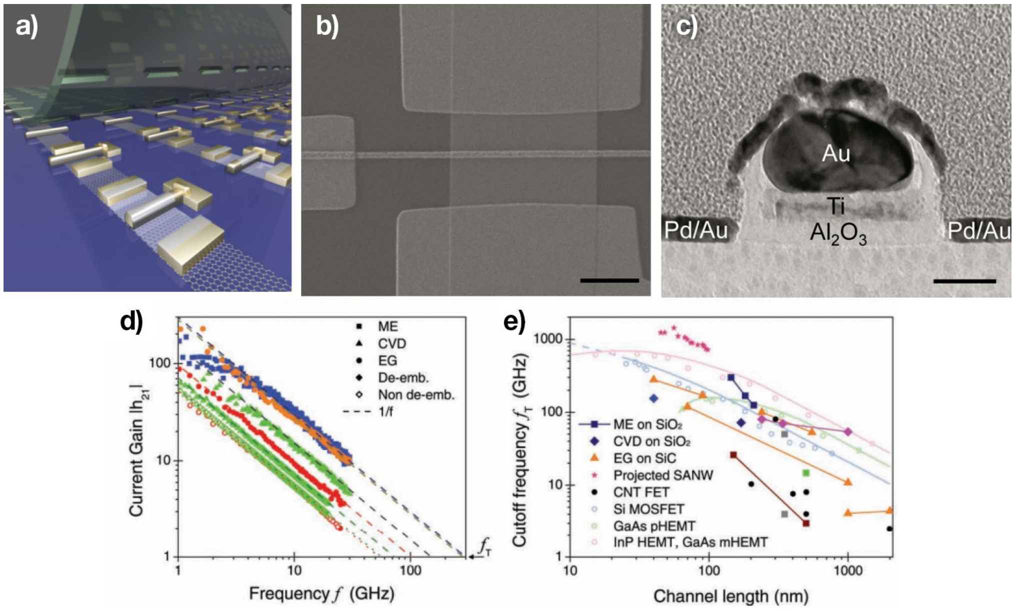

*Figure 5.2 – Scaled transfer of prefabricated nanowire gate/mask on graphene*
*a) Artistic representation of the gate stack transfer process. b) SEM and c) TEM cross-section of the gate stack self-aligned graphene device. d) Current gain vs frequency and e) cutoff frequency vs. channel length for various transistor types. Adapted (a-c)*[22] *and (d-e)*[23]

The novel technique of transferring the gate stack with self-aligned electrodes is applicable to arbitrary substrates. Herein, we apply this approach to other materials such as $MoS_2$ based high speed devices.[24] The field effect mobility , derived from the back-gate transconductance, $dI_{ds}/dV_g$, using the equation:

$$\mu = \frac{dI_{ds}}{dV_g} \frac{L}{W \cdot C_0 \cdot V_{ds}} \tag{5.1}$$

with the channel length $L = 1$ μm, width $W = 4$ μm, and back-gate capacitance $C_0 = 11.5$ nF/cm$^2$. At a drain voltage $V_{ds} = 0.5$ V, the mobility is calculated to be 170 cm$^2$/V·s, which is comparable to the highest previously reported values. In general, fewer layers of $MoS_2$ will display a lower off-state current, and larger for thicker samples. This is likely due to either a partial screening of the electric field by the bottom layers, interlayer resistance, and/or Coulomb scattering effects of the substrate. $MoS_2$ of thickness 2–7 nm provides both sufficiently high mobility and on–off ratio which are primarily used in the following devices.

Linear $I_{ds}$–$V_{ds}$ curve at low bias voltages a good Ohmic contact between the $MoS_2$ channel and the self-aligned Ni/Au source-drain electrodes. Low temperature measurements down to 30 K indicate a contact barrier well below 2.6 meV, which is negligible at room temperature. In contrast to graphene transistors, a clear current saturation is observable using high source–drain biases, with a drain-source conductance $G_{ds} = dI_{ds}/dV_{ds}$ close to zero, which is critical to achieve the highest performance speeds. Transfer characteristic using the $I_{ds}$–$V_{TG}$ curves of the devices show a typical *n*-type field effect with a threshold voltage near –2 V and an on–off ratio over $10^7$, which is sufficient for digital logic operations, of which ordinary graphene devices are incapable. In a 116 nm transistor with clear current saturation, an intrinsic gain (ratio of transconductance to drain-source conductance) of over 30 is achieved, representing the highest achievable gain in a single transistor. Typically, the on-state current and the transconductance both increase with decreasing channel length (from 1 μm to 68 nm), indicating the charge transport is dominated by the $MoS_2$ channel which makes good contact with the self-aligned source–drain electrodes.

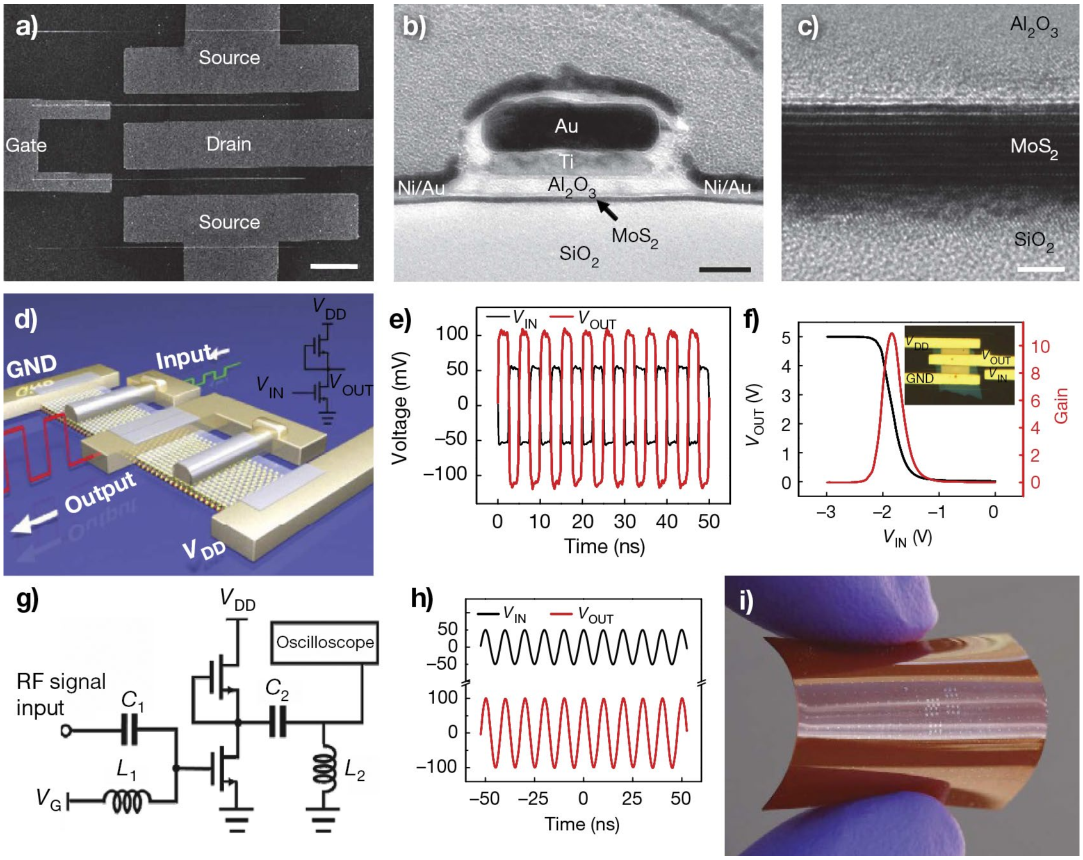

*Figure 5.3 – High frequency modulator made with dual nanowire gated transistors*

*a) SEM image and b) and c) TEM cross-section of a graphene modulator, shown schematically (d). e) $V_{IN}$ (black) and $V_{OUT}$ (red) vs. time of the inverter device. f) Output voltage $V_{OUT}$ (left axis) and gain (right axis) of the inverter device as a function of the input voltage $V_{IN}$ with bias voltage 5 V, (OM image inset). g) Electronic diagram of the amplifier device configuration. h) $V_{IN}$ (black) and $V_{OUT}$ (red) vs. time for the amplifier device. i) Photo of the flexible $MoS_2$ modulators on a bent substrate. Scale bars 5 μm (a), 50 nm (b) 3nm (c). Adapted*[24]

For radio frequency measurements, de-embedded S parameters use to describe the intrinsic performance of devices removing degrative extrinsic effects such as parasitic pad capacitance. Small-signal current gain $|h_{21}|$ shows a typical 1/f frequency dependence, leading to cut-off frequencies $f_T$ up to 42 GHz and a maximum oscillation frequency $f_{MAX}$ (the frequency at which the power gain is equal to one) up to 50 GHz, with a 5 V direct current bias. The peak cut-off frequency follows a 1/L scaling trend due to carrier velocity saturation more similar to conventional short-channel Si and III-V semiconductor devices than to graphene which is limited by contact resistance. The $f_{MAX}$ does not follow the same 1/L trend, which can be attributed to competition between $f_T$, gate resistance, and output conductance.

With excellent device performance including high on–off ratio, power gain, $f_T$, and $f_{MAX}$, these $MoS_2$ transistors are suitable for both digital and analogue electronics within the gigahertz regime. Fabrication of inverters and amplifiers on quartz substrates is achieved by interconnecting two self-aligned top-gated $MoS_2$ based transistors (Figure 5.3a-c). An inverter is a basic logic circuit that outputs a voltage with opposite value to its input, described by its voltage transfer curve (input voltage vs. output voltage), made by interconnecting the drain with one of the transistor gates. The $MoS_2$ inverter achieves a voltage gain (slop of the transition region of the transfer curve) of over 10. With an RF input signal of 200 MHz square wave of input, an inverted signal with relative voltage gain of 2 (6 dB) and negligent delay (Figure 5.3f). Further optimization of the circuit design, thinner dielectric, and larger bias could further improve high-frequency performance. An RF amplifier is constructed by integrating two transistors in series, acting as a ‘load’ transistor and a ‘switch’ transistor where the gates are the output and input respectively. With a 100 MHz sinusoidal wave input with 100 mV peak voltage, a wave with larger amplitude is outputted. The amplifier (Figure 5.3g and h) exhibits a voltage gain up to 2 (6 dB) which is retained for frequencies up to 500 MHz, while a gain > 1 remains up to 1 GHz. A propagation delay of 370 ps is measured in the $MoS_2$ amplifier using a square wave generator, which matches well with simulated results.

2DLMs such as $MoS_2$ have been used in flexible electronics and optoelectronics such as low-power, high-frequency devices. By using a bendable substrate such as polyimide (Figure 5.3), the fabricated circuits can be stretched. A high current density of 48 µA/µm (at 2 V bias) in a 116 nm channel is capable of 1000 cycles of bending to a 5 mm radius of curvature without any apparent degradation. A 68 nm $MoS_2$ FET on polyamide shows a lower $f_T$ and $f_{MAX}$ of 13.5 and 10.5 GHz respectively, which is lower than on silicon or quartz substrates, likely due degradation of the charge transport due to roughness of the substrate. By fabricating $MoS_2$ circuits on flexible substrate, inverters exhibited a voltage gain of 9, while amplifiers are capable of a voltage gain > 1 up to 300 MHz sinusoidal input signal and a propagation delay of 2 ns. These results demonstrate the high performance of 2DLM based nanoelectronics for high frequency operation with additional flexible abilities by utilizing graphene, TMDs, and others as the channel material. Next will discuss the use of graphene as the contact electrode rather than the channel, due to its nanoscale two-dimensional formfactor, exceptional conductivity, and tunable electronic properties.

### 5.3 Graphene as a contact electrode

Incorporating graphene as a contact electrode has a number of advantages, for example its planar form factor allows for defect free coverage of a thin film with a highly conductive single atomic layer. Additionally, with its unique band structure and semi-metal characteristics, the work function energy level can be tuned with an electric field, allowing for the contact barriers to be adjusted, enabling interesting device configurations. For instance, we use an organic semiconductor (*p*-type P3HT and PTB7, and *n*-type PCBM) thin film as a vertical transistor (Figure 5.4) with a tunable graphene electrode that shows exceptional performance with a high on–off ratio over $10^3$.[25] The thin film thickness controlled vertical channels of ~100–200 nm have a large planar channel area displays a current density above 3.4 A/cm$^3$ which allows for high delivery current while maintaining a high cutoff frequency compared to other conventional organic transistors. Furthermore, the device fabrication encapsulates the organic material, protecting the delicate molecules from ambient exposure. This also creates a mask for the channel region to remove excess material, allowing for multiple *p*- and *n*-type devices to be easily made on one chip.

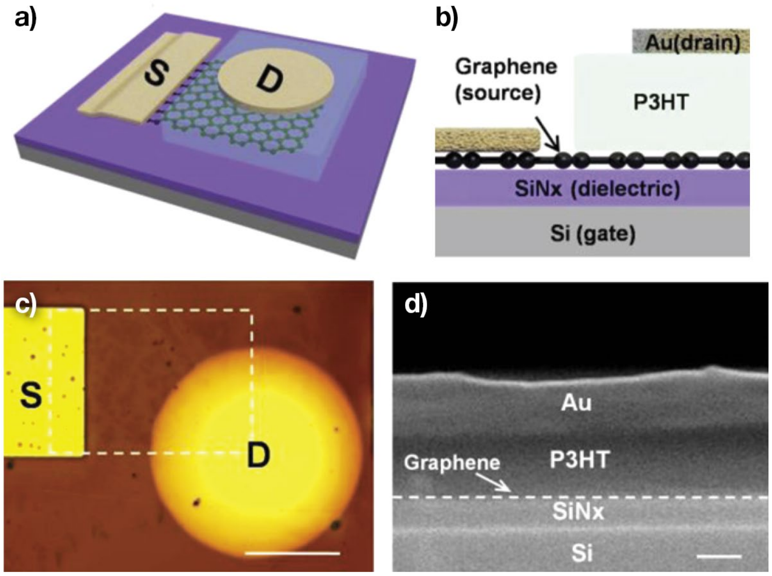

*Figure 5.4 – Graphene as a tunable contact thin film transistor*
*3D (a) and cross section (b) schematics of a tunable graphene contact device with P3HT vertical channel. OM image (c) and TEM cross section (d) of the device. Scale bar 100 μm (c) and 100 nm (d). Adapted*[25]

Further efforts of incorporating graphene as a contact electrode have shown promise, in particular in conjunction with semiconducting 2DLMs as the channel material, such as $MoS_2$.[26] 2DLMs are quite compatible as the van der Waals interaction and planar structure allow for close contact of the thin materials with benefits such as a lack of the damaging effects of depositing metals has on the underlying materials. One development is use of graphene as a back electrode; that is, place graphene electrodes underneath and the $MoS_2$ on top in order to achieve ohmic contact.[26] Since the Fermi level of graphene is able to be tuned to that of the channel material using a gate potential, this essentially enables a barrier free contact to the $MoS_2$ layer by aligning the band structures. Mechanically exfoliated graphene is used, with the space between strips defining the channel length after mechanically exfoliated monolayer $MoS_2$ is dry transferred on top. The residue-free technique ensures an ultraclean, atomically sharp interface between the graphene and $MoS_2$ and a pure van der Waals contact. Cr/Au thin film electrodes are then deposited onto the graphene using e-beam lithography to complete the device for testing purposes.

Ohmic contact is achievable even at low temperatures (down to 1.9 K) which is not seen using conventional metal contacts. The van der Waals bonding of the clean, nondamaged layers reduces charge trapping states, which prevents Fermi level pinning that plagues contact behavior with conventional metal contacts. Additionally, by encapsulation with boron nitride (BN) to further isolate and passivate the device, two-terminal extrinsic field effect mobility up to a record-high 1300 $cm^2/V\cdot s$ in $MoS_2$ at low temperature.[26] There are three types of interface geometries are possible using van der Waals contacts: coplanar contacts, staggered contacts and hybrid stack contacts (Figure 5.5). their advantages and limitations are discussed in detail below. With tunable work function and a pristine van der Waals interface, graphene−2DSC (both the coplanar and staggered geometry) shows a smaller SB height compared with metal−2DSC contacts.

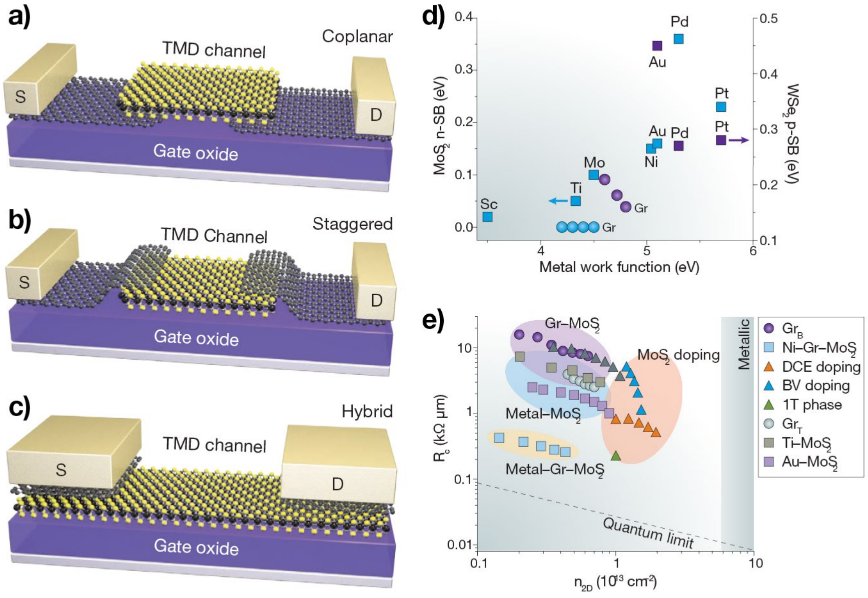

*Figure 5.5 – Graphene as a barrier free contact electrode with $MoS_2$*

*Schematics of three types of graphene contact electrode in vdWHs with two-dimensional semiconductors: coplanar contacts (a), staggered contacts (b) and hybrid contacts (c) with the source (S) and drain (D) electrodes on either end. d) Schottky barrier (SB) height for $MoS_2$ (n-type) and $WSe_2$ (p-type) using various contact materials. e) Contact resistance, $R_c$, between $MoS_2$ and various semiconductors: two-dimensional semiconductors; BV, benzyl viologen; DCE, dichloroethane; Gr, graphene; $Gr_B$, graphene (bottom); $Gr_T$, graphene (top); TMDs. The dashed line marks the quantum limit for crystalline materials. Adapted*[1]

## Conclusions

2DLMs have useful application into a wide range of applications, enabling novel designs for new and improved devices for advanced nanoelectronics. Their robust and flexible nature and membranelike behavior make them suitable for incorporating in soft electronics which enable new and unique applications from robotics to wearable technology and the internet of things. While graphene has an incredibly high mobility and is capable of extremely cutoff high-frequencies, its inherent zero bandgap make semiconductors like $MoS_2$ more capable with acceptable on–off ratios, at the expense of mobility and switching speed. The inverter and amplifiers shown here offer good performance with low power and capable of flexible robustness. Additionally, using graphene as an electrode material allows for compact, transparent and tunable contacts for improved performance and versatile applications. These studies just scratch the surface of what 2DLM based electronics are capable of, as this fast pace field continues to innovate at the laboratory scale, which will inevitably translate to practical application.

## References

1. Liu, Y., Weiss, N. O., Duan, X., Cheng, H.-C., Huang, Y. & Duan, X. "Van der Waals heterostructures and devices" *Nature Reviews Materials* **1**, 16042 (2016)

2. Liu, Y., Huang, Y. & Duan, X. "Van der Waals integration before and beyond two-dimensional materials" *Nature* **567**, 323-333 (2019)

3. Liu, Y., Duan, X., Huang, Y. & Duan, X. "Two-dimensional transistors beyond graphene and TMDCs" *Chemical Society Reviews* **47**, 6388-6409 (2018)

4. Liao, L., Lin, Y.-C., Bao, M., Cheng, R., Bai, J., Liu, Y., Qu, Y., Wang, K. L., Huang, Y. & Duan, X. "High-speed graphene transistors with a self-aligned nanowire gate" *Nature* **467**, 305-308 (2010)

5. Banszerus, L., Schmitz, M., Engels, S., Dauber, J., Oellers, M., Haupt, F., Watanabe, K., Taniguchi, T., Beschoten, B. & Stampfer, C. "Ultrahigh-mobility graphene devices from chemical vapor deposition on reusable copper" *Science Advances* **1**, e1500222 (2015)

6. Kim, S. J., Choi, K., Lee, B., Kim, Y. & Hong, B. H. "Materials for Flexible, Stretchable Electronics: Graphene and 2D Materials" *Annual Review of Materials Research* **45**, 63-84 (2015)

7. Wang, X., Zhi, L. & Müllen, K. "Transparent, Conductive Graphene Electrodes for Dye-Sensitized Solar Cells" *Nano Letters* **8**, 323-327 (2008)

8. Tsai, M.-L., Su, S.-H., Chang, J.-K., Tsai, D.-S., Chen, C.-H., Wu, C.-I., Li, L.-J., Chen, L.-J. & He, J.-H. "Monolayer $MoS_2$ Heterojunction Solar Cells" *ACS Nano* **8**, 8317-8322 (2014)

9. El-Kady, M. F., Shao, Y. & Kaner, R. B. "Graphene for batteries, supercapacitors and beyond" *Nature Reviews Materials* **1**, 16033 (2016)

10. Yu, W. J., Liu, Y., Zhou, H., Yin, A., Li, Z., Huang, Y. & Duan, X. "Highly efficient gate-tunable photocurrent generation in vertical heterostructures of layered materials" *Nature Nanotechnology* **8**, 952 (2013)

11. Weiss, N. O. & Duan, X. "Building potential for graphene photodetectors" *NPG Asia Materials* **5**, e74-e74 (2013)

12. Li, X., Zhang, R., Yu, W., Wang, K., Wei, J., Wu, D., Cao, A., Li, Z., Cheng, Y., Zheng, Q., Ruoff, R. S. & Zhu, H. "Stretchable and highly sensitive graphene-on-polymer strain sensors" *Scientific Reports* **2**, 870 (2012)

13. Kim, Y.-J., Cha, J. Y., Ham, H., Huh, H., So, D.-S. & Kang, I. "Preparation of piezoresistive nano smart hybrid material based on graphene" *Current Applied Physics* **11**, S350-S352 (2011)

14. Singh, E., Meyyappan, M. & Nalwa, H. S. "Flexible Graphene-Based Wearable Gas and Chemical Sensors" *ACS Applied Materials & Interfaces* **9**, 34544-34586 (2017)

15. Ding, M., Shiu, H.-Y., Li, S.-L., Lee, C. K., Wang, G., Wu, H., Weiss, N. O., Young, T. D., Weiss, P. S., Wong, G. C. L., Nealson, K. H., Huang, Y. & Duan, X. "Nanoelectronic Investigation Reveals the Electrochemical Basis of Electrical Conductivity in Shewanella and Geobacter" *ACS Nano* **10**, 9919-9926 (2016)

16. Britnell, L. *et al.* "Field-Effect Tunneling Transistor Based on Vertical Graphene Heterostructures" *Science* **335**, 947 (2012)

17. Ferrari, A. C. *et al.* "Science and technology roadmap for graphene, related two-dimensional crystals, and hybrid systems" *Nanoscale* **7**, 4598-4810 (2015)

18. Tan, C., Cao, X., Wu, X.-J., He, Q., Yang, J., Zhang, X., Chen, J., Zhao, W., Han, S., Nam, G.-H., Sindoro, M. & Zhang, H. "Recent Advances in Ultrathin Two-Dimensional Nanomaterials" *Chemical Reviews* **117**, 6225-6331 (2017)

19. Duan, X., Wang, C., Pan, A., Yu, R. & Duan, X. "Two-dimensional transition metal dichalcogenides as atomically thin semiconductors: opportunities and challenges" *Chemical Society Reviews* **44**, 8859-8876 (2015)

20. Chhowalla, M., Jena, D. & Zhang, H. "Two-dimensional semiconductors for transistors" *Nature Reviews Materials* **1**, 16052 (2016)

21. Zhou, H., Wang, C., Shaw, J. C., Cheng, R., Chen, Y., Huang, X., Liu, Y., Weiss, N. O., Lin, Z., Huang, Y. & Duan, X. "Large Area Growth and Electrical Properties of p-Type $WSe_2$ Atomic Layers" *Nano Letters* **15**, 709-713 (2015)

22. Cheng, R., Bai, J., Liao, L., Zhou, H., Chen, Y., Liu, L., Lin, Y.-C., Jiang, S., Huang, Y. & Duan, X. "High-frequency self-aligned graphene transistors with transferred gate stacks" *Proceedings of the National Academy of Sciences* **109**, 11588 (2012)

23. Weiss, N. O., Zhou, H., Liao, L., Liu, Y., Jiang, S., Huang, Y. & Duan, X. "Graphene: An Emerging Electronic Material" *Advanced Materials* **24**, 5782-5825 (2012)

24. Cheng, R., Jiang, S., Chen, Y., Liu, Y., Weiss, N., Cheng, H.-C., Wu, H., Huang, Y. & Duan, X. "Few-layer molybdenum disulfide transistors and circuits for high-speed flexible electronics" *Nature Communications* **5**, 5143 (2014)

25. Liu, Y., Zhou, H., Weiss, N. O., Huang, Y. & Duan, X. "High-Performance Organic Vertical Thin Film Transistor Using Graphene as a Tunable Contact" *ACS Nano* **9**, 11102-11108 (2015)

26. Liu, Y., Wu, H., Cheng, H.-C., Yang, S., Zhu, E., He, Q., Ding, M., Li, D., Guo, J., Weiss, N. O., Huang, Y. & Duan, X. "Toward Barrier Free Contact to Molybdenum Disulfide Using Graphene Electrodes" *Nano Letters* **15**, 3030-3034 (2015)

# Chapter 6: Conclusion

Graphene and other 2DLMs offer new opportunities in advanced electronic devices which can both enhance the performance of current technologies and enable new possibilities of which traditional materials are incapable. By utilizing the unique nature of atomically thin nanosheets, common fabrication techniques used in conjunction with advancements in nanotechnology processing technologies enable precise control over layered van der Waals heterostructures and complex device configurations. Furthermore, strain engineering is utilized to alter the structure, and in turn electronic properties of these 2DLMs; rather than cutting into ribbons, we use nanoscale origami to fold, bend, and stretch these membranes in precise and controlled morphologies. Inspired by the extraordinary designs of origami, new designs with unique capabilities demonstrate the power of both simple and complex folding patterns of origami. Many innovations within compact deployable structures and compliant mechanisms benefit from mimicking origami and incorporating its principles into incredibly novel engineering designs. Applying this approach and miniaturizing it to micro and nanoscale materials and electromechanical systems is a natural progression.

The first step towards realizing these materials into practical applications requires economical and scalable synthesis of high quality 2DLMs for further integration into devices. This begins with the development of techniques such as CVD based synthesis which is capable of depositing highly uniform monolayers onto various substrates for further fabrication. This growth method allows for large areas of monolayer 2DLMs with good electronic performance, though not quite as good as pristine samples from mechanical exfoliation. CVD graphene grown on copper is both self-limiting in its nature, creating uniform monolayers, and can be readily transferred onto any desirable substrate, while the CVD TMDs are grown directly onto insulating

$SiO_2$. Further advancements, on top of improving the crystal quality and performance, have enabled direct growth of both lateral and vertical heterostructures without the need for transferring.

In order to realize the advanced functionality of these new materials, fundamental studies of their electronic behavior demonstrate their extraordinary performance and novel material properties. Further modification of these properties is possible through altering the extrinsic conditions, for example the use of bandgap engineering to induce a bandgap in graphene, or to modify it in other 2DLMs. Here, nanoscale origami is explored as a novel approach, where bending, folding, and stretching are the key ingredients towards changing the electronic properties in conjunction with engineered physical distortions. Though there are numerous methods in which to induce strain into these two-dimensional nanomembranes, we presented two main strategies: suspending and stretching graphene across a gap in which it can bend into the open region, and the compression and buckling of graphene on prestrained elastic substrates. Both approaches offer versatility in the patterns in which the graphene conforms with considerable control over the feature sizes at the nanoscale. The robust nature of the nanosheets makes them ideal for stretching and conforming to various morphologies while withstanding high strains. Further research has begun to uncover what unique properties can arise from the engineering the strain and structure of these nanosheets for novel applications.

2DLM based nanoelectronics provide many exceptional qualities to enhance device capabilities, such as improved performance, but also diverge from the brittle nature of inherent to conventional electronics. Superior material properties such as high carrier mobilities enable remarkably high-frequency operation with record breaking cutoff frequencies. Though many roadblocks remain, perhaps one day 2DLMs will supplant silicon in integrated circuits, if not simply excel in niche applications such as low power and flexible devices. Regardless, they continue to attract immense research efforts in materials science, and have already undoubtedly had tremendous impact on the future of both academia and industry.

The End